POLITECNICO DI TORINO

Master's Degree in Biomedical Engineering

Master's Thesis

MODEL-BASED PLANNING AND REAL-TIME MONITORING FOR LASER THERMAL THERAPY IN OPHTHALMOLOGY

Supervisors

Prof. Guido Perrone

Prof. Gianni Coppa

Prof. Alberto Vallan

Candidate

Rosita Orsetti

Academic Year 2022/2023

"Stay hungry, stay foolish"
Steve Jobs

Summary

Severe vision impairment and blindness represent one of the major medical challenges of the next decades, especially in western countries due to the population ageing. Today, the World Health Organization estimates that at least one billion people worldwide suffer from moderate or severe distance vision impairment or blindness due to unaddressed refractive error (88.4 million), cataract (94 million), age-related macular degeneration (8 million), glaucoma (7.7 million) and diabetic retinopathy (3.9 million). This numbers are expected to worsen considering that the prevalence of severe impairment leading to blindness is larger in over 50-year-old people. The social impact of such diseases is very high because it limits working capacities and, in the case of elder adults, contributes to social isolation, difficulty in walking, with the consequence of higher risk of falls and fractures.
At present there are no definitive therapies capable of reversing these eye diseases; therefore, the treatments are aimed at stopping or at least slowing their evolution. One of the most promising approaches is the use of lasers to provide thermal therapies, especially since the development of micro-pulse technology, which has opened a range of new treatments. However, the widespread of these techniques is still limited for several reasons, one of the most important being the need for accurate predictions and measurements of the induced temperature to optimize the treatment outcome. Therapy planning methods, which can estimate the thermal response of the target area, are critical in adjusting laser power and treatment duration. Moreover, real-time monitoring systems are key to directly control the temperature induced during the thermal processes. The thesis investigates the optimisation of thermal therapies based upon tissue absorption of laser radiation to

generate a localised temperature increase. The purpose of this thesis is to study a method for estimating and controlling the temperature distribution during laser treatment processes, helping the ophthalmologist in planning, and monitoring thermal therapies. This has required the development of a suitable parametric full-eye 3D model, analyzed with COMSOL Multiphysics finite element software, to provide insights about the eye-laser interaction in view of proposing personalized treatments for each patient. The model is composed of two parts: the light-tissue interaction and the heat diffusion in tissues. In particular, the thesis work has developed a "heat pulse method" to recover the thermal parameters of biological tissue. Relying on the intrinsic correlation between biological properties and thermal outcomes, the response to a short heat pulse, not intense enough to cause cell damage, is fitted with the analytical solution of the bioheat transfer equation. The temperature is measured through all-optical fiber sensors based on fiber Bragg gratings. The method has been validated first through numerical simulations and the impact of different types of uncertainties has been analyzed. Experimental tests have been carried out on phantoms and ex-vivo tissue to demonstrate the viability of the proposed approach.

Sommario

I gravi disturbi della vista e la cecità rappresentano una delle principali sfide mediche dei prossimi decenni, soprattutto nei paesi occidentali a causa dell'invecchiamento della popolazione. Oggi, l'Organizzazione Mondiale della Sanità stima che almeno un miliardo di persone in tutto il mondo soffra di disturbi moderati o gravi della visione a distanza o di cecità a causa di errori di rifrazione non risolti (88,4 milioni), cataratta (94 milioni), degenerazione maculare legata all'età (8 milioni), glaucoma (7,7 milioni) e retinopatia diabetica (3,9 milioni). Questi numeri sono destinati a peggiorare se si considera che la prevalenza dei disturbi alla vista che portano alla cecità è maggiore negli ultracinquantenni. L'impatto sociale di queste malattie è molto elevato perché limita le capacità lavorative e, nel caso degli anziani, contribuisce all'isolamento sociale, alla difficoltà di deambulazione, con conseguente aumento del rischio di cadute e fratture.
Al momento non esistono terapie definitive in grado di far regredire queste malattie oculari; pertanto, i trattamenti mirano ad arrestarne o almeno rallentarne l'evoluzione. Uno degli approcci più promettenti è l'uso del laser per fornire terapie termiche, soprattutto dopo lo sviluppo della tecnologia a microimpulsi, che ha aperto una gamma di nuovi trattamenti. Tuttavia, la diffusione di queste tecniche è ancora limitata per diversi motivi, tra cui uno dei più importanti è la necessità di previsioni e misurazioni accurate della temperatura indotta per ottimizzare il risultato del trattamento. I metodi di pianificazione della terapia, in grado di stimare la risposta termica dell'area bersaglio, sono fondamentali per regolare la potenza del laser e la durata del trattamento. Inoltre, i sistemi di monitoraggio in tempo reale sono fondamentali per controllare direttamente la temperatura indotta durante i processi termici. La tesi studia l'ottimizzazione delle terapie termiche basate sull'assorbimento dei tessuti da parte delle radiazioni laser per generare un aumento localizzato della temperatura. Lo scopo di questa tesi è studiare un metodo per stimare e controllare la distribuzione della temperatura durante i processi di trattamento laser, aiutando l'oftalmologo nella pianificazione e nel monitoraggio delle terapie termiche. Questo ha richiesto lo sviluppo di un adeguato modello parametrico 3D a occhio intero,

analizzato con il software agli elementi finiti COMSOL Multiphysics, per fornire approfondimenti sull'interazione occhio-laser in vista della proposta di trattamenti personalizzati per ogni paziente. Il modello è composto da due parti: l'interazione luce-tessuto e la diffusione del calore nei tessuti. In particolare, il lavoro di tesi ha sviluppato un "metodo dell'impulso di calore" per recuperare i parametri termici dei tessuti biologici. Basandosi sulla correlazione intrinseca tra proprietà biologiche e risultati termici, la risposta a un breve impulso di calore, non abbastanza intenso da causare danni cellulari, viene adattata alla soluzione analitica dell'equazione di trasferimento del biocalore. La temperatura viene misurata attraverso sensori in fibra ottica basati sui reticoli di Bragg. Il metodo è stato prima convalidato attraverso simulazioni numeriche ed è stato analizzato l'impatto di diversi tipi di incertezze. Sono stati eseguiti test sperimentali su fantocci e tessuti ex-vivo per dimostrare la fattibilità dell'approccio proposto.

Acknowledgements

Special thanks are dedicated to my supervisors, Prof. Guido Perrone and Prof. Gianni Coppa, for their immense patience, important advice and knowledge imparted throughout the thesis project. A kind thanks goes to Prof. Alberto Vallan, for giving me the opportunity to carry out fundamental activities of the research work. I would like to thank Prof. Gian Maria Cavallini for his kind cooperation in experimental tests based on micro-pulsed laser technology.
My immense gratitude goes to CarloAlberto for standing by my side with his special support. A heartfelt thanks is dedicated to my parents for the sacrifices they made to allow me to reach this important life milestone.

"Sono una parte di tutto ciò che ho trovato sulla mia strada."
Alfred Tennyson

Table of Contents

List of Tables

List of Figures

Acronyms

FBG

Fiber bragg grating

NPDR

Non-proliferative diabetic retinopathy

PDR

Proliferative diabetic retinopathy

PRP

Pan-retinal photocoagulation

DME

Diabetic Macular Edema

VEGF

Vascular endothelial growth factor

RPE

Retinal pigment epithelium

DRS

Diabetic Retinopathy Study

ETDRS

Early treatment diabetic Retinopathy Study

CW

Continuous wave laser

AOG

Angle-open glaucoma

ACG

Angle-closure glaucoma

IOP

Intraocular pressure

LPI

Laser peripheral iridotomy

Nd:YAG

Neodymium-doped yttrium aluminium garnet laser

KTP:YAG

Potassium titanyl phosphate/yttrium aluminum garnet laser

FSL

Femto-second laser

SNR

Signal-to-noise ratio

NTC

Negative temperature coefficient

DAQ

Data acquisition system

LASER

Light Amplification by Stimulated Emission of Radiation

TIR

Total internal reflection

NA

Numerical aperture

LED

Light emitting diode

RMS

Root mean square

PDE

Partial differential equation

FEM

Finite element method

RTD

Resistance temperature detector

DSC

Differential scanning calorimetry

Chapter 1

Introduction

Eye health is a key factor in the well-being and health of people across the spectrum of life. Vision is a golden thread running through the Sustainable Development Goals settled by the United Nations for the 2030; from poverty reduction to economic growth and employment, to education and reducing inequalities. According to the World Health Organization's latest estimates, at least two billion people worldwide have vision impairments and at least one billion of these cases could be prevented [1]. Vision disorders involved people at any stage of their life, with the majority being over the age of 50. Increasing life expectancy and global population growth, together with poor access to health care in some low-income countries, lead to estimate a significant increase in the total number of people with low vision by 2050. Visual impairment is recognized as a globally significant health problem involving effects on an individual's personal, economic, and social life. Young children with severe vision disorders can experience lower levels of educational achievement. Adults with eye disease often have lower rates of workforce productivity, and higher rates of depression and anxiety. The leading causes of vision impairment vary significantly among and within countries, depending on the availability of eye care services and their affordability. Globally, the main eye diseases are uncorrected refractive errors, age-related macular degeneration, cataract, diabetic retinopathy, and glaucoma. Considering the growth of the elderly population, the increasing

incidence of these ocular disorders creates a challenging scenario for ophthalmology. The Fig. 1.1 shows how the prevalence of vision loss increases rapidly with age; in fact, age is associated with a higher prevalence of eye diseases, particularly cataracts, age-related macular degeneration, and glaucoma.

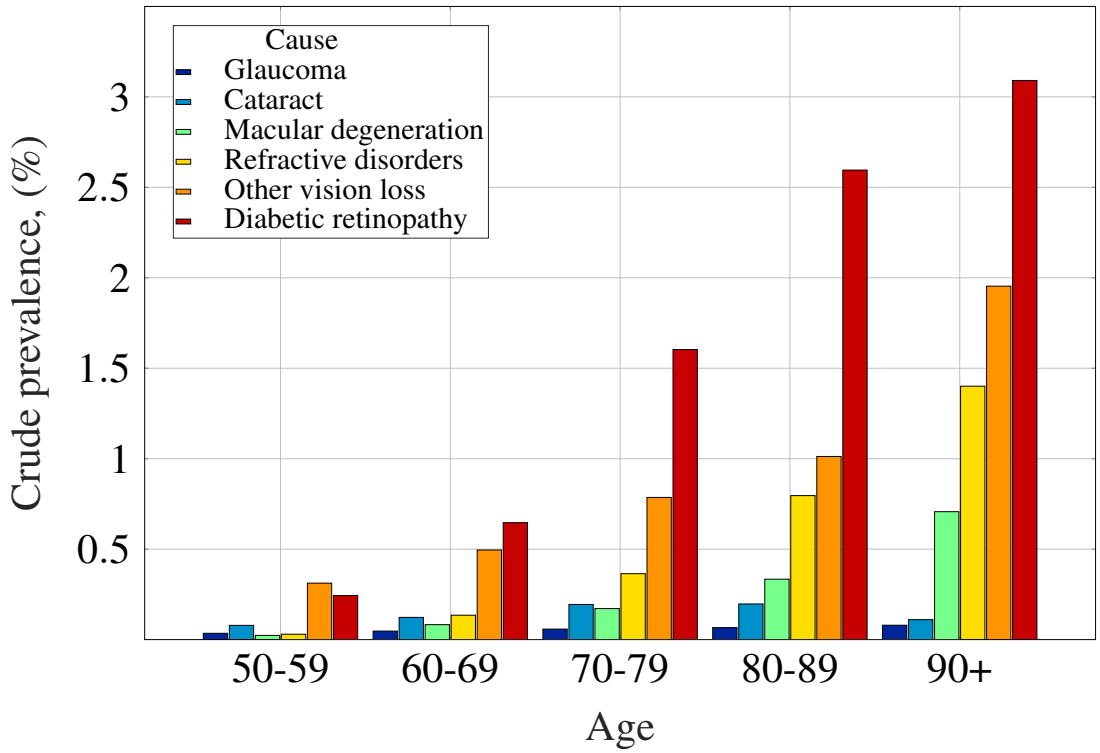

Figure 1.1: Crude prevalence of vision loss, Global, 2020 [2].

In this context, the application of laser technology is essential for eye treatment and diagnostic. Thermal processes in ophthalmology are very promising tools, although it is still necessary to accurately predict and measure the laser-induced thermal effect in order to optimize treatment outcomes. This thesis investigates key principles of thermal therapies based on the absorption of laser radiations by biological tissues. Model-based planning is critical for predicting the thermal response of the target area, and thus for evaluating the optimal laser parameters, such as laser power and duration of beam emission. Moreover, a real-time monitoring tool is necessary to directly control the temperature induced by the laser. The

purpose of the thesis project is to optimize the application of laser technology in ophthalmology. The solutions proposed include: 1. The heat pulse method for thermal biological properties evaluation, based on the analytical solution of the bioheat transfer equation; 2. Numerical simulations using the finite element method of COMSOL Multiphysics; 3. Experimental tests with fiber laser beam delivery and Fiber Bragg Gratings (FBG) sensors; 4. Real-time visualization of laser-induced heat map by data analysis in Matlab. Moreover, a 3D parametric full-eye model has been developed by COMSOL software, to provide important insights about the eye-laser interaction and to supply a personalized treatment for every patient. In the end, this thesis presents a brief introduction on a study aimed at developing an eye simulator, with multi-point fiber optic sensors, to support the ophthalmologists in evaluating possible thermal effects of laser processes, with a particular attention to the case of yellow lasers used to treat macular retinopathies.

Part I

Laser in ophthalmology

Chapter 2

Ophthalmic laser therapy

The LASER - acronym of Light Amplification by Stimulated Emission of Radiation - is one of the greatest inventions of the 20th century. The first working laser was designed by Theodore H. Maiman in 1960 [3], and since then this technology has found application in all branches of physics and science. In particular, the use of laser for medical purposes, and especially thermal therapy, is a young and growing field. Focusing on ophthalmic science, this innovative technology is applied today for diagnostic and for therapeutic purposes. In the field of diagnostics, the technology is used for microperimetric mapping of the macula, confocal scanning laser ophthalmoscopy, optical coherence tomography, and laser retinal doppler flowmetry. Confocal laser microscopy is an excellent diagnostic tool for detecting early stages of retinal changes to recognized early retinal detachment and glaucoma diseases. In the therapeutic field, the main ophthalmic procedures are the treatment of diabetic retinopathy, glaucoma, cataracts, and refractive corneal surgery. This thesis focuses on the use of thermal therapies based on impulsed laser technology, used particularly for diabetic retinopathy and macular edema, which in recent years are among the leading causes of blindness in Western industrialized countries. Subsequent chapters provide to the reader a theoretical background on the main eye diseases and related laser therapeutic procedures.The targets of all eye therapies can be classified into anterior and posterior segments. The anterior segments consist of the cornea, sclera, trabeculum, iris, and lens. The posterior segments are the

vitreous body and retina. The next section presents the ocular component of the retina, which is the key target tissue of new impulsed technologies.

2.1 General retina anatomy and physiology

The retina is a thin layer of the eye structure, consisting of transparent biological tissue permeated with blood vessels. The retina is part of the central nervous system, and its function is to convert an optical image into electrical impulses that are sent to the brain through the optic nerve. The thickness of the retina reaches a minimum value of 80 µm at the level of its anterior limit, the ora serrata, and increases in the antero-posterior direction to a maximum of 400 µm at the macular area. The macula is the anatomical centre of the retina with a diameter of 5.5 mm and provides the maximum central vision. The centre of the macula is the fovea centralis, responsible for highest level of visual acuity, colour vision, and brightness perception. The fovea centralis is thick 100 µm and it is 1.5 mm in size, with the densest concentration of cones and an absence of rods. Foveal cells have a yellowish appearance due to the presence of xanthophyll and beta carotenoid pigment, lutein and zeaxanthin, which protect the cones from high-intensity blue light. The retina has dual circulation: the outer retina is supported by branches of posterior ciliary arteries and the inner retina is supplied by branches of the central retinal artery. Retinal blood vessels are non-fenestrated and maintain the blood-retinal barrier. Anatomically, the retina is divided into several layers, each of which has a distinct function: retinal pigment epithelium (RPE), receptor layer, outer limiting membrane, cell layer, nerve fibre layer, and inner limiting membrane. A schematic cross section of a human retina is shown in Fig. The retina is the most metabolically active ocular component, and its metabolism is regulated by the retinal pigmented epithelium, a barrier tissue layer that regulates the passage of nutrients to and from the retina. The pigmented cell layer is closest to the choroidal membrane and extends throughout the entire optic part of the retina, excluding the optic papilla. The RPE consists of hexagonal, nucleated cells that are rich in fuchsin granules in the form of prismatic crystals; these cells send out fine offshoots that lie between one photoreceptor and another of the underlying layer to transport nutrients, ions, and water. These expansions, which also

contain melanin granules, serve to phagocytize the outermost membranes of the photoreceptors, allowing continuous renewal of the depleted receptor portions, and serve to absorb light that would tend to diffuse from one sensory element to the adjacent one. The receptor layer consists of two types of cells: rods and cones. The rods are used in low-light conditions and are located mainly around the macula. Cones perceive colours in good light and are very close to the fovea. The cell layer consists of horizontal cells, bipolar cells, amacrine cells and ganglion cells. The main function of these cells is to act as the first network with the corresponding receptive fields. Finally, the nerve fibre layer contains the axons of ganglion cells, while the inner limiting membrane forms a boundary between the retina and vitreous body. The Fig. 2.1 illustrate the composition of the retina.

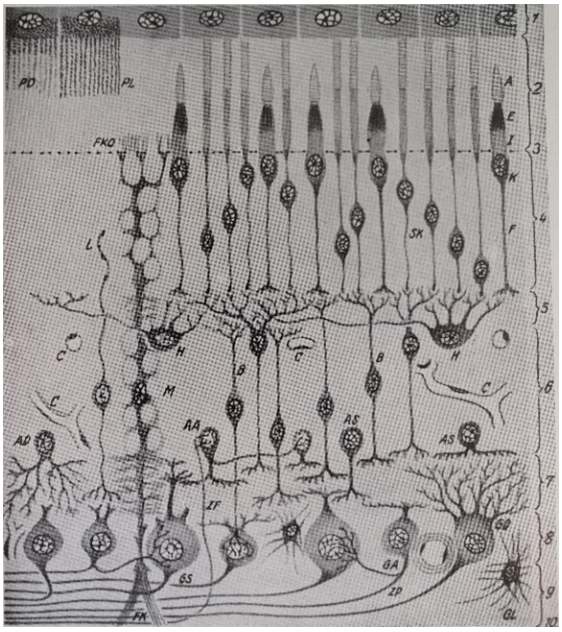

Figure 2.1: Scheme of the structure of the retina: 1) Pigment epithelium; 2) receptor layer; 3) outer limiting membrane; 4-8) cell layer; 9) nerve fiber layer; 10) inner limiting membrane

.

2.2 Diabetic retinophaty

Diabetic retinopathy is a vision disorder caused by retinal damage and is a long-term consequence of diabetes mellitus. The eye disease is clinically classified into non-proliferative (NPDR) and proliferative (PDR) forms, according to the presence or absence of retinal neovascularization. NPDRis the early stage of the eye disease and consists of increased vascular permeability and occlusion of capillaries. The hyperglycemic condition leads to endothelial damage of retinal capillaries and to microaneurysms formation, resulting in hemorrhages deep in the retina, which appear as "spots" on retinal examination. Moreover, capillary occlusion can cause infarction of the eye's layer of nerve fibers, resulting in cotton-wool spots. Consequently, this ischemic condition stimulates retinal cells to release pro-angiogenic factors, such as vascular endothelial growth factor, (VEGF). Therefore, PDR is the advanced stage of diabetic retinopathy, characterized by the presence of neovascularization, in order to bypass damaged retinal blood vessels. However, these new vessels are extremely immature and permeable, originating severe complications, such as vitreous hemorrhage or tractional retinal detachment. Diabetic retinopathy can occur with or without macular edema, (DME). Indeed, the inflammatory cytokines are significantly up-regulated in diabetes and thus chronic inflammation and endothelial damage lead to increased vascular permeability of blood vessels. The pathologic process involved in DME results in the leakage of fluid, deposited within 500 µm of the center of the macula; the hard exudates from edema are waxy, yellow lipid byproducts. Macular edema is a typical disease in more severe cases of diabetic retinopathy, where the increased vascular permeability is more advanced. DME is responsible for most of the visual loss experienced by patients with diabetes[4].

2.2.1 Pan-retinal photocoagulation

Pan-retinal photocoagulation (PRP) is the standard procedure for retinal vascular diseases, including the two main conditions, proliferative diabetic retinopathy and central retinal vein occlusion. The efficacy and benefits of PRP have been established by Diabetic Retinopathy Study (DRS) [5] and Early Treatment Diabetic Retinopathy Study (ETDRS) [6] studies. These two key studies represent the first large randomized, prospective, multicenter clinical trials on the efficacy of retinal laser photocoagulation, demonstrating the efficacy of PRP in reducing the risk of severe visual loss by 60% at 2 years in patients with high-risk PRP and in treating clinically significant macular edema [7]. Recent studies [8] found that anti-vascular endothelial growth factor monotherapy for diabetes is as effective as PRP .However, anti-VEGF therapy requires multiple injections and long-term commitment; moreover, macular edema can be or become anti-VEGF resistant, giving less chance for both the specialist and the patient to manage the disease [9]. Therefore, laser therapy remains the main treatment for retinal vascular diseases.

Therapeutic procedure

Pan retinical photogoagulation therapy involves the application of a photothermal laser in order to reduce hypoxia and reverse the ischaemic drive on the target retinal area. The principle of treatment is based upon the absorption of laser energy radiation by ocular pigments, predominantly in the retinal pigment epithelium and choroid melanin and hemoglobin [7]. The therapeutic procedure sacrifices the peripheral ischaemic retina in order to stabilize the vascular disease and to maintain the central vision. Indeed, the cells of the RPE layer and the photoreceptors are high oxygen-demanding biological components, and thus their selective destruction increases oxygen availability to the remaining retina. The overall lower level of hypoxia results in an under-regulation of angiogenic factors and in a reduction of retinal vascular permeability. Moreover, the effect of the laser creates direct oxygen bridges from choroid to the inner retina, improving oxygenation.
The therapeutic benefit zone of photocoagulation involved peak temperatures of the tissue in the range of 60 °C - 80 °C; higher values can cause

severe damage to the target area, while for lower values the thermal effect is reversible [10]. These temperatures cause the coagulative necrosis with denaturation of cellular proteins, making the retina clear and opaque at the burn site [11]. The standard therapy involved the laser beam to deliberately heat and destroy newly formed blood vessels and nearby retinal tissues. The main wavelengths used for this procedure are 532 nm, green, and 577 nm, yellow. The advantages of these radiations are low intraocular scattering and higher absorption coefficient of oxyhemoglobin compared with deoxy-hemoglobin. Indeed, the absorption of blood and pigmented epithelium at these wavelengths is predominant over that of the rest of the tissue,leading to precise treatment with relatively low laser power [12, 13]. The Fig. 2.2 show the absorption coefficient for the main components involved in the therapy: melanin, hemoglobin, oxygenated hemoglobin, and lutein.
Traditional PRP involved continuous-wave (CW) laser duration between 100 ms and 200 ms, with spot size ranges from 100 µm to 500 µm. The new approach is to reduce the emission time in order to limit tissue damage to the inner retina and heat diffusion into the choroid. The PASCAL® represents a modern semiautomatic scanning system based on a frequency-doubled, optically pumped semiconductor laser, to reduce treatment time, increase patient comfort, and improve the accuracy of treatment. The typical laser parameters for PRP are a square grid of spot size of 200 µm with duration of 10 ms and 20 ms [14].

Well-done and safe laser therapy relies on a fundamental understanding of retinal anatomy. A brief introduction is presented below. In planning laser PRP, retina can be divided into four zones and four quadrants, centred at the fovea area. The four quadrants are: superior, inferior, nasal and temporal. The four zones are: central zone, near periphery zone, mid periphery zone and far periphery zone. In particular, the central area includes the macula and optic disc and should not be treated by the laser. The therapy starts in mid-periphery, the most ischemic area, and involves firstly the inferior quadrant because is a safe area to treat, and the superior retina, which does not involve visual driving function. The nasal quadrant must be treated sparingly to preserve driving visual fuction, and, if disease remains active, the next zone treat is the far periphery, because it contributes to persistent diabetic macular edema and proliferative activity. Finally, treatment of the

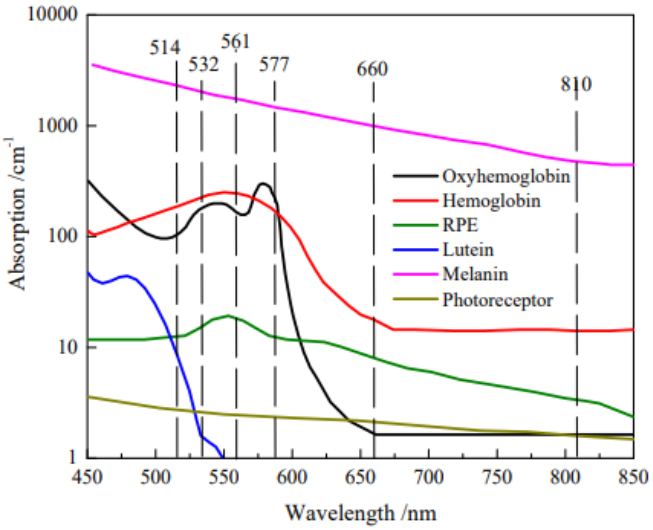

Figure 2.2: Absorption coefficient versus wavelength [15].

near peripheral retina should only be done in the case of persistent pathology activity with florid neo-vascularisation; therefore, it should be done sparingly and with large inter-bruising spacings to spare the visual function [11].

2.3 Modern laser therapy

Since the publication of the Early Treatment Diabetic Retinopathy Study [6], retinal laser photocoagulation has represented the routine tool for clinical management of diabetic macular edema and other retinal conditions. However, conventional laser treatments has several possible side effects and significant disadvantages, including permanent retinal scarring, prolonged treatment time, and reduction in the patient's peripheral vision. In addition, direct action on retinal neovascularization can cause hemorrhage, and late complications of photocoagulation include secondary choroidal neovascularization, subretinal fibrosis, and macular pucker [7].The main problem with photothermal lasers is the damage associated with heat diffusion to the neurosensory retina overlying the pigment epithelium. The severity of the damage is related to the use of excessive powers, long-duration pulses, and

large spot sizes, resulting in painful treatment and loss of vision. Therefore, photothermal lasers do not improve vision, but they stabilize the vascular disease and maintain vision [11]. The development and improvement of laser technology in recent decades, especially in biomedical applications, has led to an evolution in conventional retinal laser therapy with the aim of minimizing retinal damage and adverse side effects while maintaining the excellent therapeutic effect of the conventional approach.In innovative approaches, special attention is focused on changing the laser pulse duration, wavelength and spot size. Some of the new laser treatments in ophthalmology are selective retinal therapy with nano-second laser pulses and micropulsed yellow laser technology. Focusing on the latter, the chapter presents the new treatment procedure along with an initial experimental work on the heat map generated by the micropulsed laser.

2.4 Glaucoma

Glaucoma is a group of eye diseases characterized by damage to the optic nerve, mainly caused by increased intraocular pressure (IOP). The IOP is the fluid pressure of the eye resulting from the balance between the secretion and reabsorption of aqueous humor, which is composed of water and a limited percentage of minerals and proteins. The fluid is produced by the ciliary body and flows from the posterior chamber to the anterior chamber, passing around the lens through the pupil. Finally, the fluid is reabsorbed by the sclerocorneal trabeculate and drains into Schlemm's canal. Under physiological conditions, the positive pressure within the eye range from 10 mmHg to 20 mmHg. The Fig. 2.3 illustrates pathway of aqueous humor which is actively secreted by the ciliary body and eventually exits, mainly through the trabecular meshwork.

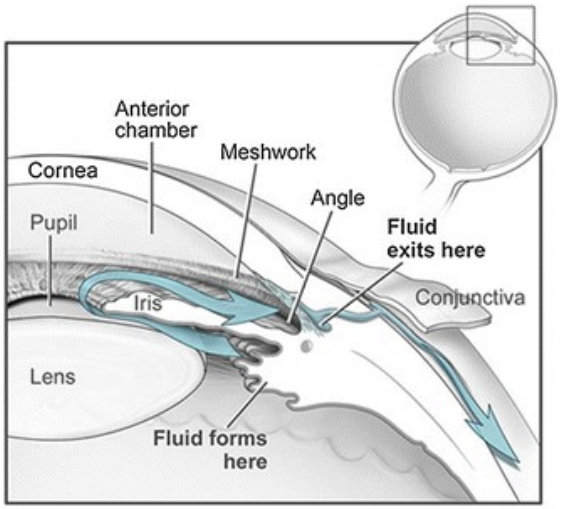

Figure 2.3: The main outflow pathway of aqueous humor from generation to outflow [16].

Glaucoma can be classified as open-angle glaucoma (AOG) or angle-closure glaucoma (ACG). The irido-corneal angle originates from the meeting of the iris plane with the corneal plane, and at the apex of the convexity is the trabecular system. The width of this angle correlates with the presence or possibility of glaucoma development. Narrow-angle glaucoma results in an increased intra-ocular pressure, presenting symptomatic manifestations from the earliest stages. The main cause is the primary pupillary blockage, which obstructs aqueous flow, increasing the intraocular pressure. Open-angle glaucoma is a progressive and irreversible optic neuropathy, manifesting symptomatology only in advanced stages. ACG is caused by the inability of the eye to drain excess aqueous humor, as a result of decreased elasticity and porosity of the sclerocorneal trabecular system.
The main goal of laser treatments in glaucoma is to reduce the IOP to slow down the degeneration of the retinal nerve fiber layer. Therapeutic lasers are used in peripheral iridotomy, iridoplasty, and trabeculoplasty.

2.4.1 YAG Peripheral Iridotomy

Laser peripheral iridotomy (LPI) is the standard first-line method of treating angle-closure glaucoma. Angle closure can occur gradually and intermittently with few symptoms (chronic angle-closure glaucoma) or suddenly and severely with painful symptoms (acute angle-closure glaucoma)[11]. The LPI is the outpatient procedure required for the prevention of acute angle-closure glaucoma attack. The main therapeutic treatment is performed with the neodymium-doped yttrium aluminum garnet (Nd:YAG) solid-state laser, emitting at 1,064 nm [17]. The laser principle effect on tissue is photodisruption, with no thermal process, in order to creates an alternative way for water outflow. The therapeutic procedure involves very short, high-power laser pulses capable of ionizing biological tissue. In this way, a rapidly expanding plasma and cavitation bubble with an explosive effect cause tissue breakdown, relieving pupillary blockage and opening the angle. The treatment focuses on the anterior iris stroma, which is the middle layer of the iris composed of heavily vascularized and innervated connective tissue. Typical laser parameters are a power of 3 mJ and a pulse duration of nanoseconds [11]. The following Fig. 2.4 shows the treatment procedure performed in

narrow-angle eyes to prevent a angle closure attack.

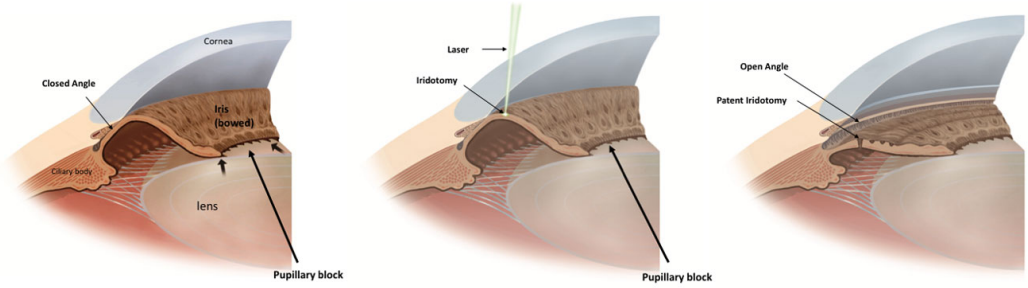

Figure 2.4: Laser peripheral iridotomy [18].

2.4.2 Selective Laser Trabeculoplasty

Laser trabeculoplasty has a key role in open-angle glaucoma treatment. Selective laser trabeculoplasty is an effective therapeutic method to reduce and control intraocular pressure, and is based on stimulation of aqueous drainage by a photothermal effect. Indeed, the therapy acts at the level of the intracellular pigment, melanin, in order to dilate the trabecular meshwork. One typical laser used in the procedure is the potassium titanyl phosphate/yttrium aluminum garnet (KTP:YAG), with a wavelenght of 532 nm. The pulse duration of beam emission is 3 ns, less than the thermal relaxation time of trabecular meshwork melanin (2 µs), in order to prevents heat transfer and damage to surrounding tissues. The amount of energy used, between 0.5 mJ and 1 mJ, is controlled according to the degree of trabecular pigmentation. The therapy involves low energy density on target area and the absorption of laser radiation stimulates biological mechanisms resulting in aqueous outflow.

2.5 Cataratta

Cataracts consists of the progressive loss of transparency and opacification of the natural lens. The crystalline lens is biconvex and transparent, and is enclosed in the capsule, an elastic membrane. The capsule is held in place by the ciliary zonule of Zinn, the structural ocular component that directly holds the lens in place and mediates the movement forces of the ciliary muscle toward the lens for accommodation. The zonular apparatus is a three-dimensional complex of microfibrils, composed primarily of the protein fibrillin, which aggregate into fibers that run from the inner surface of the ciliary body to the outer surface of the lens capsule. Histologically, the lens is composed of fibers arranged radially and in concentric layers. The fibers located in the central part of the lens are denser, non-nucleated, and have a higher refractive index, while the more peripheral fibers are nucleated and have a lower refractive index. Therefore, the change in the optical density of the lens leads to an increased dioptric power. The function of the crystalline is to allow light rays to pass through the eye and to adjust the focus of images on the retina. The natural lens results free of blood vessels and maintains transparency and functionality due to: 1. The composition of the aqueous humor; 2. The chemical and physical balance of lenticular proteins; 3. The integrity of the capsule. Thus, when one or more of these physiological conditions is altered, cataract formation can occur.
Cataracts is a disease that tends to develop gradually until vision is impaired and affects more than half of older people, over 65 years of age. The disease occurs because proteins accumulate in the crystalline, which form an opaque veil that gradually prevents light from reaching the retina. Therefore, in a cataract-affected eye, the lens partially arrests and distorts the passage of light rays, significantly reducing vision and making images foggy and blurry. Cataract surgery is a frequently performed laser treatment in ophthalmology, and an introduction to the traditional and new techniques involved is presented in the next section.

2.5.1 Femtolaser

Phacoemulsification is the traditional cataract surgery. The treatment procedure involved the opening, along the side of the cornea, of a small micro-incision of about 2 mm. Through the aperture, an ophthalmic visco-elastic device is inserted into the anterior chamber in order to replace the aqueous humor and to allow the safe passage of surgical instruments during the procedure. Next, a portion of the anterior capsule of the lens is removed through capsulorrhexis. The crystalline is then fragmented using a torsional ultrasound probe that, through a 'cross' technique, divides the lens in four quadrants, and then the probe performs a cortical aspiration of the fragments. The cataract is removed and a new intraocular lens is implanted. The posterior capsular acts as a support and a case for the artificial lens, and helps prevent vitreous body collapse and subsequent retinal detachment.
The most recent technology approved for ophthalmic cataract surgery is the Femtosecond laser (FSL), working in the deep infrared with by ultra-short pulses from 1,028 nm to 1,053 nm. The key characteristic is the emission of ultra-fast pulses in the temporal domain of femtoseconds (1 fs = 10^{-15}s) [19], resulting in laser energy delivered with preserving the surrounding tissues. That process is based on the emission of a radiation beam with a spot diameter of less then 8 µm, which can be focused at different depths in the eye to treat the desired target area. In particular, the absorption of ocular tissue in the wavelengths FSL results in fundamental laser therapy in corneal and anterior segment surgery. The principal effect on biological targets is photodistruption, that permits perfect cut through a rapidly expanding plasma with creation of cavitation. Multiple cavity bubbles of carbon dioxide and water vapor separete the tissue plane. In Fig. 2.5, the mechanism of photo-destructive action of laser on tissue is schematized.

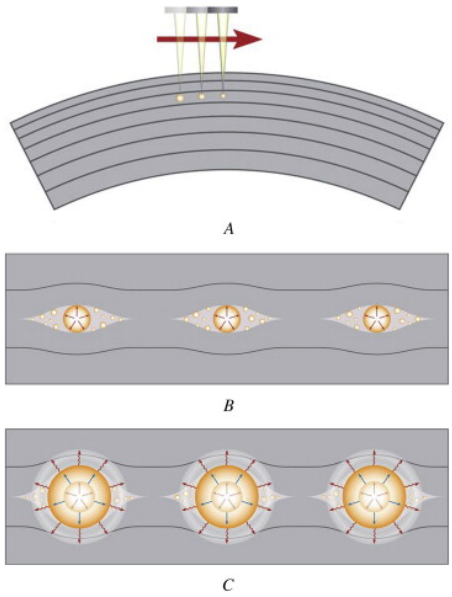

Figure 2.5: The laser surgical tool in ophthalmology is based on microscopic bubbles formation of rapidly expanding plasma. In this way, the application of thousands of pulses defines a plane of tissue cutting [20].

The laser accurately performs capsulorhexis, creating an extremely centered and symmetrical circular capsule opening for better positioning of the new intraocular lens. This technology requires a minimal amount of energy, for greater safety and sparing of ocular tissues, such as the cornea and capsule. In addition, the femtolaser provides surgical accesses with very small and precise reproducible cuts, reducing the risk of postoperative astigmatism and ensuring rapid visual recovery time and quality of vision. Therefore, the most critical steps of cataract surgery (access, capsule opening, and lens fragmentation) are thus performed using the femtolaser, preparing the eye for the next steps of traditional surgery (cataract aspiration and artificial lens insertion).

Chapter 3

Introduction to laser, optical fibers and FBG interrogators

The overall project under which this thesis work was carried out aims at providing the clinicians with support for planning and monitoring laser-based thermal processes. In this context, the heat source comes from the absorption by biological tissues of laser radiation, which is delivered to the target through optical fibers. In addition, the temperature sensing devices used in the experimental validation part are Fiber Bragg Grating arrays. Therefore, it is necessary a brief introduction to lasers, optical fibers and FBG sensors, to give the reader a comprehensive view of the main topic of this research.

3.1 Laser

The LASER - acronym of Light Amplification by Stimulated Emission of Radiation - is a device that emits light by an optical amplification mechanism provided by the stimulated photon emission. Laser beam radiation is characterized by a high degree of spatial and temporal coherence, which means a fixed phase relationship between electric field values at different times and locations. This property accounts for the the possibility to obtain high power density by tightly focusing a laser beam. A laser device requires three building blocks: an active medium, an energy source mechanism (the so-called “pump”), and an optical feedback system. The active medium is the gain source, where photon amplification by stimulated emission is activated. This requires that some atoms or molecules inside the active medium are brought to an excited state by absorbing energy. Under proper conditions it is possible to achieve the so-called "population inversion", in which the excited state level is more populated than the fundamental level, a fundamental requirement for the onset of the laser emission. This energy transfer mechanism takes place through a pumping device in the form of an electrical discharge or another optical source, such as a flash-lamp or a laser diode. Moreover, to enhance the gain process, it is necessary to transform this amplification system into an oscillator through positive feedback. Indeed, an optical cavity formed by two discrete or fiber mirrors, positioned at both ends of the active medium, allows multiple passages of the photons through the laser medium to increase gain. Typically, one mirror is totally reflective to reflect the radiation inside the cavity, while the other, called the output coupler, is a partially reflective mirror in order to transmit part of the photons outside the optical resonator.
To support this introduction to laser, Fig. 3.1 shows a scheme of the first working laser device invented in 1960 by Theodore Maiman.In this laser, the active medium was a ruby crystal and the pump was provided by a flash-lamp.

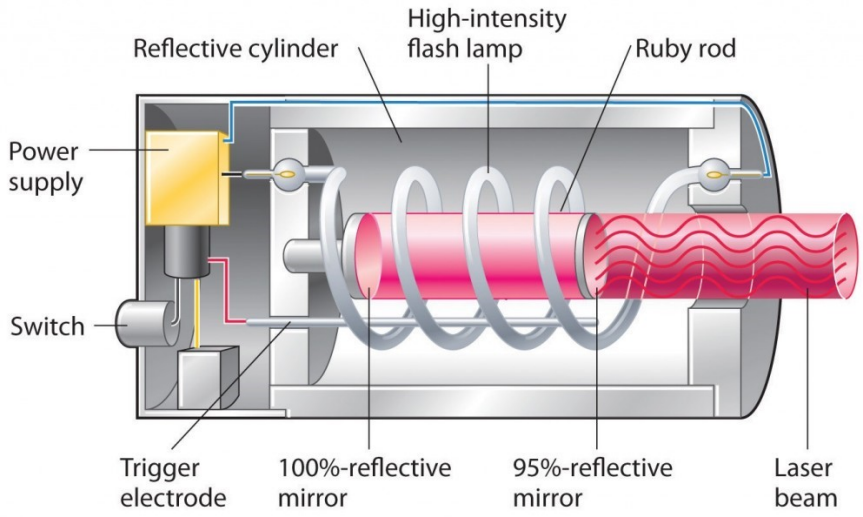

Figure 3.1: Theodore Maiman's ruby laser [21].

Active laser media are gases, dyes, rare-earth doped crystals or fibers, and semiconductors. Therefore, lasers are respectively classified into five main types: gas lasers, dye lasers, solid-state lasers, fiber lasers, and diode lasers. In the next section we will focus on the laser diode as it will be the type of laser used in the experimental part.

Laser diode

The diode laser is a semiconductor device that converts electrical energy into electromagnetic energy, emitting a coherent laser beam. The active medium is a p-n junction diode, made by a semiconductor crystal differently doped in two separate regions: the p-type side contains an excess of holes, and the n-type region contains an excess of electrons. The interface region between the two sides is the p-n junction.
The laser diode consists in a multi-layer structure of semiconductors with different doping and composition, as sketched in Fig. 3.2. The pumping mechanism for stimulated photon emission is obtained by applying a current flowing in the active layer of the diode. The optical resonator consists of two mirror surfaces perfectly perpendicular to the diode junction.
The main advantages of a semiconductor diode are the higher power-to-cost ratio, miniaturization, and availability of a wide range of combination of

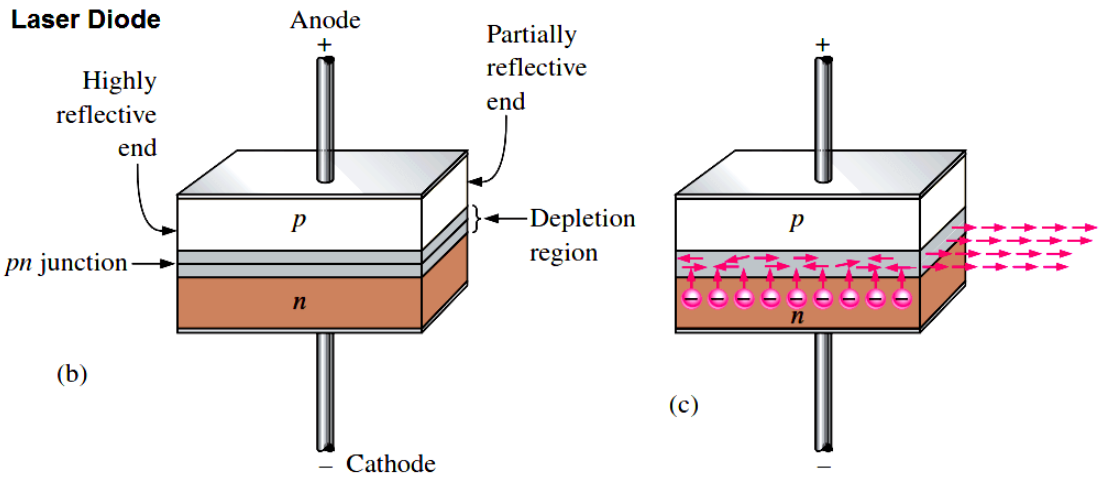

Figure 3.2: Schematic illustration of a laser diode [22].

semiconductor materials that allow the emission at many different wavelengths. Laser diodes are used in many applications such as telecommunications, materials processing, and medical field. In this thesis, laser diodes are employed as the heat source in the simulated medical treatments.

3.2 Optical fibers

Optical fibers are cylindrical optical waveguides consisting of concentric rods of dielectric mate- rials, such as silica glass or plastic, with diameters in the order of tens to hundreds of micrometers. Optical fibers are used to guide laser radiation with low losses, by exploiting the total internal reflection (TIR) at the interface between the inner rod, the *core*, and the outer rod, the *cladding*. External polymeric layers, such as buffer and jacket, can be added over the cladding to provide support and resistance to mechanical stress and to prevent contact between the fiber and the external environment (Fig. 3.3).

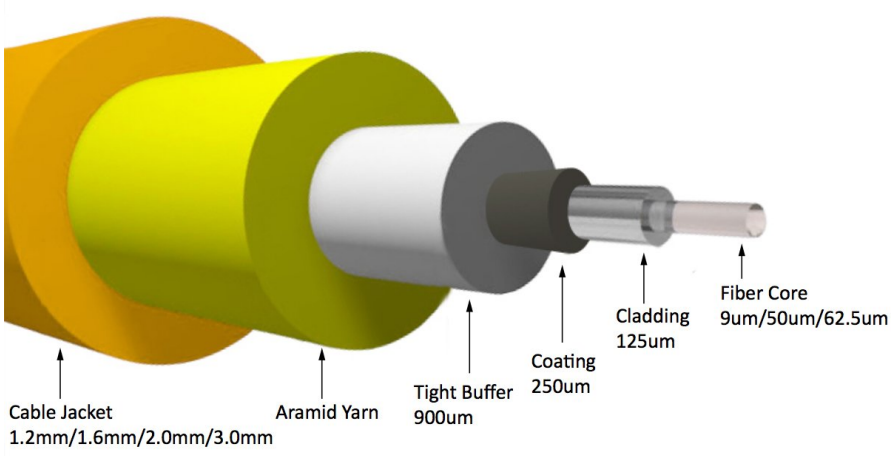

Figure 3.3: Optical fiber structure [23].

Optical fibers guide the laser beam in the core according to the Snell's law, which governs the behaviour of light-rays propagating across an interface between two media. To allow being in the TIR condition the core has a slightly larger refractive index value than the cladding. Indeed, according to the Snell's law of refraction, as light crosses the boundary between two materials, it will be refracted either at a greater angle or a smaller angle depending on the relative refractive indices of each material. If the refractive index of the incident medium is larger than that of second medium, for certain incident angles the beam is in total internal reflection condition, meaning that transmitted field is exponentially decaying (evanescent wave), and the associated power is therefore totally reflected back into the incident

medium. In the case of an optical fiber, the condition of TIR occurs when laser radiation enters the fiber with an incident angle, θi, less than the maximum acceptance angle, θa of the fiber, which is a related to the numerical aperture (NA), a characteristic parameter of the fiber (Fig. 3.4).

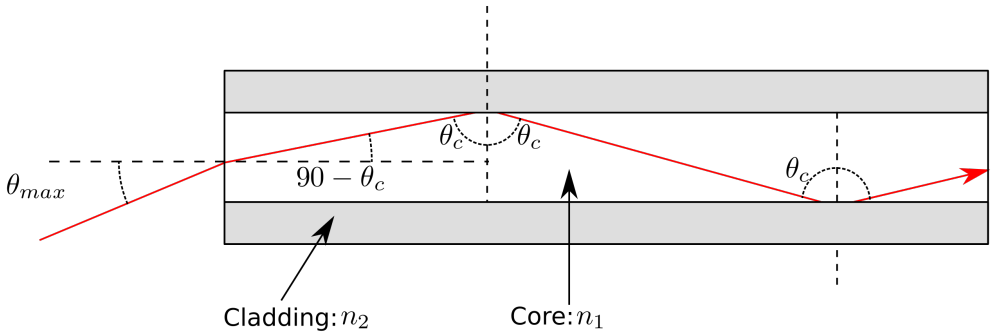

Figure 3.4: Propagation of light through optical fiber [24].

Depending on the fiber core size, operation wavelength, and core-cladding refractive index difference, an optical fiber can propagate one or more electromagnetic field configurations, defined as *mode*. Single mode fibers used at around 1,550 nm, the typical wavelength range of optical communications, have a typical core diameter of 9 um and have beam intensity profiles with Gaussian distribution. On the contrary, multimode fibers have a much larger core diameter, from 50 um to over 400 um, and are characterized by many propagating field configurations, which interfere giving an overall rectangular field distribution. In the experimental part of this thesis work, multimode fibers have been used for the laser beam delivery, while single mode fibers for the fiber-Bragg grating temperature sensors. Depending on the fiber core size, operation wavelength, and core-cladding refractive index difference, an optical fiber can propagate one or more electromagnetic field configurations, defined as *mode*. Single mode fiber has a typical core diameter of 9 µm and have beam intensity profiles with Gaussian distribution. The multimode fiber has a diameter that varies from 50 µm to 62.5 µm and has many propagating field configurations, which interfere giving a rectangular field distribution. In this thesis work, multimode fiber is used in the experimental part, both for laser delivery and for temperature sensors. One of the most important applications of fiber-optic technology in the medical field is the delivery

of laser beams in surgical procedures. Indeed, the ability to focus the laser beam enables precise cutting, tissue ablation, and photocoagulation effect. Another emerging biomedical application of optical fibers is in the field of sensing systems. Fiber-optic sensing exploits the changes in the physical properties of light traveling along a fiber to detect variations in temperature, strain, and other parameters. A fiber-optic sensor is classified as either extrinsic or intrinsic, depending on the sensing location. In an extrinsic sensor, the fiber is simply used to transport light to and from an external optical device, where sensing takes place. In an intrinsic sensor, the physical properties of the fiber undergo perturbations, which change certain characteristics of the light within it. Fiber-optic sensors have developed rapidly because of their small size, robustness to the environmental conditions, electromagnetic immunity, and the ability to implement real-time and remote sensing. In this work, fiber-optic sensors will be applied for accurate temperature measurement during experimental testing. The main types of temperature sensors are fluorescence sensors, interferometric sensors, distributed temperature sensors, emissivity-based sensors, and fiber Bragg Gratings. In particular, the focus in the thesis is on FBGs, which represent the most promising technology for heat treatment monitoring due to their unique combination of technological maturity and sensing performance.
The biomedical applications of the thesis do not involve the use of electromechanical sensors; in fact, the acquisition of metallic systems causes absorption of laser light, resulting in large artifacts and perturbations. Fiber optic temperature sensors do not produce artifacts in presence of laser radiations and their main advantages are the mall size, electromagnetic immunity, and the possibility of real-time detection.

3.3 Fibre Bragg Gratings

Fiber Bragg gratings are a periodic perturbation of the refractive index inscribed in the core of an optical fiber, as sketched in Fig.3.5.
This results in a wavelength sensitive response for which all the spectral

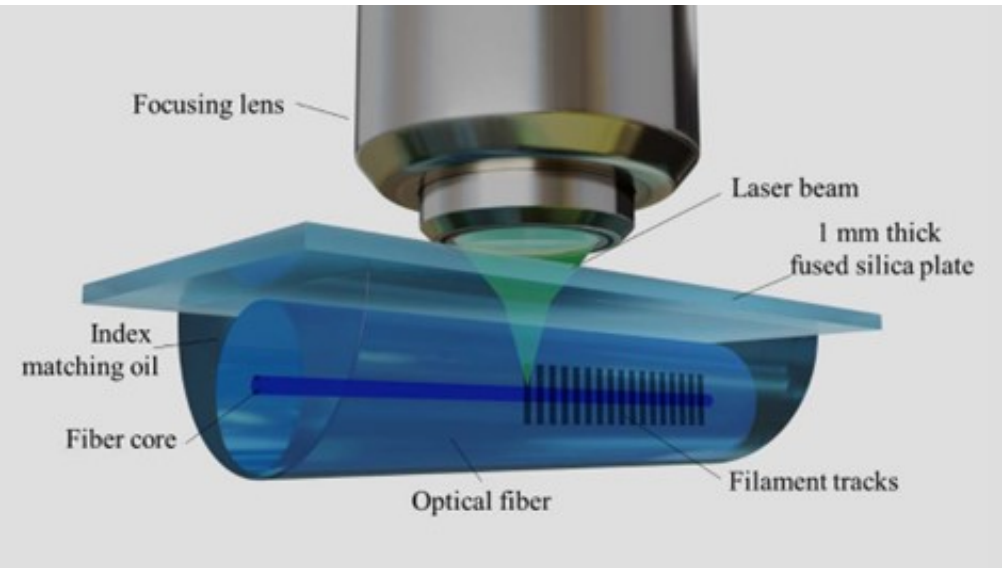

Figure 3.5: Periodic refractive index change by femtosecond laser writing in the fiber core waveguide [25].

components of broadband light are transmitted except for those satisfying a specific relation with the period of the perturbation, which are reflected. Traditional FBG fabrication methods are based on the mechanism of photosensitivity, whereby the refractive index of the fiber core increases during exposure to an intense UV light source. More recent fabrication approaches instead rely on the local modification of the refractive index with ultra-short pulses generated by a femtosecond laser. There are three FBG inscription main techniques: the interferometric technique, the point-by-point technique and the phase mask technique.

- The interference lithography method requires two UV laser beams and exploits the interference between them to generate a periodic field intensity distribution. The procedure involves an initial ultraviolet laser, which is then split into two parts. Subsequent recombination of the

ultraviolet beams occurs at a given angle, defining the desired periodic interference pattern. The interference pattern induces a modulation of the refractive index in the fiber core with the same spatial periodicity. In this way, fiber Bragg gratings at specific wavelengths are obtained by changing the intersection angle between the two writing beams.

- The phase mask technique is widely used for the fabrication of reproducible Bragg gratings. The phase mask is a diffractive optical element that spatially modulates the laser writing beam. The mask can be created holographically or by electron beam lithography in a high-quality fused silica that is transparent to the ultraviolet wavelength. This photographic pattern induces a refractive index modulation of the photosensitive fiber core located immediately behind the mask. Fiber Bragg gratings at specific wavelengths require different types of phase masks.
- The point-by-point technique is based on a laser pulse to change the fiber properties. In particular, the variation of the refraction index is induced along the fiber core with an ultra-fast laser. The femto-second laser beam emit pulses with a very high energy, with high spatial and temporal resolutions. During the writing process, the fiber is translated in the parallel direction to through a distance corresponding to the grating pitch. This method simplifies writing multiplexed sensor arrays because of its flexibility in choosing the period of the FBGs.

The specific wavelength that is reflected by the sensor is called the Bragg wavelength, which is related to the period of the perturbation through the relationship:

$$\lambda_B = 2n_{eff}\Lambda \tag{3.1}$$

where λ_B is the Bragg wavelength, at which the reflection peak is centered, n_{eff} is the modal effective index and Λ is the refractive index modulation period.
Bragg grating sensors are sensitive to strain because of the linear expansion

effect involving the grating period and the refractive index change due to the photo-elastic effect. Similarly, fiber-optic sensors are sensitive to temperature due to thermal expansion and the thermo-optic effect of the fiber material[]. A sensitivity analysis is reported to understand the relation between the temperature and the strain variation, and the Bragg wavelength shift. To this purpose, it is necessary to take the differential of previous equation:

$$d\lambda_B = \left[\frac{\partial}{\partial \varepsilon} 2n_{eff}\Lambda\right] d\varepsilon + \left[\frac{\partial}{\partial T} 2n_{eff}\Lambda\right] dT \tag{3.2}$$

The relative spectrum shift is described by the following equation, dividing by equation 3.1:

$$\frac{d\lambda_B}{\lambda_B} = \left[\frac{1}{\Lambda}\frac{\Lambda}{\varepsilon} + \frac{1}{n_{eff}}\frac{n_{eff}}{\varepsilon}\right] d\varepsilon + \left[\frac{1}{\Lambda}\frac{\Lambda}{T} + \frac{1}{n_{eff}}\frac{n_{eff}}{T}\right] dT \tag{3.3}$$

The right term in the equation is the sum of the effect of strain with the effect of temperature on the relative Bragg wavelength variation. Specifically, strain and temperature change the grating period Λ and, through the photo-elastic effect, change the n_{eff} value. The macroscopic equation of Bragg wavelength shift is:

$$\Delta\lambda_B = K_\varepsilon \cdot \varepsilon + K_T \cdot T \tag{3.4}$$

where, for optical fibers made by silica material, K_ε = 1 pm/$\mu\varepsilon$ is the strain sensitivity; K_T = 10 pm/°C is the temperature sensitivity.

The cross-sensitivity of strain and temperature of fiber sensors must be taken into account during biomedical applications, especially as it is necessary to selectively discriminate the two contributions.
The Fig. 3.6 shows a schematic illustration of the sensing mechanism on which Bragg grating sensors are based.

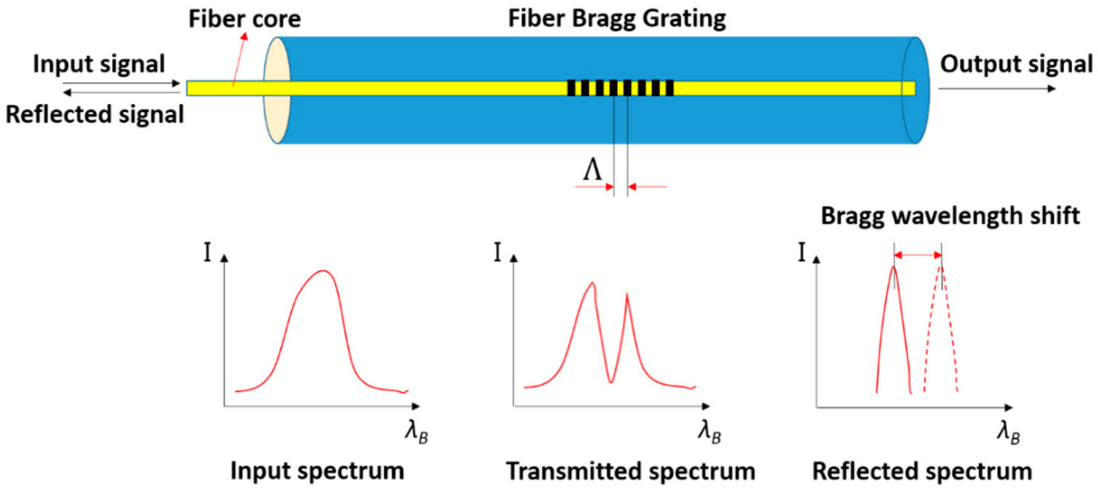

Figure 3.6: Scheme of the sensing principle of Fiber Bragg Gratings [26].

3.4 Introduction to FBG interrogators

An FBG interrogator measures the wavelength associated with the light reflected from the optical sensors, in static and dynamic monitoring conditions, allows extracting some key features (e.g., the peak wavelength), and transfers these data to a remote PC. Thanks to the multiplexing capability of FBGs, sensor arrays formed by multiple gratings inscribed at different points a long a fiber can be interrogated in a single acquisition, performing a distributed measurement. Reading an FBG sensor is complicated because the sensed quantity is encoded in the wavelength; therefore, a high resolution requires the capability of measuring small wavelength changes, in the order of picometers.

A first method for interrogating FBG sensors is to use a broadband light source, generated by a super-luminescent LED or by the amplified spontaneous emission, and an optical spectrum analyzer or a spectrometer. The light source feeds the grating through an optical circulator, which is a device that allows separating at two different ports incident and reflected light beams. The reflections from all sensors are then acquired by an optical spectrum analyzer or a spectrometer, from which the Bragg wavelength

peaks reflected are extracted. The spectrum analyzer or the spectrometer act as a tunable filter, which works as a narrow-bandwidth optical filter able to sweep all wavelengths. The filtered output signal is detected by a photodetector and then sent to a trans-impedance amplifier, which converts the current to an analog voltage, proportional to the optical power associated to the specific wavelength. The second method for interrogating the FBGs is to use a tunable laser to generate a wavelength swept narrow-band light source. The laser is tuned to cover and explore the desired wavelength range for sensor interrogation. The incident light is reflected when the wavelength of the laser matches the Bragg wavelength. In this way, the method involves spectral filtering of the light before sensor interrogation, and the reflected light is focused directly on a photodiode. Unlike the previous source type, in the tunable laser-based system, the high-power source always has the same intensity for all the wavelengths it sweeps, providing a higher signal-to-noise ratio. In the next section, is presented an introduction to a tunable laser-based system used to provide the peaks tracking during the experimental tests.

MICRON OPTICS HYPERION si155

Micron Optics HYPERION si155, by Luna Technologies, is an FBG interrogator; it relies on the tunable laser approach. The Micron Optics provides reliable and accurate measurements of hundreds of sensors through four parallel channels. The device specifications are a wide wavelength range from 1,500 nm to 1,600 nm, a resolution of 10 pm and a maximum acquisition rate of 10 kHz. The Fig. 3.7 show the device.

Figure 3.7: MICRON OPTICS HYPERION device.

The device is compatible with the user interface *ENLIGHT Sensing Analysis Software*, which provides tools for analyzing optical sensors and managing instrument settings. Moreover, the software enables signal spectrum display and automatic spectral peak detection in real time, for each channel simultaneously. The Fig. 3.8 and Fig. 3.9 show the software user interface;in particular, the first and fourth channels detect 3 and 20 peaks, respectively

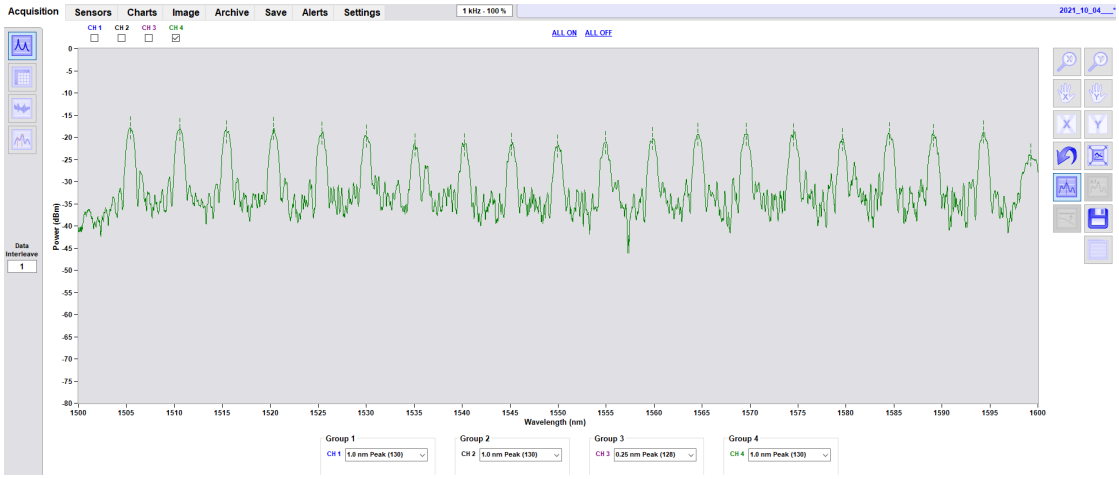

Figure 3.8: User interface of ENLIGHT Sensing Analysis Software.The spectrum of the fourth channel is displayed.

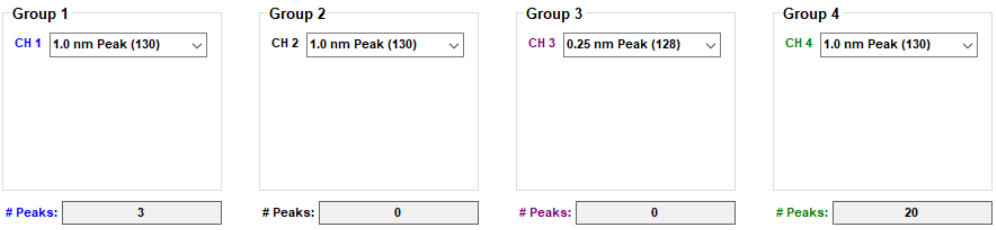

Figure 3.9: User interface of ENLIGHT Sensing Analysis Software.The spectrum of the fourth channel is displayed.

3.4.1 Real-time monitoring method

The section presents an engineering tool aimed at monitoring and controlling the heat therapies in ophthalmology. The purpose is the real-time visualization of the temperature map generated in the target area by the laser source. Graphical visualization of the temperature distribution through ENLIGHT is only possible during data post-processing, as the sensing software only allows real-time data storage. Therefore, to ensure instantaneous feedback on the therapy-induced thermal effect in the localized target zone, a code has been created in Matlab to communicate directly with the MicronOptics. The interaction with the device is through a remote command interface. Specifically, a socket interface is used on several specific ports to exchange

commands and responses, and to stream data. The developed program receives in real time the spectral peaks identified in the active channels of the MicronOptics. The initial peak wavelength values are saved for each channel and used as a reference to calculate the Bragg wavelength shift, for each sampling instant. The initial temperature is set by the user and the thermal distribution is obtained according to the Eq. 3.4, in which the effect of strain is considered negligible. A color map linearly associates heating or cooling values with an RGB color code. Graphical display of temperature map is possible for all four available channels. The Bragg grating is represented by a rectangular shape filled with the color relative to the detected temperature. The time required for real-time visualization of the thermal effect in results in an acquisition frequency of about 10 Hz. The program shows the temperature for each FBG array, indicating the associated channel number and the amount of peaks detected. The developed GUI allows the acquisition to be stopped by a stop button. The data are saved in special structures, divided according to the number of channels involved, for the post-processing of the results. The Fig. 3.10 displays the temperatures of channels one and four.

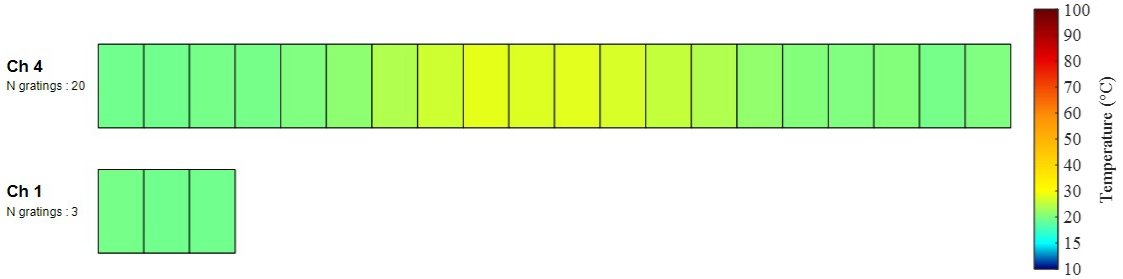

Figure 3.10: Temperature detected from FBG array during real-time acquisition.

Heat treatment is monitored by displaying the thermal map generated in the target zone.

Part II

Simulation activities

Chapter 4

Multiphysics simulation of laser-eye interaction

Although the new micro-pulsed laser technology has already demonstrated several advantages, proper treatment protocols are needed to be used first for planning and then for real-time monitoring. The purpose of this thesis is to study a method to estimate and control temperature distribution during laser treatments, supporting ophthalmologists in thermal therapies. In this chapter is presented the development of a suitable 3D eye model analyzed with the Comsol multiphysics finite element software. The goal is to provide insights about the eye-laser interaction for evaluating customised treatments to each patient. The model is composed of two parts: the light-tissue interaction and the heat diffusion in the tissue.

4.1 3D Eye Model

The simulation activity involved the development of a parametric 3D whole-eye model to study the laser-induced effect on the biological tissue of the specific patient. Indeed, there is a significant inter-individual heterogeneity in terms of thermo-physical tissues behaviour. Focusing on the thermal properties, the intra-patient parameter variability depends on the organ and tissue of interest. To create an accurate model of the eye, a complete

description of the organ is considered and several physical phenomena are taken into account. Ocular structure involves several physical aspects to be evaluated, such as fluidics of aqueous humor, optical behavior of the lens material and cornea, and mechanical deformation in the process of accommodation. As a first approximation, the study analyzes the main focusing phenomena of the lens. Since the heat source is generated by the absorption of the laser beam by the tissue, particular attention is dedicated to the optical properties of layers. The presence of heat transfer due to convection on the corneal surface is considered.

Eye geometry

The human eye dimensions vary among individuals depending on multiple factors, such as the age [27]. Therefore, the model considers the Gullstrand-Le Grand standard dimensions on the trasverse plane, resulting in a vertical dimension of 23 mm and an horizontal diameter along the pupillary axis of 24 mm [10]. The eye is divided into two parts: the anterior segment with the cornea, the anterior chamber and aqueous humour, the lens and the vitreous humour; the posterior segment includes a portion of vitreous humour, retinal layers and the sclera. One main component of the eye dioptric apparatus is the crystalline, that focuses the light rays on the retina. The 3D model considers a biconvex lens with a diameter of approximately 10 mm and an axial thickness of 4 mm. The retina structure is modeled by three key layers: the neural retina, the retinal pigment epithelium (RPE) and the choroid. The neural retina contains photo-receptors and neurons, to encode and transfer visual information to the neural system. The RPE cells help to deliver nutrients to the neural layer and to transport the metabolic outputs to the choroid. The high concentration of pigments in this region, such as melanin, leads to an high absorption of wavelengths. To develop a realistic eye model, we incorporate a single 190 µm thick neural retinal component. The RPE layer thickness varies between 6 µm and 15 µm depending on the individual, and it is assumed to be 10 µm [10]. The choroidal circulation accounts for 85% of all ocular blood flow [28], and during heat transfer in thermal treatments, the choroid acts as a heat sink through conduction and blood convection. The concentration of melanin in the choroid differs between

individuals and a standard pigmented layer of 100 µm is considered. The thickness of the choroid with or without the 100 µm pigmented layer is taken as 0.5 mm. The sclera is the fibrous membrane that protects the eyeball, and has a maximum thickness of 1.5 mm at the exit of the optic nerve, while it thins in the anterior portion to 0.3 mm. In that model, size is considered constant and equal to 0.5 mm. The geometry of the components of the eye model is shown in the Fig. 4.1.

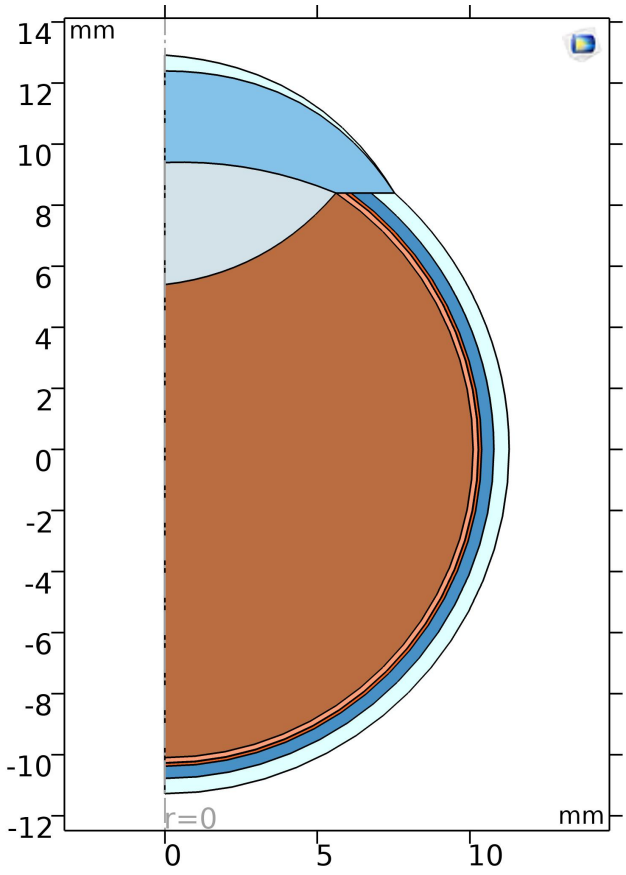

Figure 4.1: Eyeball Geometry

The geometry of the model is divided into eight homogeneous eye domains, and it is assumed symmetrical with respect to the pupillary optical axis. The thermal and optical properties of ocular domains are listed in Tab. 4.1 and Tab. 4.2.

Table 4.1: Physical properties of eye model components [10, 12].

Thermal property			
Ocular domain	Conductivity, (W/mK)	Specific Heat (J/kgK),	Density, (kg/m^{-3})
Cornea	0.58	4178	1050
Aqueous	0.58	3997	1000
Lens	0.4	3000	1050
Vitreous	0.603	4178	1000
Neural retina	0.628	4190	1000
RPE	0.603	4178	1000
Choroid PC	0.58	3840	1060
Choroid	0.58	3840	1060
Sclera	0.603	4178	1000

Table 4.2: Physical properties of eye model components for yellow wavelength, 577 nm [10, 12].

Optical property			
Ocular domain	Absorption coefficient, (1/m)	Refractive index, real part	Depth, (mm)
Cornea	518	1.376	0.52
Aqueous	17	1.336	3
Lens	29	1.41	4
Vitreous	0.08	1.2	15.5
Neural retina	421	1.385	0.17
RPE	100000	1.45	0.01
Choroid PC	100000	1.4	0.1
Choroid	15000	1.4	0.4
Sclera	400	1.41	0.5

Ray tracing

The ray optics module of COMSOL software is used to track a collimated beam, with parallel incoming rays emitted from an infinitely distant source. The refractive properties of the lens and of the eye component are listed in Tab.3. The laser design results in different intensity beam profiles,each of which leads to specific temperature distributions in the treatment spot. In this section, the effect of a laser radiation with Gaussian intensity profile is investigated. The rays propagate through the human lens along the z-direction, perpendicular to the retina, and the simulation considers the spatial intensity decay due to absorption by all eye components. Indeed, the pre-heating of anterior tissues is taken into account based on the optical property for each domain. In simulations of heat transfer of thermal therapies, a collimated source laser beam is considered, which is focused through an external plano-convex lens placed anterior to the cornea. The Fig. 4.2 show the spot diagram of the focused incident beam on the retina layer. The beam is shown in micrometers and corresponds to the RMS value relative to the average of the beams.The simulated beam spot radius incident to the retina

is approximately 500 µm.

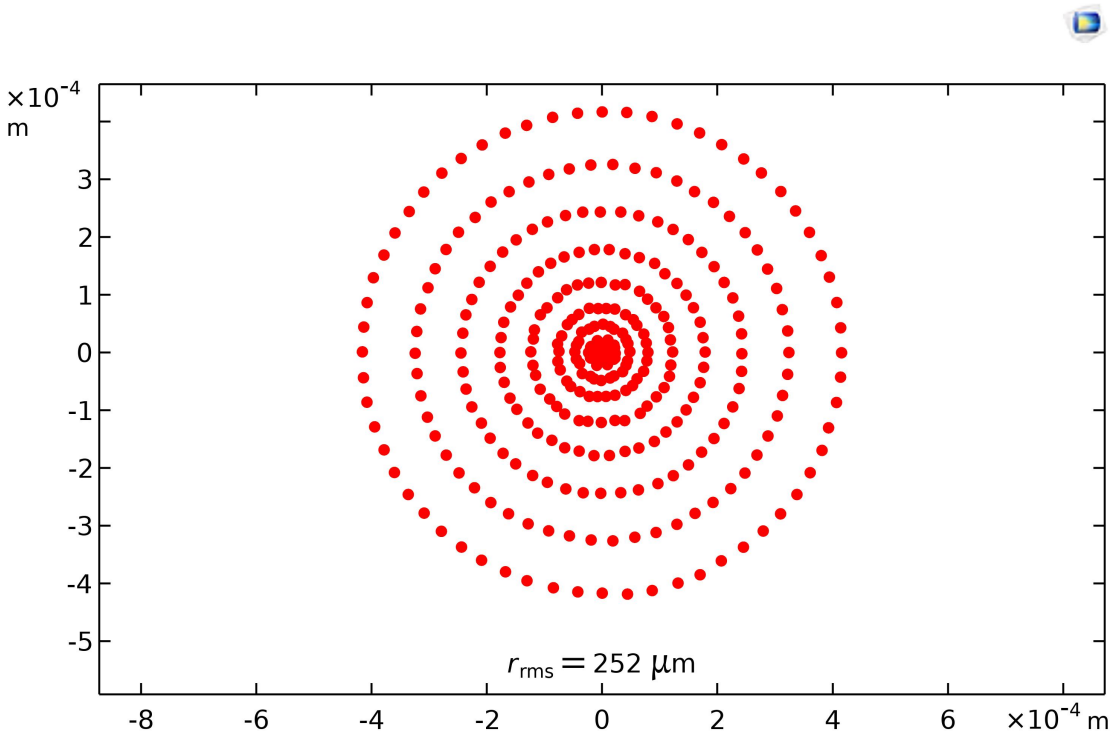

Figure 4.2: Spot size of the focused Gaussian beam. RMS ray radial position relative to average over rays, expressed in µm.

Bioheat Transfer

The heat transfer from the laser source to the eye tissues is analyzed through the Bio-heat transfer physics module of Comsol Multiphysics. Finite element analysis methodology is used to evaluate the model thermal response respect to time and to the three-dimensional space. In the interaction between the laser and biological tissue, the heat source is generated by the absorption of the electromagnetic energy by the eye components. Indeed, each domain of the model is characterized by a complex-valued refractive index, where the modulus of the imaginary part represents the extinction coefficient. The extinction coefficient is the optical attenuation model that evaluates and quantifies the energy absorbed by tissues. The parameter is related to the absorption coefficient of the ocular domains, which in turn depends on the wavelength of the laser. During the application of laser beam, the tissue also redirect some of the incident energy, through the phenomenon of scattering, which, to a first approximation, is considered negligible. Heat transfer theory regulates temperature evolution in tissues based on the biological heat transfer equation, which will be discussed in detail in Chapter 6:

$$\rho C \frac{\partial T}{\partial t} = \nabla(k\nabla T) + \rho_{\mathrm{b}} C_{\mathrm{b}} w_{\mathrm{b}} (T_{\mathrm{b}} - T) + Q_{\mathrm{met}} + Q \tag{4.1}$$

where the left-side of the equation is the time-dependent term, while the first, second, third and fourth term of the right side are heat conduction, heat dissipation by blood flow and metabolic heat source (Q_{met}), and external heat source (Q_{laser}). In the time scale of the simulation of few hundred of ms, the metabolic heat generation within the ocular tissues is assumed negligible [10]. Several studies have examined the effect of thermal convection through blood perfusion of the eye, most notably the analysis by Welch et al [29] explored the contribution of choroidal blood perfusion considering a constant heat transfer of 65 W/m^2. This work found no significant heat loss through blood perfusion in the time scale of photo-coagulation therapy. An important observation comes from the study of Sandeau et al [30], in which the heat loss term is discussed in relation to the exposure duration; the results show a temperature change of less than 1 °C with a pulse duration of 500 ms, or less than 2 °C using 60 s. The eye initial temperature is set to 37 °C throughout the computational domain and this value is related to the

boundary condition of the simulated volume. The ambient temperature is set to 20 °C. Convective heat flux at the cornea surface with external ambient is considered.

4.1.1 Simulation of laser therapy

In the section, are presented the results of laser thermal effect on eye model by the simulation with finite element method. The Fig. 4.3 show the interaction between the laser and 3D model, with a total source power of the Gaussian beam of 150 mW.

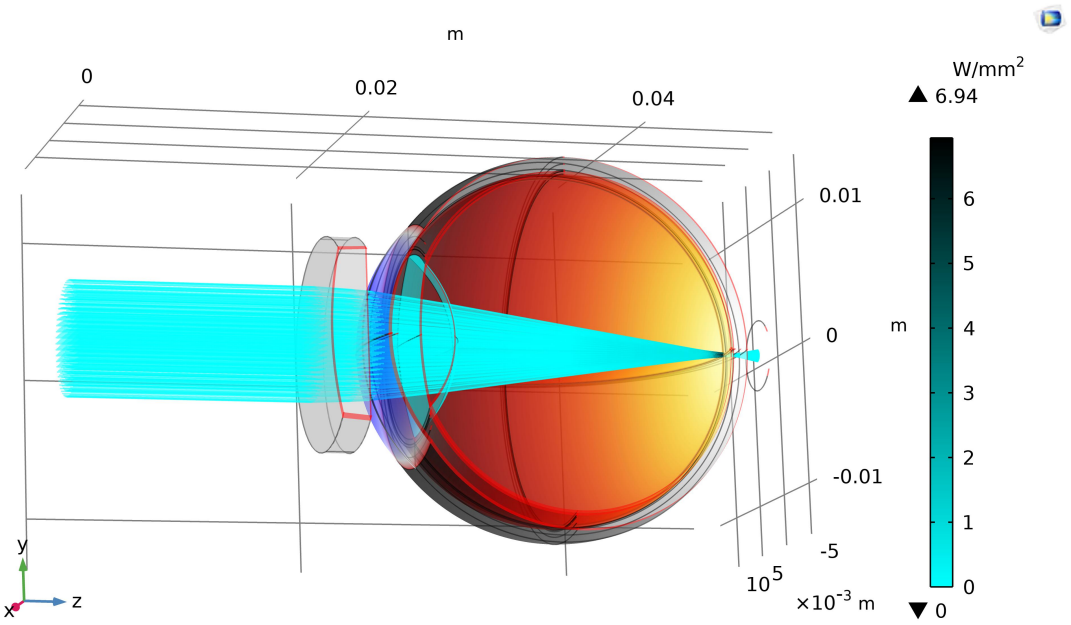

Figure 4.3: Beam tracking and focusing on the retinal layer.

The following plot in Fig. 4.4 show the thermal effect on retina layer. In particular, the great absorption is on RPE layer. The total laser power is 150 mW and the duration of continuous emission is 100 ms.

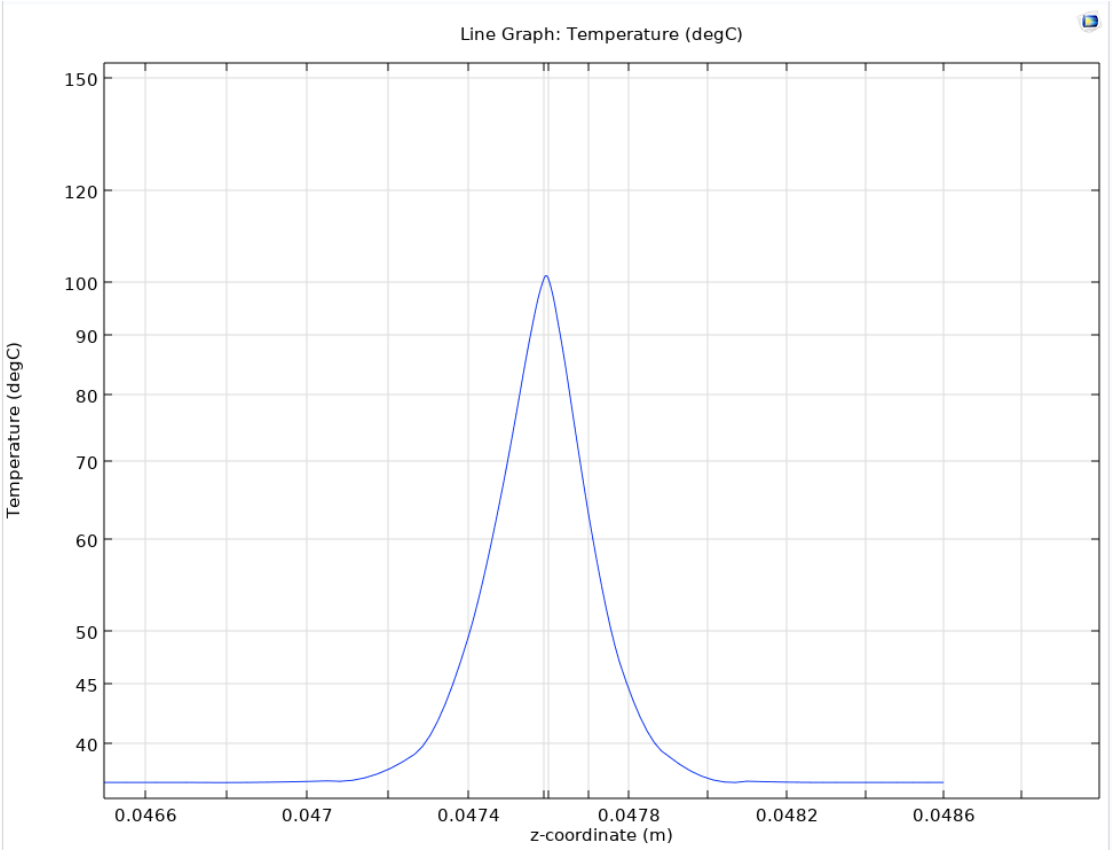

Figure 4.4: Temperature distribution along z-axis with 500 µm of spot laser.

The Fig. 4.5 show an example of heat map on eye retina surface.

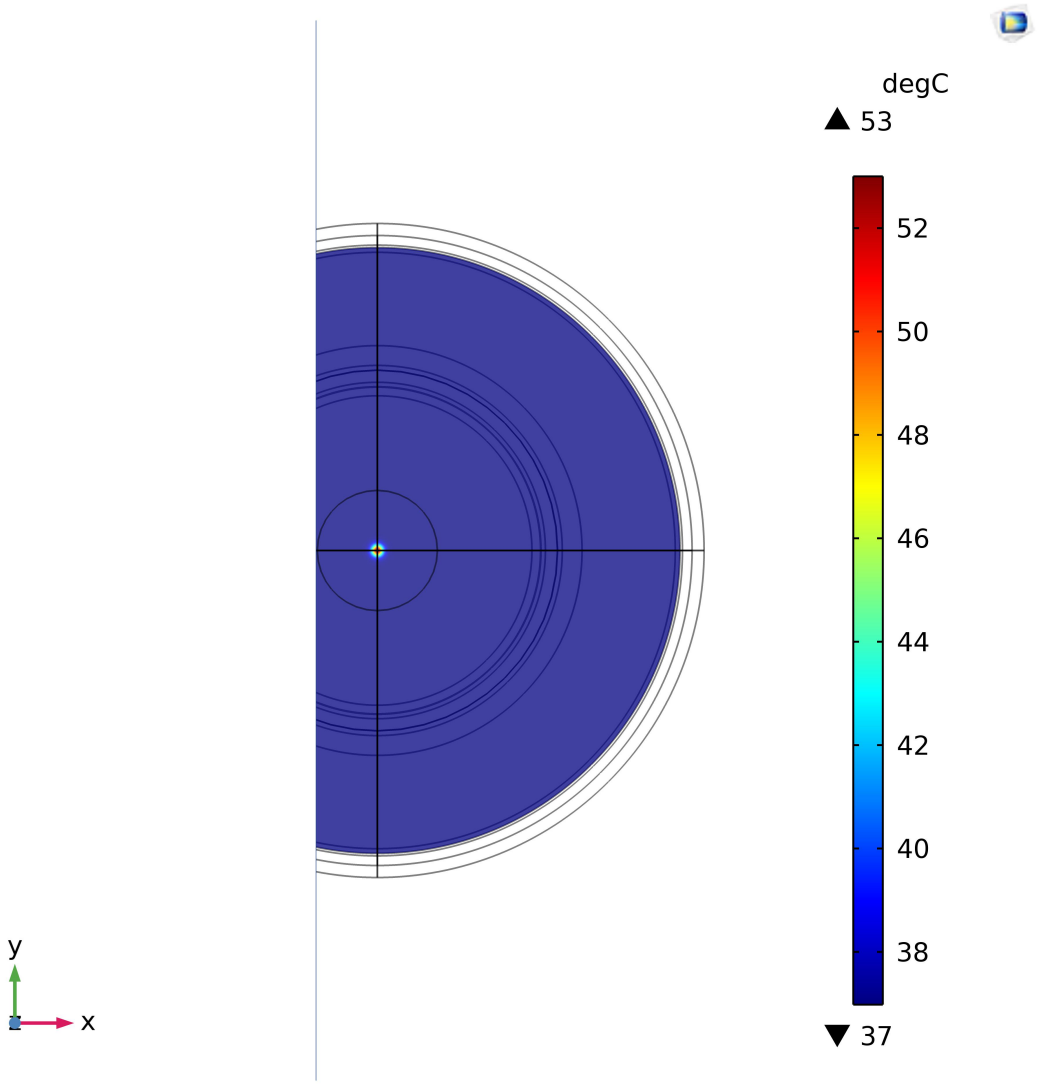

Figure 4.5: Temperature heat map on RPE model surface

Chapter 5

Bioheat transfer equation

This chapter is dedicated to the fundamental concept of heat transfer in biological tissues. The differential Fourier heat equation is introduced, and the 3D Green's function is presented as a closed-form solution of the heat equation.

5.1 Laser - tissue interaction

In the first decades following Maiman's invention of the laser device, many studies were conducted on the potential interaction effects between various types of lasers and tissues. Currently, five categories of interaction types are mainly classified: photochemical interactions, photothermal interactions, photoablation, plasma-induced ablation and photodestruction. In this thesis project, we will study laser-tissue photothermal interaction as it is widely used in ophthalmology to treat retinal diseases such as retinitis pigmentosa, choroidal melanoma, central serous chorioretinopathy, diabetic retinopathy, and age-related macular degeneration. The photothermal interaction defines a large group of tissue effects, where the increase in local temperature is the significant parameter variation. Depending on the treatment duration and on the peak value of the tissue temperature achieved, different effects like coagulation, vaporization, and carbonization may be distinguished [31].

The lowest temperatures, at which biological tissues are thermally affected, range from 42 °C to 50 °C. In this temperature range, conformational changes of molecules, accompanied by bond destruction and membrane alterations, are summarized in the single term hyperthermia.
At 60 °C, the denaturation of proteins and collagen occurs, which leads to coagulation of tissue and necrosis of cells. The corresponding macroscopic response is a visible paling of the tissue.
At 100 °C, water molecules contained in most tissues start to vaporize. Only if all water molecules have been vaporized, and laser exposure is still continuing, the increase in temperature proceed.
Finally, at temperatures exceeding 100 °C, carbonization takes place which is observable by the blackening of adjacent tissue and the escape of smoke.
The spatial extent and degree of tissue damage primarily depend on laser intensity, exposure time, and position of the target zone inside the tissue. The deposition of laser energy is not only a function of laser parameters but it also strongly depends on optical tissue properties like absorption and scattering coefficients. In biological tissue, absorption is mainly due to the presence of free water molecules, proteins, pigments, and other macromolecules and it strongly depends on the wavelength of the incident laser radiation [15]. In Tab. 5.1 the local temperature and the associated tissue effects are listed.

Table 5.1: Thermal effects of laser radiation [31].

Laser-tissue interaction	
Temperature, (°C)	Biological effect
37	Normal
42-50	Hyperthermia
60	Coagulation
100	Vaporization
> 100	Carbonization
300	Melting

5.2 Fundamentals of Bioheat equation

The heat propagation is a process of thermal energy transfer from media, or between parts of the same medium, at different temperatures. The driving force of the phenomenon is the difference of temperature.
Heat transmission occurs in general according to three main mechanisms: conduction, convection and radiation. These physical processes often coexist, but the prevalence of one of them is observed depending on the medium in which heat transfer occurs. In particular, conduction happens in solids, convection in liquid or aeriform, radiation in aeriform and in vacuum.
Within the human body, each biological element is in direct contact with other biological elements and perfused by various fluids, e.g., blood. So, heat transfer occurs by conductive and convective heat exchange.
In order to describe phenomena useful for biomedical applications, it is essential to obtain an equation that allows the description of the overall heat transfer in tissues or in organs. One of the most recognized models that predict heat transfer in biological tissues is Pennes's bioheat equation, which is based on the Fourier conduction law:

$$\rho C \frac{\partial T}{\partial t} = \nabla(k\nabla T) + \rho_{\mathrm{b}} C_{\mathrm{b}} w_{\mathrm{b}} (T_{\mathrm{b}} - T) + Q_{\mathrm{met}} + Q \tag{5.1}$$

where the left-side of the equation is the time-dependent term, while the first, second, third and fourth term of the right side are heat conduction, heat dissipation by blood flow and metabolic heat source (Q_{met}), and external heat source (Q_{laser}). Also, C is the heat capacity of tissue (J/kg/K), ρ is the tissue density (kg/m^3), k is the thermal conductivity of tissue (W/m/K), ρ_{b} is the density of blood (kg/m^3), T is the tissue temperature (K), T_{b} is the temperature of blood (K), C_{b} is the specific heat capacity of blood (J/kg/K), w_{b} is the blood perfusion rate (1/s).
The equation is simplified by considering an ideal tissue system with some approximations: the tissue is considered homogeneous and isotropic; large vessels are not considered; capillaries are considered isotropic; the blood temperature is the same as the temperature within the arteries that vascularize the tissue.

For our applications, the term blood perfusion and metabolic heat source have been neglected. In this way, we obtain the partial differential Fourier equation for homogeneous media:

$$\rho C \frac{\partial T}{\partial t} = k\nabla^2 T + Q \tag{5.2}$$

In a stationary problem, Eq. 5.2 can be simplified into the Poisson equation:

$$k\nabla^2 T + Q = 0 \tag{5.3}$$

If there is not heat generation inside the body, Eq. 5.2 can be simplified into the diffusion equation

$$\frac{\partial T}{\partial t} = \alpha\nabla^2 T \tag{5.4}$$

where

$$\alpha = \frac{k}{\rho C} \tag{5.5}$$

is the thermal diffusivity (m^2/s).

5.3 The Green's function for heat equation

Separation of variables is an excellent tool for solving partial differential equation problems without sources. In the presence of sources, as in the problems discussed in this thesis, the Green's function method can be used. Green's function method is a useful mathematical tool, based on integrals, to deal with initial boundary partial differential equations, and it has been widely applied to solve heat conduction problems. Mathematically, it is the kernel of an integral operator that represents the inverse of a differential operator; physically, it is the response of a system when a unit point source is applied to the system.
Differential equations, such as the heat equation, are all in the form of :

$$Ly(t) = f(t) \tag{5.6}$$

where L is a linear differential operator.Linearity is an important property because it allows superposition of effects and allows equations in general to be solved by the particular integral and complementary function methods.
In this section we focus on a technique for finding the solution to partial differential problems, considering a very simple form for the right-hand side of the equation: an impulse, in which the source term is concentrated at a particular instant of time. The impulse response function is also called Green's function, named after George Green who invented it in 1828.
The moment at which the impulse occurred is $\tilde{t}$, so the force applied is a delta function centered at that moment, and Green's function solves:

$$LG(t-\tilde{t}) = \delta(t-\tilde{t}) \tag{5.7}$$

A Green's function, indicated as G, is the impulse response of a linear differential operator, L, applied on a domain with defined initial and boundary conditions.
In this way, the general right-term of the partial differential equation can be thought of as a superposition of pulses. In fact, the sifting property of Dirac's delta function shows that summing a set of pulses, centered on different values of $\tilde{t}$, on the right term of the equation yields f(t):

$$L\int G(t-\tilde{t})f(\tilde{t})d\tilde{t} = \int \delta(t-\tilde{t})f(\tilde{t})d\tilde{t} = f(t) \tag{5.8}$$

So, the general solution is a superposition of different Green's functions:

$$y(t) = \int G(t-\tilde{t})f(\tilde{t})d\tilde{t} \tag{5.9}$$

Green's functions defines the propagation in time, t, of the effect of applying a source $f(\tilde{t})$ at time $\tilde{t}$.

Now, an impulsive source in space and in time is introduced:

$$q(\tilde{x},t) = \delta(t)\delta^3(\tilde{x}) \tag{5.10}$$

According to the heat equation, the differential operator L is:

$$\frac{\partial}{\partial t} - \alpha\nabla^2_{3\mathrm{D}} \tag{5.11}$$

The heat equation with source term is:

$$\frac{\partial G}{\partial t} = k\nabla^2 G + \delta(t)\delta^3(\tilde{x}) \tag{5.12}$$

The function $G(r, t) = T(r, t)$ defines the temperature value in each point of the medium with respect to time, as a result of the application of the heat pulse to the system :

$$G(r,t) = \frac{1}{(4\pi kt)^{3/2}}\exp\left(-\frac{r^2}{4kt}\right) \tag{5.13}$$

Considering a heat source with a certain temporal duration:

$$\delta(t) = \begin{cases} Q & t \in [0,\tilde{t}] \\ 0 & elsewhere \end{cases}$$

The temperature distribution, as a function of time and space, in the domain of interest, due to the previous source, is obtained by equation:

$$T(r,t) = \int_0^t \delta(t')G(r,t-t')dt' \tag{5.14}$$

The response *T'(r, t)* of the system to a source function *x(r, t)* different from the Dirac's delta function can be evaluated by convolution of the new input signal with the impulse response *G(r, t)*:

$$T'(r,t) = x(r,t) \circledast G(r,t) \tag{5.15}$$

Chapter 6

Thermal Properties reconstruction

In the treatment of ocular diseases, laser is a promising key technique that can induce localized thermal damage in the target area. The ability to predict tissue behavior during laser treatment is important to meet the increasing demand for reproducibility and accuracy in laser procedures. Therefore, it is necessary to provide a decision strategy and predictive model to plan patient-specific laser therapy.
Several variables influence the temperature distribution in the tissue and the resulting effectiveness of the therapy; some variables are closely related to the heat source, while others depend on the specific characteristics of the control target volume.In the first case, some main factors are the power of the laser light, the wavelength of beam emission, and the duration of the treatment. In the second case, it is essential to know the factors related to the biological, optical and thermal characteristics associated with the specific patient. This study focuses specifically on the analysis of the thermal properties of biological tissue as a key aspect to evaluate a predictive model of the thermal response of the target area to laser technology therapy processes. In this way, the model will be able to define a therapeutic protocol associated to the patient, avoiding thermal damage from laser application in the medical field.

Thermal properties are associated with a material-dependent response, e.g. a temperature increase, when heat source is supplied. In particular, thermal conductivity refers to the intrinsic ability of a medium to transfer heat, and the specific heat capacity is the ability of storage of heat in a specific point of a material. Knowledge of the thermal properties of tissues is necessary to predict the outcome of laser-tissue interaction, but reliable estimates of these values are extremely difficult to obtain. Thermal properties are highly temperature-dependent and can vary both spatially within the tissue and temporally due to changes in aspects such as water concentration. Indeed, the differences are due to the biological variability of living things: the physical parameters of the same organ vary from individual to individual and even within the organ itself. In addition, thermal conductivity and heat capacity depend on the state of the tissue, such as in vivo or in vitro; for example, the effective heat capacities of tissues in vivoare up to three times higher than those of tissues in vitro. In vitro measurements usually refer only to steady-state thermal conductivity, while in vivo investigations provide "effective" and thus higher thermal conductivity, taking into account the increased heat transfer through the perfused tissue.
The following Tab. 6.1 shows a short list of some representative thermal properties collected from the literature to provide the reader with some guidance.

Table 6.1: Thermal conductivity of some human organs [32]

Thermal Conductivity, (W/m/°C)	Average	Standard Deviation
Kidney	0.53	0.02
Fat	0.21	0.02
Liver	0.52	0.03
Lung	0.39	0.09
Brain	0.51	0.02
Blood	0.52	0.03
Eye (Choroid)	0.52	0.03
Eye (Cornea)	0.54	0.06
Eye (Lens)	0.43	0.06
Eye (Retina)	0.39	0.09
Eye (Ciliary Body)	0.49	0.04

Relatively large differences in thermal conductivity exist between similar tissues and organs, and differing values for the same organ are frequently reported. The values found in the literature are often only mentioned; therefore, there is no information about the method of measurement, tissue preparation, and tissue status. Most references do not provide an estimate of the measurement uncertainty due to the equipment, nor the standard deviations of the measurements. Therefore, it is difficult to assess the quality of the reported values. In this context, such differences emphasize the importance of both defining the measurement conditions and establishing a reliable measurement technique.

Thermal conductivity and heat capacity are measured using either steady state techniques or transient techniques. This section presents an introduction to the steady-state method, the thermal pulse decay method and the differential scanning calorimetry method.
The steady state techniques that employ steady state measurement of thermal conductivity utilize Fourier's law of heat conduction:

$$\vec{\Phi} = -k\nabla T \tag{6.1}$$

with $\vec{\Phi}$ is the heat flux and ∇T is the temperature gradient. Therefore, the previous equation show that the steady-state methods are based on proportionality between heat flux and an applied temperature difference. The main requirement in detecting heat conductivity is that the total power involved in the treatment creates the time independent monitored temperature profile. So, accurate measurements require perfect thermal insulation, minimizing parasitic heat losses to the environment, especially for samples with small thermal conductance values. Furthermore, no convection should interfere with heat conduction; a demand which seems hardly to be fulfilled in liquid materials. Another challenge of steady-state methods is the accurate measurement of the imposed temperature difference. Typical temperature sensors are thermocouples and resistance temperature detectors (RTDs). RTDs are more complicated to attach to the sample and can have higher parasitic heat losses. In practice, achieving high accuracies is challenging and requires rather complex experimental setups due to temperature sensor uncertainties.In conclusion, steady-state methods have the advantage of measuring thermal conductivity directly based on the simple steady-state heat flux equation, e.g., Fourier's law, but they require accurate knowledge of absolute temperatures and power inputs, and only in vitro analysis is possible.

The differential scanning calorimetry (DSC) is a fundamental tool in thermodynamic analysis, allowing for the investigation of thermal properties of materials, including the measure of specific heat capacity of tissues. DSC instruments typically consist on a single or a double furnace, two crucibles (one containing the bio-material under evaluation, whereas the other one

is left empty as a reference), and thermocouple sensors for temperature monitoring. In heat-flux DSC method, a thermo-electric disk is utilized to transfer the heat to the specimen-containing and the reference crucibles. The differential temperature between the sample under test and the reference, and the heat flux of the specimen q are characterized by a direct proportionality relationship according to the thermal equivalent Ohm's law:

$$q = \Delta T / R \tag{6.2}$$

in which R is the thermo-electric disk resistance. The different temperatures of the reference and the specimen under analysis are ascribable to the heat capacity of the sample material. Calorimetric investigations enable results to be obtained in a relatively short time. In DSC, only small samples, a few mg, are needed to determine heat capacity. However, only in vitro measurements can be made, and care must be taken that no water loss occurs in the tissue before and during the measurement.
Since heat transfer is affected by many parameters (blood perfusion, temperature, composition and inhomogeneities of the tissue) in vivo measurements are necessary. In the thesis is presented a method aimed at reconstructing thermal properties, based on the temperature distribution response of the target zone, following the application of a short pulse of energy emitted by a probe inserted into the tissue.

Heat Pulse Method

The heat pulse method is a transient method for determining the thermal properties of biological tissues under clinical conditions.
The advent of the HP method can be traced back to Schleiermacher (1888), who proposed this method for measuring heat in gases. Then, has been used for a wide range of materials such as gases, liquids, and biological tissues[33]. For this thesis, we focus only on the application of the HP Method in studies of biological tissues at atmospheric pressure for ambient temperatures between 30 °C and 60 °C.
The heat pulse method relies on a heat source and a temperature sensing device. The heat energy is delivered for a short period of time within the tissue of interest, causing an increase in local temperature. The sensor measures

the temperature trend during both the heating phase and the cooling phase. Thermal properties are evaluated by fitting the experimentally measured temperature trend with the analytical temperature derived from the solution of the bio-heat equation using Green's function.

6.1 Green's function method

We define a spatially Gaussian heat pulse:

$$q(\tilde{x},t) = Q\ \delta(t)\ \frac{1}{(2\pi\sigma_s^2)}\ \exp\left(-\frac{r^2}{2\sigma_s^2}\right) \tag{6.3}$$

where

- Q is the power of the heat source, W ;
- $\delta(t)$ is delta di Dirac;
- σ_s is the spatial width of the Gaussian source, mm;
- r is the distance from the source,mm.

As seen in 3.15, the response *T(r, t)* of the system to a source function *q(r, t)* different from the Dirac's delta function can be evaluated by solving:

$$T(r,t) = Q\ \frac{1}{(2\pi\sigma_{\mathrm{s}}^2)}\ \exp\left(-\frac{r^2}{2\sigma_{\mathrm{s}}^2}\right) \circledast\ \frac{1}{(2\pi\sigma_{\mathrm{t}}^2)}\ \exp\left(-\frac{r^2}{2\sigma_{\mathrm{t}}^2}\right) \tag{6.4}$$

where $\sigma_{\mathrm{s}}^2 = 2\alpha\ t_{\mathrm{s}}$ and $\sigma_{\mathrm{t}} = 2\alpha\ t$.

Considering that the convolution product between two Gaussians with variance σ_{s}^2 and σ_{t}^2 is equal to a Gaussian with variance $\sigma_{\mathrm{s}}^2 + \sigma_{\mathrm{t}}^2$, we get *T(r, t)* for $t >= 0$:

$$T(r,t) = \frac{Q}{\{4\pi\alpha(t+t_{\mathrm{s}})\}^{3/2}}\ \exp\left(-\frac{r^2}{4\alpha(t+t_{\mathrm{s}})}\right) \tag{6.5}$$

During the heating phase, the source emits constant power for $t \in [0,\tilde{t}]$, so the temperature distribution can be obtained as:

$$T(r,t) = Q \int_0^{min[t,\tilde{t}]} \frac{1}{\{4\pi\alpha(t-\tilde{t}+t_s)\}^{3/2}} \exp\left(-\frac{r^2}{4\alpha(t-\tilde{t}+t_s)}\right) d\tilde{t} \quad (6.6)$$

In order to solve Eq. 5.4, the complementary error function was introduced:

$$\mathrm{erfc}(x) = 1 - \mathrm{erf}(x) = \frac{2}{\sqrt{\pi}} \int_x^{+\infty} e^{-t^2} dt \quad (6.7)$$

We obtain the temperature distribution during the heating phase, so $t \in [0,\tilde{t}]$:

$$T(r,t) = \frac{Q}{4\pi\alpha r}\left\{\mathrm{erfc}\left[\left(\frac{r^2}{4\alpha(t+t_s)}\right)^{1/2}\right] - \mathrm{erfc}\left[\left(\frac{r^2}{4\alpha(t_s)}\right)^{1/2}\right]\right\} \quad (6.8)$$

The temperature distribution during the cooling phase, so t >= $\tilde{t}$:

$$T(r,t) = \frac{Q}{4\pi\alpha r}\left\{\mathrm{erfc}\left[\left(\frac{r^2}{4\alpha(t+t_s)}\right)^{1/2}\right] - \mathrm{erfc}\left[\left(\frac{r^2}{4\alpha(t+t_s-\tilde{t})}\right)^{1/2}\right]\right\} \quad (6.9)$$

6.2 Finite Element Method

The description of physical laws for space- and time-dependent problems is usually expressed in terms of partial differential equations (PDEs). For most geometries and problems, an approximation of the equations can be constructed, usually based on different types of discretization. These discretization methods approximate PDEs with numerical model equations, which can be solved by numerical methods. The solution of the numerical model equations is consequently an approximation of the real solution of PDEs. The finite element method (FEM) is used to calculate such approximations. Looking back at the history of FEM, the usefulness of the method was first recognized at the start of the 1940s by Richard Courant, a German-American mathematician. While Courant recognized its application to a range of problems, it took several decades before the approach was applied generally in fields outside of structural mechanics. Indeed, with the increasing application of the method in the numerical solution of continuum problems, it has since been extended and applied to the broad field of Continuum Mechanics. Because of its variety of uses and ductility, FEM emerges as one of the best tools for the study of complex systems, for which laboratory investigations and experiments would involve excessive expense, logistical difficulties and difficulties related to the physical measurement of various quantities. The finite element method is a computational numerical method for solving differential and integral equations that arise in engineering. The finite element method is generally used to simulate thermal treatment, because it is a powerful tool to transform differential equations over a volume to algebraic equation at the points, called nodes. The first step in FEM is to define initial and boundary conditions. Then we multiply both sides of the equation by a test function ϕ and integrate over the domain of interest. The test function ϕ and the solution T are assumed to belong to Hilbert spaces. A Hilbert space is an infinite-dimensional function space with functions of specific properties, such that these functions can be conveniently manipulated in the same way as ordinary vectors in a vector space. Indeed, the finite element method is a systematic way to convert the functions in an infinite dimensional function space to first functions in a finite dimensional function space and then finally ordinary vectors (in a

vector space) that are tractable with numerical methods. The weak formulation of the equation is obtained by requiring that this equality holds for all test functions in Hilbert space. It is called "weak" because it relaxes the requirement that all terms of the PDE must be well-defined at all points, requiring instead only equality in the integral sense. It is possible to show that the weak formulation, together with boundary conditions, is directly related to the solution from the pointwise formulation. Then, the finite element analysis of any problem involves basically four steps:

1. The discretization of the solution region into finite number of subregions or elements. The approximation of the solution depends on the number and size of the finite elements: the finer is the discretization, the better is the accuracy of the solution. However, a finer discretization requires a higher computational cost. With the weak formulation, it is possible to discretize the mathematical model equations to obtain the numerical model equations. First, the discretization implies looking for an approximate solution to the equation in a finite-dimensional subspace to the Hilbert space H so that $T \approx Th$. This implies that the approximate solution is expressed as a linear combination of a set of basis functions ψ_i that belong to the subspace:
2. Derive the governing equations for a particular element. One key advantages of the finite element method is the possibility to select test and basis functions that are supported over a very small geometrical region.
3. The assembly of all elements of the solution region, obtaining a system of equations of the same dimension as the finite-dimensional function space.
4. The resolution of the obtained system of equations.

Simulation with COMSOL Multiphysics

To achieve the objectives of this research, the comprehensive COMSOL Multiphysics package, an excellent FEM solver tool, was used. The COMSOL Multiphysics simulation environment facilitates all stages of the modeling process: geometry definition, physical specification, meshing, resolution,

and post-processing of results. Simulation with Comsol Multiphysics software enables graphical representation of "invisible" phenomena occurring in the real world and allows analysis of the interaction of different physics simultaneously on the same object. It also allows the execution of rapid iterations of non-invasive tests, testing different inputs to the sytem. In the end, simulation modeling allows us to study a wide range of operating conditions, such as worst-case scenarios, the limits of our system, and allows us to probe the conditions of a particular hard-to-access point. All this leads to optimization of the system for our purposes.
This chapter will discuss a numerical model to predict the temperature distribution following thermal heating and see how it evolves over time. For this purpose, the COMSOL Multiphysics® program is used, making use of the BioHeat transfer in Biological tissue package. The main steps performed to build this model are given below and will be discussed in detail in the following sections. The entire implementation process can be summarized as follows:

1. Definition of the 2D - axisymmetric geometry;
2. Setting the thermal parameters of the biological tissue;
3. Definition of initial and boundary conditions of our system;
4. Definition of the thermal heat source;
5. Creation of the mesh for model discretization;
6. Study of thermal evolution: time resolution and results obtained.

6.2.1 Thermal model

A thermal model is a mathematical model used to represent a natural thermal phenomenon. In this thesis, a thermal model was created to validate the analytical method based on Green's function, used to reconstruct the thermal diffusivity of human tissue. The model developed simulates the interaction between an unconfined homogeneous biological medium and a Gaussian heat source placed within it. The response of the system during the heating and cooling phases is then studied.

Geometry

The geometry used for the thermal model is a three-dimensional cylinder. Taking advantage of its symmetry, the cylinder is recreated by rotating a rectangle around an axis, i.e. the axis of symmetry of the cylinder. By reducing the size of the model from 3D to 2D geometry, simulation in COMSOL requires less computation time and memory, allowing easier application of boundary conditions and the creation of a simpler mesh. The simulation is a 2D problem in the rz plane and therefore there are variations in the radial (r) and vertical (z) direction. The symmetry axis of the model is coincident with the z-axis. An important decision step in defining the geometry of the system is the choice of the domain size. The optimal dimension of the rectangle was found to be $l_1 = 8$ mm the smaller side and $l_2 = 16$ mm for the longer side. In fact, for the same total number of discretization elements and computational cost, the definition of a wider domain results in a less fine mesh and consequently an increase in the approximation error. On the other hand, for rectangles of smaller width and height, the simulated solution differs from the analytical one, as the latter was derived considering an unlimited medium, for which the boundary conditions are valid.

Setting thermal parameters

Thermal parameters necessary to carry out a thermal study of the tissue of interest are: thermal conductivity, specific heat and density. Biological tissues have a high water content and often their heat response characteristics are similar to those of water. So, the thermal parameter values set in COMSOL to validate the method based on the Green's function are:

- Thermal conductivity $\lambda = 0.56\,\mathrm{W\,m^{-1}\,K^{-1}}$
- Specific heat c = $4{,}186\,\mathrm{J\,kg^{-1}\,K^{-1}}$
- Mass density $\rho = 997\,\mathrm{kg\,m^{-3}}$

Initial and boundary conditions

To solve a differential equation in space, i.e. the bio-heat equation, it is necessary to impose appropriate boundary and initial conditions. In that case, considering futute biomedical application in vivo tissues, the temperature of the geometric volume boundaries is fixed at 37 °C. The same value is also used as the initial temperature of the model for the simulation.

Mesh creation

COMSOL Multiphysics performs a finite element analysis to study thermal propagation within the biological tissue, and then the entire volume of the system of interest is discretized into sub-elements, creating a mesh. The mesh used for the geometry of a model plays a key role in how the model is solved, as it determines the quality, size, density and number of elements into which the geometry is divided. These factors directly affects the computational time required for the solution, the amount of memory required to compute a problem, the way the solution is interpolated between nodes and its accuracy. The selected mesh, "Extremely Fine," is a compromise between computational cost and accuracy of results, and the shape of the elements is triangular. The mesh element quality is an important aspects to consider when validating a model and it is dimensionless quantity between 0 and 1, where 1 represents a perfectly regular element. In the model, the result average mesh quality is 0.9617 and the minimun element quality is 0.69. Fig. 6.1 shows the geometry with the mesh discretization.
After discretizing the volume with an "Extremely fine" mesh with Comsol,

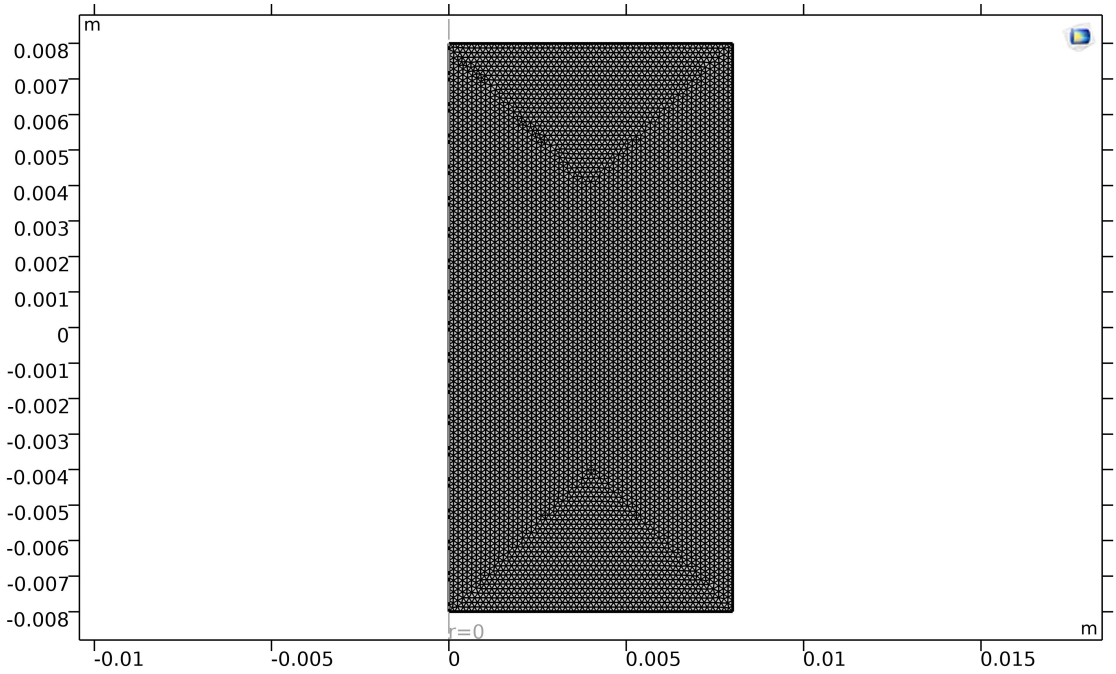

Figure 6.1: Extremely fine mesh with triangular elements.

we study how the thermal mapping evolves over time inside the cylinder, during both heating and cooling phase. To this end, we decide to study the phenomenon over a time duration of 45min.

Definition of the heat source

The source originating the heat distribution within the tissue is a Gaussian heat source, with spatial width $\sigma_s = 1$ mm. The energy source is in the centre of the domain under analysis, with coordinates (r =0,z =0). The power heat source set for the validation test is 1 W constant for a heating phase duration from 2 s to 12 s. The Fig. 6.2 illustrates the Gaussian heat source distribution in space.

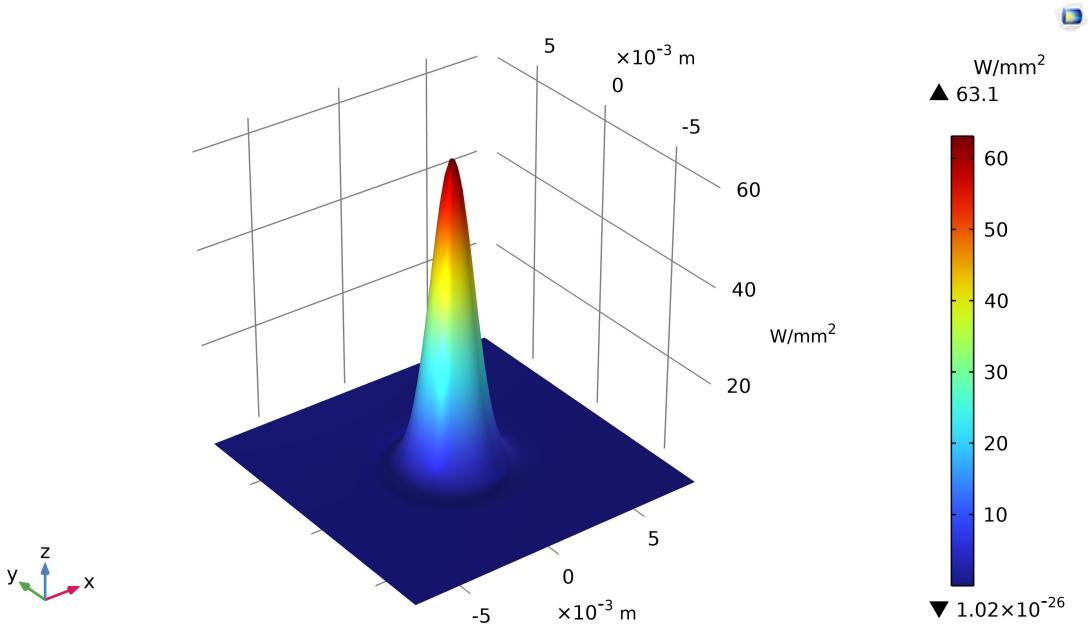

Figure 6.2: Gaussian heat source distribution with at 1/e of 1 mm.

Results

The results quantify the error in the reconstruction of thermal parameters and estimation of thermal response by the model. The system response is evaluated on the rz plane, at the sampling point coordinates: (r=3.7 mm, z=0). Considering the Comsol simulation, the temperature trend is given in input to the model and the thermal properties are reconstructed through the fitting with the analytical bioheat equation solution.

Table 6.2: Error on the reconstruction of tissue thermal parameters

Thermal diffusivity	Conductivity	Heat capacity
2.7^{-11}	1.2^{-4}	0.0818
0.02 %	0.022	0.002

Tab. 6.2 shown above the absolute error and percentage relative error on the reconstruction of tissue thermal parameters.The obtained value of thermal

diffusivity is equal to that expected with a relative percentage error of 0.02%. The following results showing the temperature distribution over time. In the Fig. 6.3, simulated and analytical solutions are compared for each time step. Evaluating the maximum temperature difference between analytical

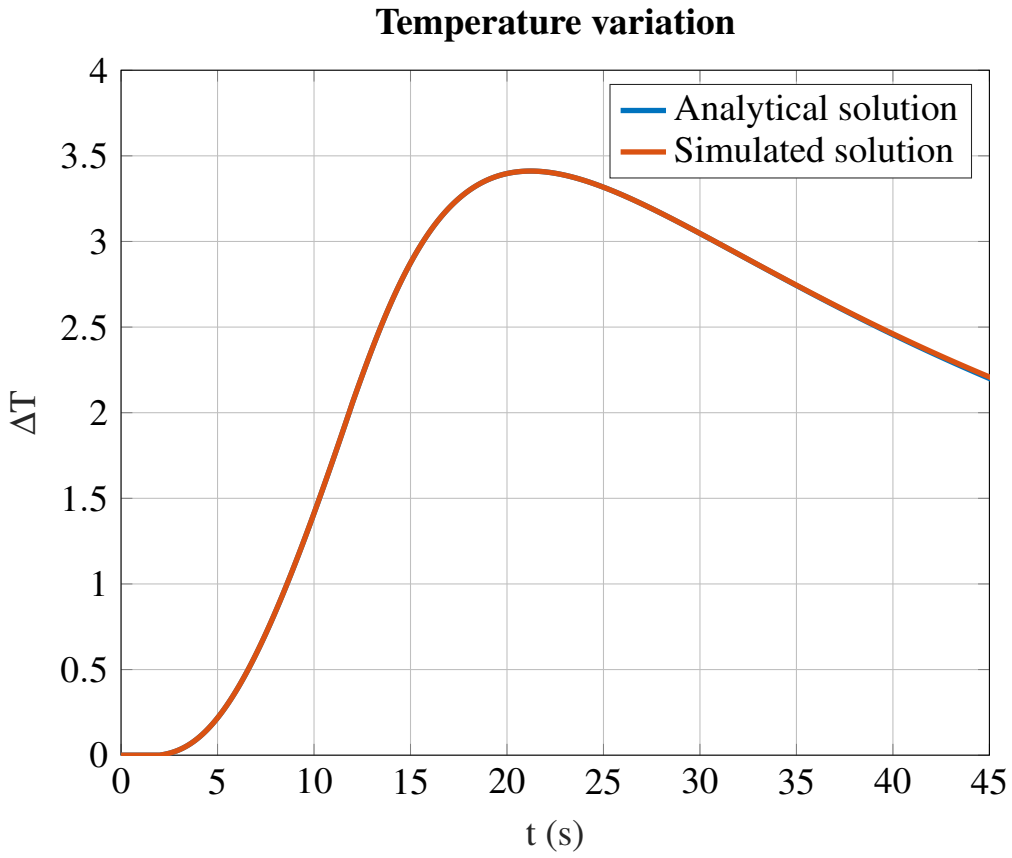

Figure 6.3: Temperature distribution at 3.7 mm from the source centre.

and simulated values, we obtain a local maximum of $\Delta T = +5.6^{-4}$ at 12 s, at the peak temperature value. Due to the boundary limit condition, the absolute error of simulation is $\Delta T = +9^{-3}$, obtained at 45 s simulation. The Fig. 6.4 shows the absolute prediction error of temperature as a function of time, highlighting the effect of the imposed boundary condition on the control system.

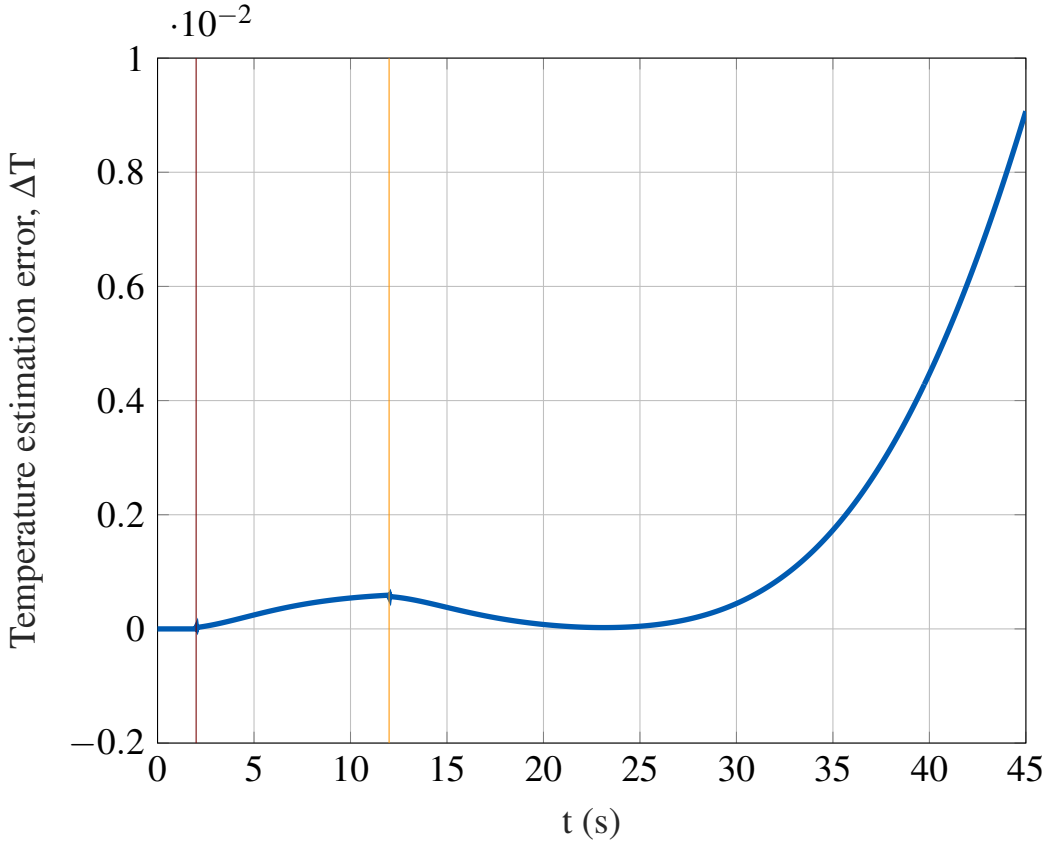

Figure 6.4: Effect of the boundary condition on the temperature estimation. The vertical lines indicate the on/off time of the heating phase.

Observations and conclusion

The solutions proved to be accurate when evaluated at grid points located in an intermediate area between the source and the edges of the domain (Fig. 5.4). Positions closer to the source, Δr <3 mm, are subject to a higher temperature gradient, so they are significantly affected by the discretization errors of the finite element method. In this case, the discrepancy with the analytical solution is mainly due to the simulation accuracy error on the value of the temperature assessment position. To increase the accuracy of the model in Comsol, a finer, higher quality mesh would be required. The points close to the system boundaries, Δr >4.5 mm, present a solution influenced by the boundary condition imposed for the case of unlimited medium. In

conclusion, the choice of temperature sensing point for the evaluation of the analytical method turns out to be between 3 mm and 4 mm, as it guarantees a discrepancy of less than .In this way, the method was validated. The simulation activity part of the thesis is based on two fundamental steps for method optimization: validation and uncertainty analysis. In particular, the previous validation of the heat pulse method allows us to move on to the in-depth discussion in the following chapters. Indeed, the performance of the method is evaluated, quantifying the estimation errors on the thermal behavior of the system under analysis, caused by the possible uncertainties committed during the experimental thermal acquisitions.

Chapter 7

Uncertainty analysis

This chapter is dedicated to the analysis of the uncertainties of the model prediction due to imprecisions of the inputs. To this end, the first step is to define a reference condition, starting from known initial data values and with the temperature evolution obtained from the analytical solution of the bioheat equation. Once the reference thermal response is defined, the uncertainty analysis is performed, and the relative results are evaluated for two main applications: 1. The use of the method as a tool for reconstructing the thermal parameters;
2. The application of the model as a thermal therapy planning tool.
The present study is conducted by intentionally adding an uncertainty to the input value of the model's independent variables in order to simulate the inaccuracies of experimental reality. The main objective of the work described in this chapter is to identify the limitations and weaknesses of the model in view of the correct interpretations of the data provided by experimental tests.

Reference condition

The temperature distribution used to recover the thermal parameters simulating different operating conditions is obtained by analytically solving the bioheat equation, having taken for the thermal properties of the tissue those of water, as listed in the previous model validation section, which result in a thermal diffusivity of 1.341,818 m^2/s.
The heat source considered by the method is a spatially Gaussian source with a spatial width at 1/e equal to 1 mm and a power set to 1 W. The duration of the heating phase is 10 s, from 2 s to 12 s. The simulation lasts up to 40 s, with a resolution in time of 0.1 s. The thermal response of the model is evaluated at points ranging from a distance of 1.5 mm to 8 mm from the center of the source. The curves in Fig.7.1 show the analytical temperature trends at various locations.

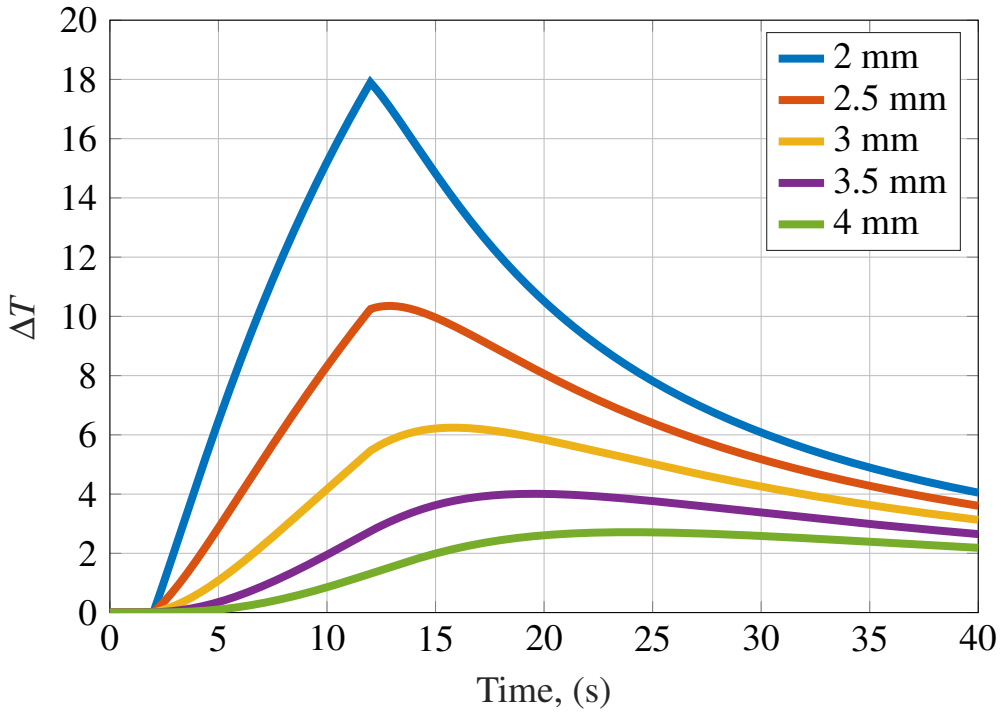

Figure 7.1: Temperature trends at different sampling points.

Ideal case

The first approach to uncertainty analysis is to evaluate the parameter recovery results in the ideal case, in which no perturbations occur. In other words, the first numerical experiment is to validate the approach by reconstructing the thermal parameters, in particular the diffusivity, from the temperature evaluated using the same parameters, without adding any error.
Fig.7.2 shows the value of the recovered diffusivity for each sensing point, compared with the input value indicated by the horizontal line. Since the difference between the known and the reconstructed values is on average an over-estimation of $\Delta k = 3.78e^{-23}$, which is negligible, we can conclude that the implemented fitting approach is able to find the correct value, for all distances from the source.

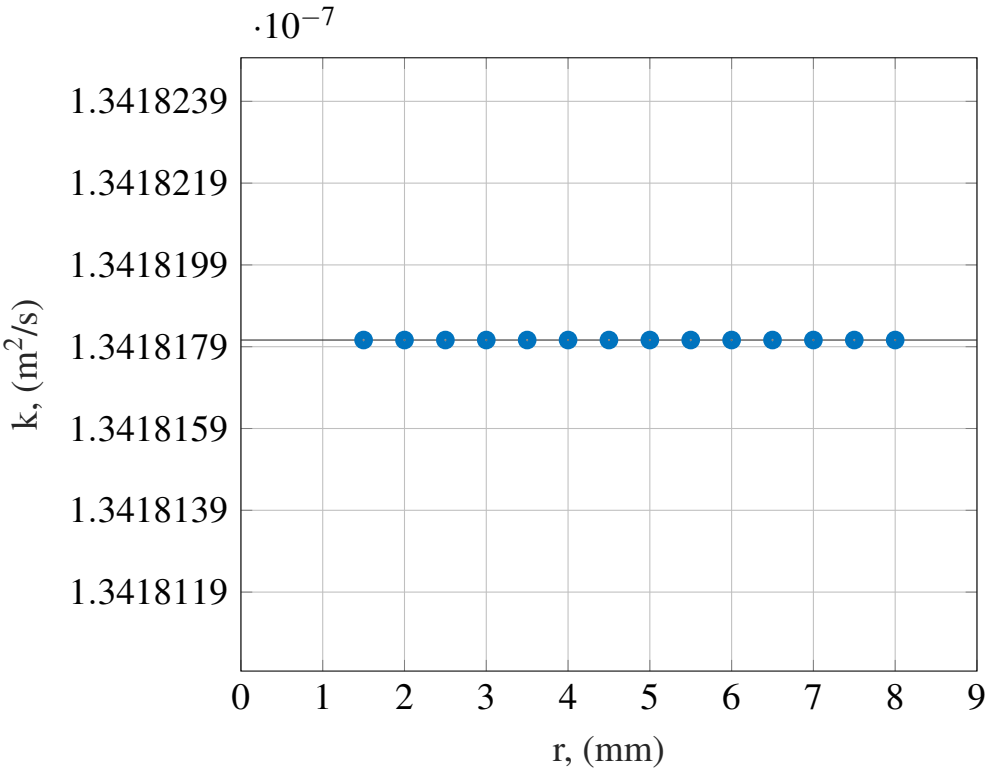

Figure 7.2: Thermal diffusivity reconstruction in the ideal case.

Using the recovered thermal diffusivity values is then possible to recalculate the temperature distributions through the bioheat equation once again. The results, evaluated in percent relative error, are shown in Fig.7.3.

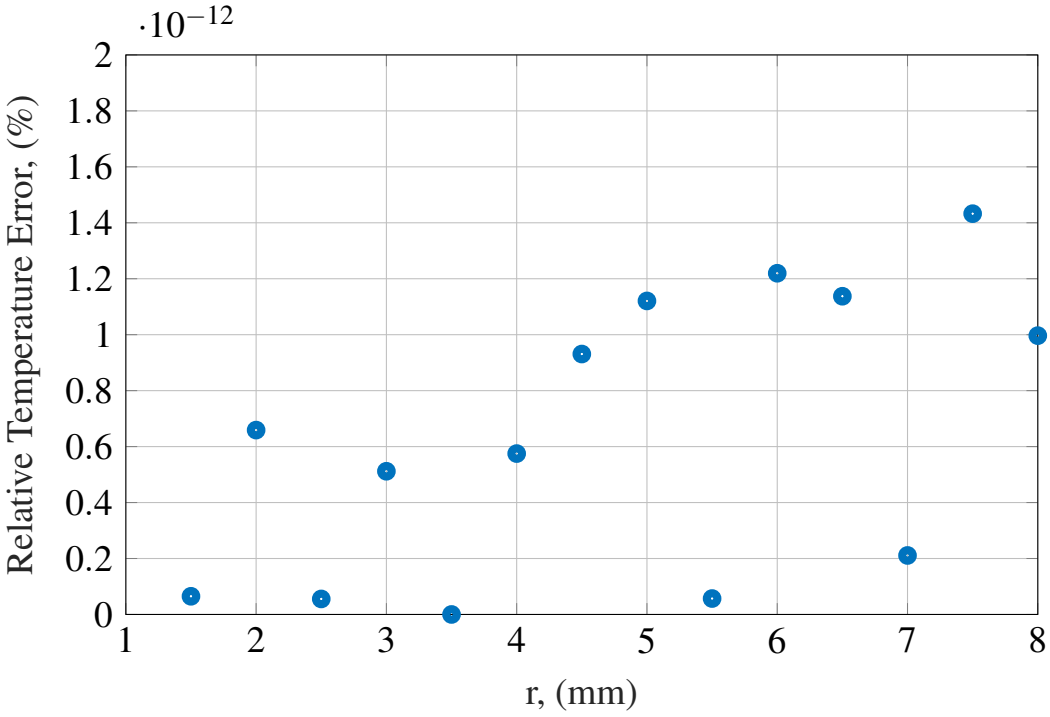

Figure 7.3: Maximum temperature estimation relative error for different distances from the source in the ideal case.

The recovered parameters lead to an average overestimation of the temperature response of approximately $\Delta T = 1.17e^{-15}$, which is negligible.
In the following sections, an analysis is presented on the error of the method in reconstructing the thermal behavior of the target tissue in the presence of:

- Uncertainty due to additive noise;
- Uncertainty on the synchronization between laser and sensors;
- Sensor position uncertainty;
- Uncertainty due to the finite length of the FBG temperature sensor.

7.1 Signal noise

This section presents the analysis of uncertainty due to the additive noise on the signal. The sensors involved in the thesis are all-optical FBG, which are immune to electromagnetic interference that often compromises electronic sensors. Therefore, the main cause of noise is mechanical stresses on the measurement sensor, such as strain effects on the cable during acquisition. In an electrical circuit, the value of an electrical quantity is not stable over time but fluctuates around the expected value. Specifically, the output signal can be decomposed as:

$$x(t) = s(t) + n(t) \tag{7.1}$$

where *x(t)* is the signal acquired by the sensor; *s(t)* is the real signal of interest; *n(t)* is the additive noise.
Signal denoising techniques aim to process the acquired data in order to obtain the real signal with a reduced noise component and the methods involved are based on the application of spectral filters. In this section, we analyze the effect of noise on the performance of the method, computing the error in the reconstructed thermal diffusivity and temperature, as a function of the Signal-to-Noise Ratio SNR, which is an index of recording reliability. SNR is defined differently depending on the type of signal and on the kind of noise. Considering a deterministic signal *s(t)* and a random noise *n(t)* the definition of SNR is :

$$SNR = \frac{A_{\mathrm{s}}}{4\sigma_{\mathrm{n}}} \tag{7.2}$$

where A_{s} is a measure of signal amplitude *s(t)*, the peak value, and $4\sigma_{\mathrm{n}}$ is the amplitude of the noise band (95%).
An important observation is that the magnitude of the acquired temperature variation depends significantly on the power of the heat source. Indeed, too low powers imply temperature variations with amplitudes comparable to additive noise, resulting in unreliable readings.
In the following analysis, noise is modeled as a Gaussian random process with mean equal to 0 and a variance of 1. Sixteen sensing points, from 2 mm to 5 mm, in 0.2 mm steps, are evaluated, and the same noise is added

for each relative distribution. The results are evaluated for three different source powers: 2 W - 3 W - 4 W. The SNR, evaluated in dB, is shown in the Fig.7.4. with respect to the power source value for the locations : 2 mm, 3 mm, 4 mm, and 5 mm.

The graph in Fig. 7.4 shows that for distances from the center of the source

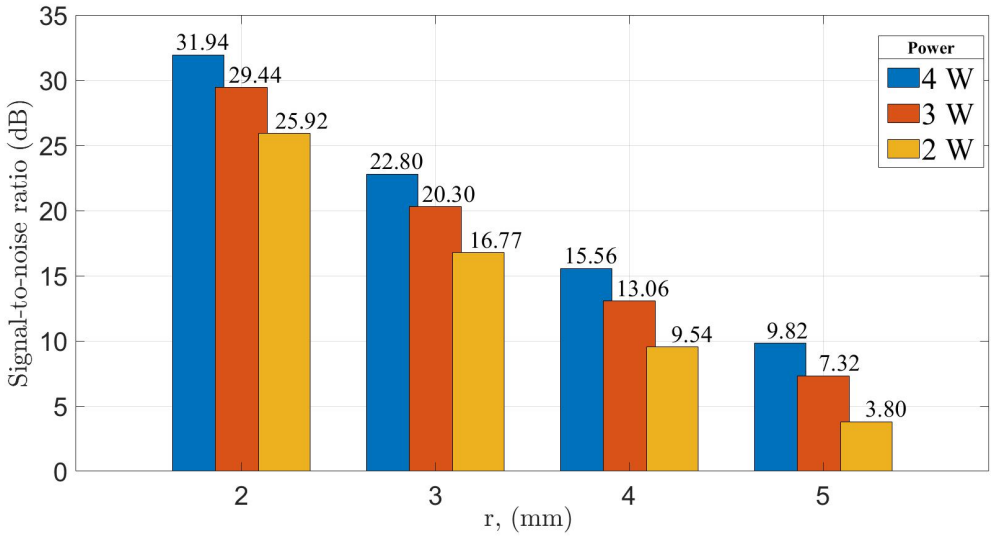

Figure 7.4: Signal-to-noise ratio in decibel for three power sources for different distances from the source.

greater than 4 mm, the additive noise significantly perturbs the signal with a SNR $<$ 10 dB, especially for source powers less than 3 W.

7.1.1 Results

Fig. 7.5 show the analytical temperature trends at the locations 2.4 mm, 3.4 mm, 4.4 mm from the heat source centre, with noise SNR of 22.12 dB, 13.6 dB, and 7.1 dB, respectively. The temperature distributions are obtained through a power of the source of 2 W.

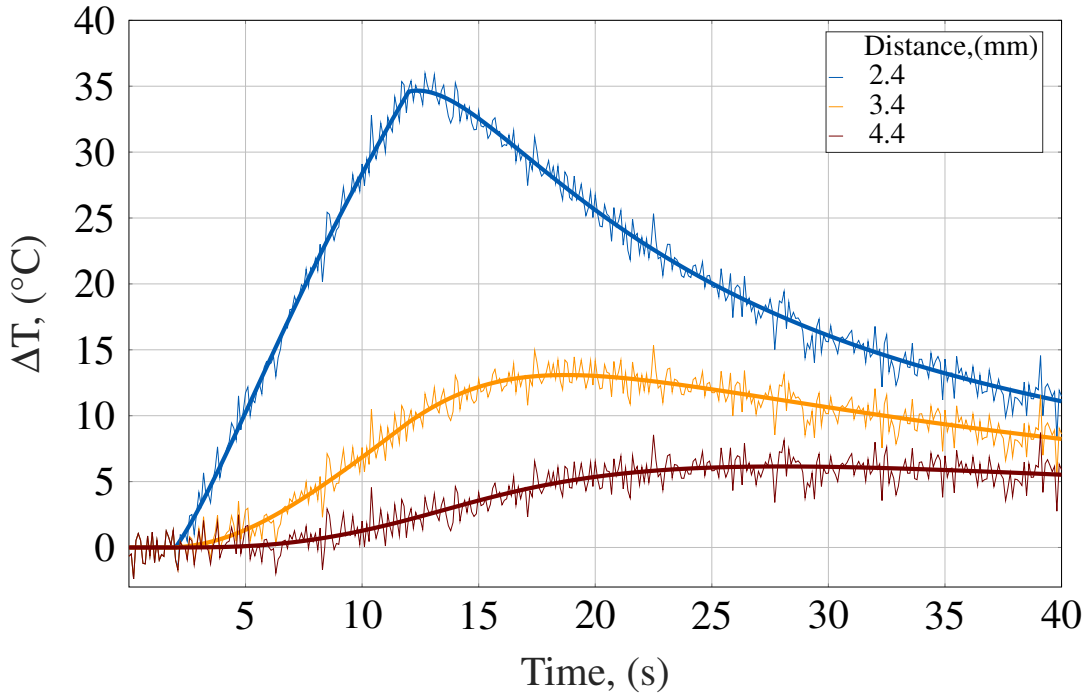

Figure 7.5: Temperature profile at three distances from the source and additive noise with SNR less than 23 dB.

The next graph, in Fig. 7.6, illustrates the effect of noise, superimposed on the signal, resulting on the accuracy of the thermal diffusivity value estimated by the model. Specifically, the relative percent error is analyzed by considering temperature distributions obtained at different positions, with respect to three different heat power values. From the recovered diffusivity values, Fig. 7.7 shows the associated temperature distribution for each sampling point, with respect to power heat source.

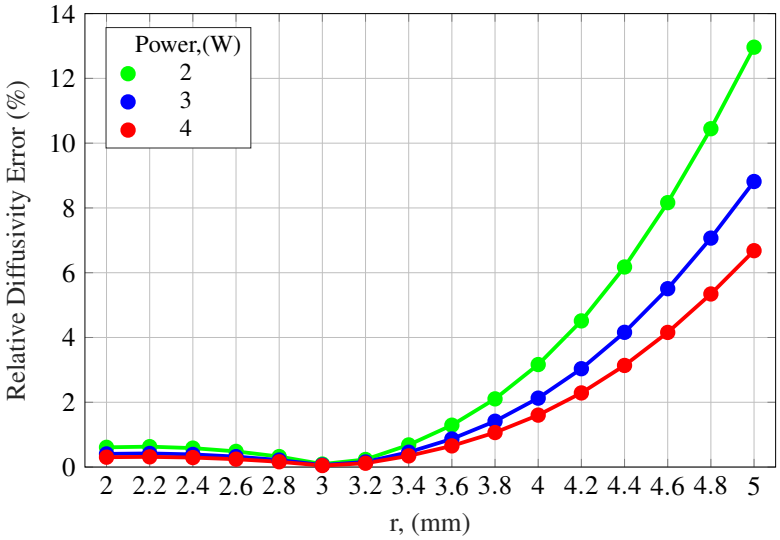

Figure 7.6: Relative thermal diffusivity estimation error at different distances for 2 W, 3 W, 4 W.

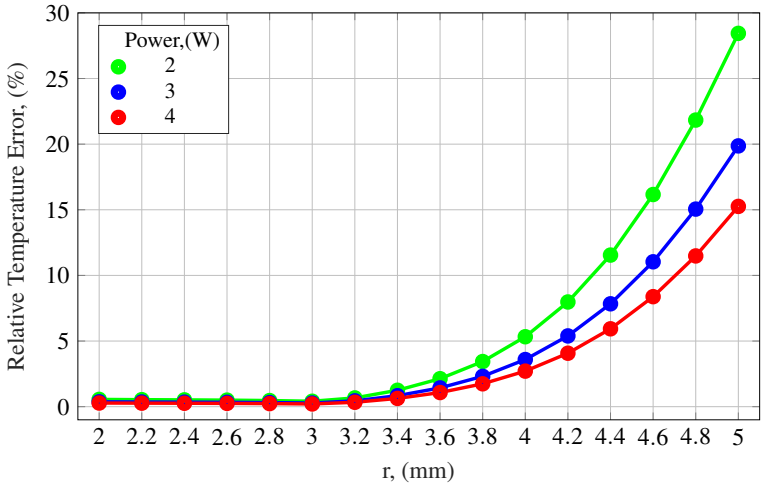

Figure 7.7: Relative temperature error at different distances for 2 W, 3 W, 4 W.

Observations

The effect of noise on the reconstruction of thermal parameters is smaller than that of temperature prediction. The results show that for distances from the source greater than 3.2 mm, the additive noise results in a reduction in the quality of model results on both thermal diffusivity and temperature reconstruction. In addition, high source powers improve the SNR, decreasing the estimation error particularly for more distant points. In the end, the results show a maximum temperature over-estimation error, $\Delta T = 0.3$, for a SNR value of 4 dB.

7.2 Synchronisation error

One of the most influential sources of uncertainty on the thermal parameter reconstruction is the synchronization between the instant of heat source activation and the beginning of the data acquisition. In the laboratory tests a LabVIEW program has been developed to control both the laser source and the MicronOptics FBG sensor interrogator. Since both the laser controller and the FBG interrogator write they outputs in texts files, to simplify their synchronization, a preliminary solution has been implemented adding in both file a time stamp. In this way, during the data post-processing, a time synchronization is manually performed between the acquisition start instant and the heating start instant by aligning their respective data stamps.
The purpose of this section is to evaluate and quantify the effect of the uncertainty of the instant of onset of thermal heating, on the estimation of thermal properties and temperature prediction. In particular, the results of the analysis are important for defining the limits on the temporal resolution required for laser and data acquisition management.
Uncertainty analysis first considers the evaluation of the reference condition by obtaining the temperature trends with a certain value of heating onset instant. These thermal responses are introduced into the model input and an underestimation and overestimation error on the correct instant of heat source activation is introduced. Specifically, the positive and negative time delay are an error in module of Δt : 1 s - 0.8 s - 0.6 s - 0.4 s - 0.2 s. The effect of synchronization uncertainty is evaluated for the following sampling points, distant from the source Δr : 2.5 mm - 2.8 mm - 3.1 mm - 3.4 mm - 3.7 mm - 4 mm - 4.3 mm - 4.6 mm.

7.2.1 Results

The Fig. 7.8 shows the absolute reconstruction error of the thermal diffusivity value for each synchronization error, considering different sampling points.

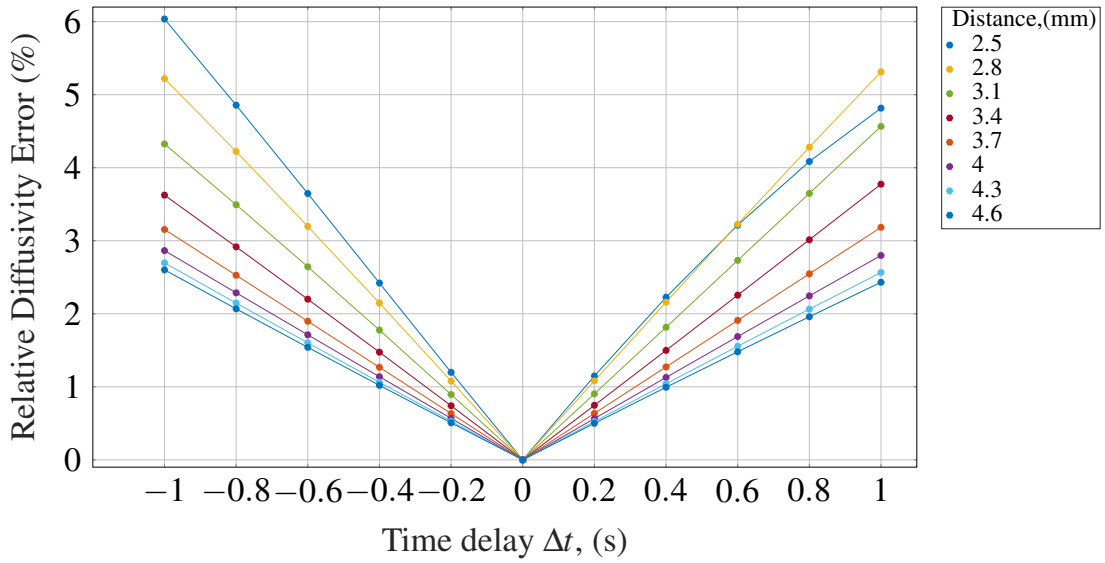

Figure 7.8: Thermal diffusivity estimation relative error due to synchronization uncertainty.

In the above graph, box-plots refer to the estimation errors for different sampling locations, and in each box, the middle sign indicates the median, while the lower and upper edges of the box indicate the 25th and 75th percentiles, respectively. The maximum and minimum values are also represented. Starting from the estimated diffusivity, the temperature distribution has been evaluated again and the effect of synchronization uncertainty is shown in Fig.7.9. At each value on the x-axis, box- plots refer to the estimation errors for different sampling locations, and in each box, the middle sign indicates the median, while the lower and upper edges of the box indicate the 25th and 75th percentiles, respectively. The maximum and minimum values are also represented.

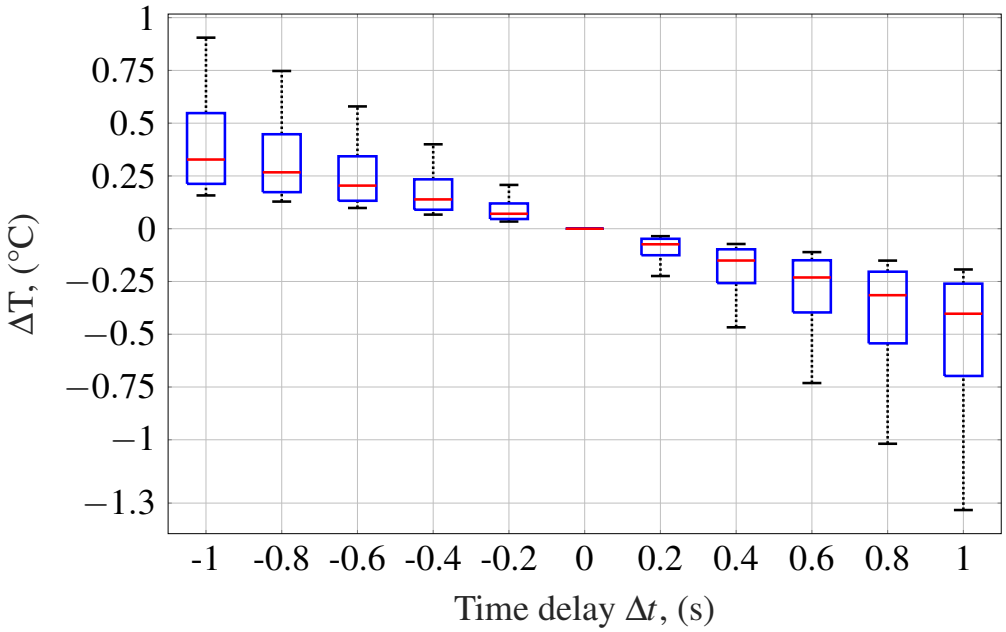

Figure 7.9: Temperature estimation error due to synchronization uncertainty.

Observations

The synchronization uncertainty on temperature estimation results, on average, in an error below the critical threshold of ΔT=0.5 °C. Analyzing the effect of the sampling point position on the model outcomes, the results show that the closest distance from the center of the source, i.e., 2.5 mm, generates a larger estimation error, for all time delay. Moreover, considering distances greater than or equal to 3.4 mm, the temperature reconstruction errors are lower than 0.5 threshold, for all uncertainties evaluated in this section. An important conclusion is that negative time delay about the instant of heat source activation result in underestimation of temperature with a smaller absolute error than in the case of positive uncertainty, where temperature is overestimated with a larger error. As for the reconstruction of thermal parameters, again positive delays and larger sensing distances are favored. In particular, for negative uncertainties, there is an overestimation of diffusivity and vice versa in the opposite case.

7.3 Position error

One of the main steps in the experimental activity is the positioning of the all-fiber sensors with respect to the heat source. The laboratory tests require manual sensor placement by the operator, and future applications of the method in living biological tissues involve the invasive insertion of the fiber within the target volume; this leads to inaccuracies in positioning, also due to possible displacement during the experimental trial. Therefore, the uncertainty analysis is required to evaluate the effect of sensor position errors on the method performances.
In the section, the response of the system at a known distance is obtained through the analytical solution of the bioheat equation. Next, the temperature distribution is given as input to the model with an underestimation or an overestimation of the sensor distance. Manual application of the sensing probe to the target zone allows accuracies on the order of millimeters. Therefore, the analysis considered eight sensing points equally spaced between 2.5 mm and 4.6 mm, and for each of them is introduced the position errors of Δr : ± 0.1 , ± 0.2 , ± 0.3 , ± 0.4 , ± 0.5. The ideal situation is evaluated by considering the case of certain sensor position, Δr=0, to demonstrate the reliability of the method.

7.3.1 Results

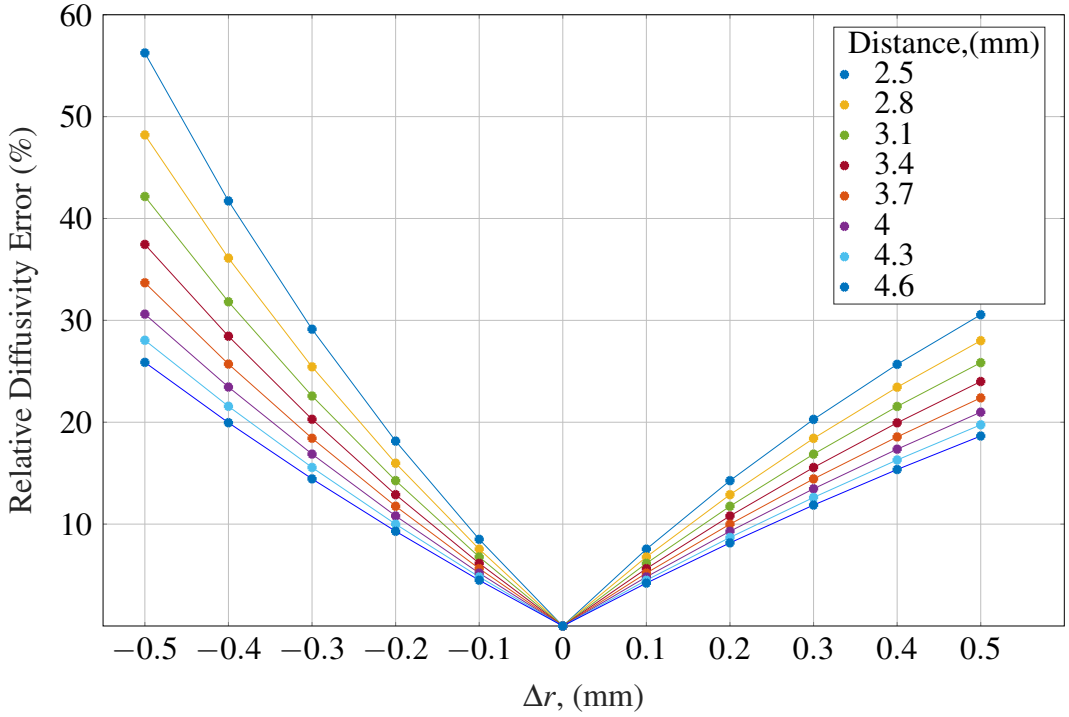

Figure 7.10: Thermal diffusivity estimation relative error due to position uncertainty.

Fig. 7.10 displays the relative percent error on the estimation of the diffusivity parameter, as a function of the placement error committed. From the graph, it can be seen that underestimating the distance of the temperature sampling point significantly increases the error on the thermal parameter recovered. In particular, the point closest to the source obtain the maximum relative error of 56% and the point farthest away obtain the minimum value of 26%. The Fig. 7.11 shows the absolute temperature estimation error.

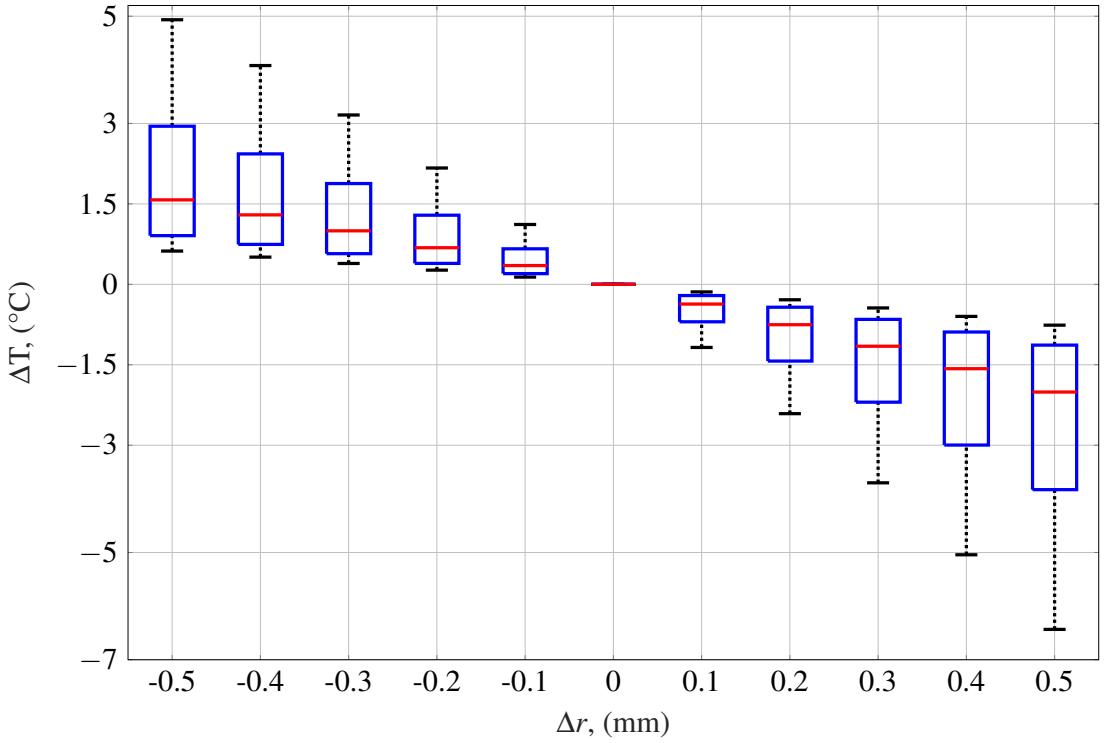

Figure 7.11: Temperature estimation error due to position uncertainty.

Observations

The result of the analysis show that for uncertainties greater than or equal to 0.1 mm, the temperature estimation error exceeds the threshold ΔT=0.5 °C for locations closer to the heat source, from 2.5 mm to 3.3 mm. On the other hand, for larger distances from the source, the errors on the system response estimation are below the threshold, based on the value of position uncertainty. In particular, better temperature estimation is found for more distant points. In conclusion, study shows that the performance of the model depends significantly on the position uncertainty of the sensor. Furthermore, the optimization of the model will strongly depend on the choice of the distance at which sampling the signal of interest.

7.4 Sensor length error

As already discussed, FBGs are used for temperature sensing during the heat treatments. The ideal model considers that the temperature is sampled with a point sensors; however, FBGs have a finite extent so that it is necessary to take into account the temperature variation over the finite spatial length of the Bragg grating. Recent studies [34] have shown that the accuracy of temperature measurement decreases as the size of the sensor increases. In particular, the acquisition system reads the data with an error of about 3 °C for a grating length of 1.5 cm and with an error of about 0.5 °C for a size of 1 mm. Another key aspect to consider is the non-linearity of the temperature distribution, which is an influence quantity on the sensor output. In the case of linear thermal map, the Bragg grating has been shown to return the average temperature along its sensing area. Under a non-linearity condition, it has been shown that the difference between the acquired temperature and the mean temperature is smaller in case of shorter FBGs [34]. Therefore, the optimal solution is to use sensors with sensitive length in the order of few millimetres. Considering the relationship between sensor length and measurement accuracy, in the experimental activity is involved an high density of sensing points through an array made by all-optical fiber Bragg sensors, each with 1 mm of spatial resolution. The two main steps of the present uncertainty analysis are: 1. Analytical reconstruction of the mean temperature acquired by the FBG, the length of which extends from 4 mm to 5 mm from the heat source.The first sensor position, from 4 mm to 5 mm, is defined based on the results of the previous sections,in order to minimizing the influence of uncertainties of input data. 2. The evaluation of cases where the temperature detected by the sensors is associated with points, belonging to the same grating and having different distances from the source. The Fig. 7.12 illustrates the configuration of the experimental set-up described. Thermal parameters are then reconstructed by associating the average tissue response for three different sampling points along the length of the sensor. In particular, the points along the sensor are the closest to the source (4 mm), the furthest (5 mm), and the midpoint of the FBG (4.5 mm). Once the optimal position to associate the acquired data with has been evaluated, the sensor is moved relative to the center of the source. Four different midpoints are

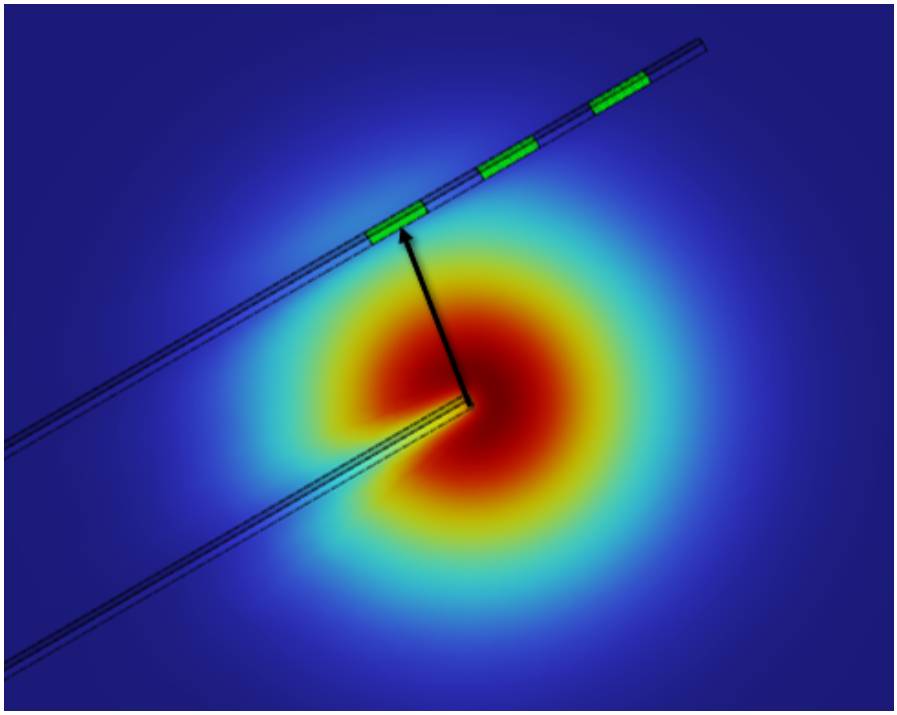

Figure 7.12: Illustration of the laser beam delivery fiber parallel to the fiber with the grating array. The arrow indicates the distance of the central point belonging to the 1-mm-long sensor.

obtained and the values of the thermal parameters are estimated, respectively. Finally, knowing the thermal behavior of the target volume, the estimation error of the heat map as a function of distance is evaluated.

7.4.1 Results

The Fig. 7.13 illustrate the absolute error on temperature estimation for three main positions of the points along the length of FBG. The results show an average of $\Delta T = 0.04$ °C in the mid position case, while the near and far positions have errors greater than 0.5 °C.

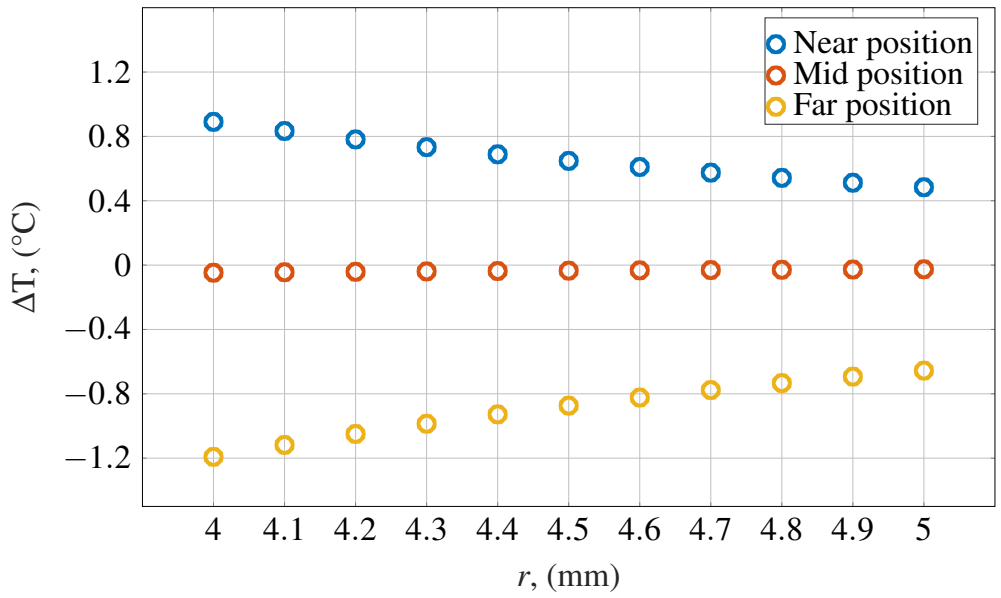

Figure 7.13: Temperature estimation error due to sensor length error.

The Tab.7.1 shows the relative percent error on the estimated thermal diffusivity as a function of the point to which the average temperature is associated. In addition, the column on the left indicates different positions of the sensor midpoint.

Table 7.1: Relative diffusivity error due to sensor length uncertainty.

Thermal diffusivity			
Distance	Near Position	Mid Position	Far Position
2.5 mm	51.04 %	3.33 %	32.87 %
3.5 mm	33.74 %	1.74 %	24.77 %
4.5 mm	25.17 %	1.098 %	19.89 %
5.5 mm	20.07 %	0.76 %	16.61 %

Focusing the study to best-case condition, the performance of the model

is analyzed by considering the central location of the Bragg grating at different distances from the source. A spatial extent of the sensor of 1 mm is always considered, and the following cases are evaluated: (2 mm-3 mm); (3 mm-4 mm); (4 mm-5 mm); (5 mm-6 mm). The Fig.7.14 shows the unsigned errors of temperature estimation, respect to the positions at which the temperature is predicted by the method. For each r, four different thermal properties are given in input to the model, resulting in different heat maps. The parameters are those related to the percentage errors in the second column of Tab.7.1.

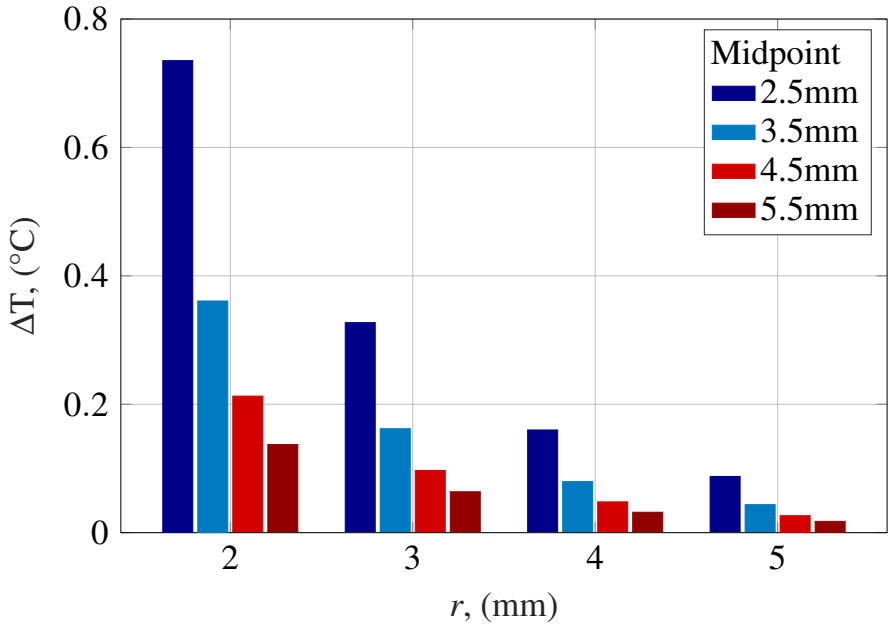

Figure 7.14: Absolute error of temperature estimation for 1mm-wide grating.

Observations

The graphs in Fig. 7.13 and Fig. 7.14 lead to the following conclusions:

- The optimization of the method is based on associating the temperatures,

acquired from the non-point sensors, with the position of their midpoints respect to the center of the heat source. In addition, the correlation of the sampled signal with the positions closest to the source results in an underestimation of the tissue thermal response, with a smaller absolute error than the opposite case;

- Model performance in recovering tissue thermal parameters improves as the distance of the sampling points increases;
- The ability of the method to predict the temperature map is significantly better with percentage errors on diffusivity estimation below 1.5%.

In the end, the ΔT values in Fig.7.12 are always negative, and therefore the model overestimates the temperature peak.

Chapter 8

Fiber Bragg grating array

This chapter aims to eliminate or minimize the uncertainty of sensing point location on the reconstruction of thermal parameters and thermal response of biological tissue. The purpose is achieved by additional information provided by the chosen method of temperature monitoring : fiber-optic Bragg grating arrays. A key aspect to consider is the type of temperature map distribution of the system in response to laser therapy. Indeed, the analytical trends presented in Fig. 7.1 in Chapter 6 show a strong temperature gradient with respect to distance from the source; for example, the peak temperature variation from 2 mm to 3 mm is ΔT = 18 °C, and the the maximum temperature change from 3 mm to 3.5 mm is ΔT = 2 °C. Therefore, for distances close to the center of the source, the sensor position error has a significant impact on the accuracy of the final results of the method; in fact, it was found in the previous chapter that uncertainties of 0.1 mm can result in a temperature estimation error of 1.5 °C. Fig. 8.1 shows the result of analyzing the temperature distribution in the target volume following the application of a Gaussian-type heat source; the plot show iso-potential lines of the thermal response in XY-plane, with gradient arrows. The gradient increases significantly at distances close to the center of the source.

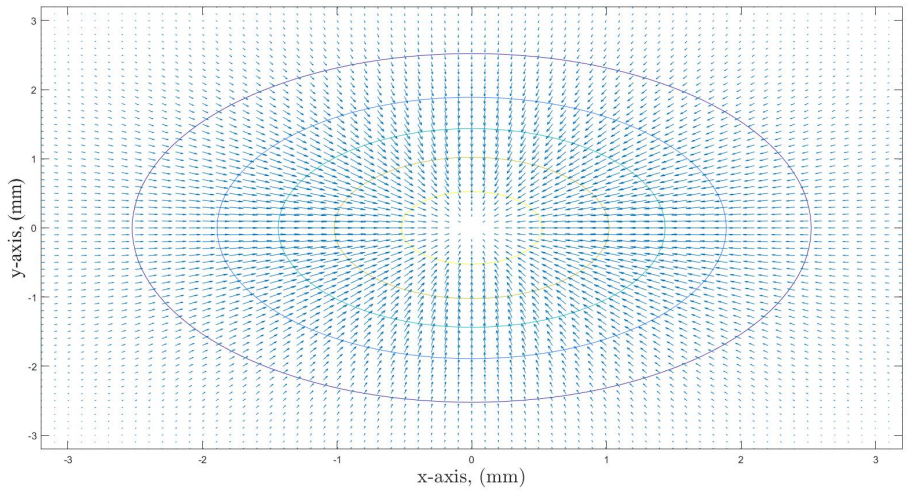

Figure 8.1: Iso-potential line of temperature map for 5 W of power source with $\sigma_s = 1\,\text{mm}$.

In the following sections, we first analyze the advantage of Bragg grating arrays as point sensors at known and well-defined relative distances. Second, the real case of arrays composed of 1-mm-long gratings is evaluated.

8.1 Array of point-type FBG

Uncertainty analysis on position error is performed by considering an acquisition tool of point-sensor array. Specifically, a sequence of three FBG separated by 1 mm along the optical fiber is considered. In this study, the laser beam delivery fiber and the fiber with sensors are considered to be positioned in parallel, at a distance of 1.5 mm. The energy of the laser beam is absorbed by the tissue and is considered a Gaussian heat source at the center of the system in the xy plane. The second fiber present the first sensor at the minimum distance of 1.5 mm, and the other gratings are positioned according to the quantities defined by the Pythagorean theorem. The all distances for monitoring the thermal response of the system are : 1.5 mm, 1.8 mm and 2.5 mm. First, the reference temperatures associated with the

three positions are analytically evaluated and the position uncertainty introduced is $\Delta r = (\pm 0.5\ ,\ \pm 1\ ,\ 0\ ,\ +2)$. The fitting of the analytical solution is performed simultaneously on multiple temperature signals acquired along the sensing fiber. In this way, the position value of the first sensor in the array is reconstructed correctly and, consequently, of the others as well. In addition, a single optimal thermal diffusivity value is derived, with which the thermal responses at different locations are derived and compared with the reference ones.

8.1.1 Results

The Fig. 8.2 shows the thermal diffusivity reconstruction with respect to different location errors from the source centre. The results highlight the method's ability to reconstruct the parameter regardless of the value of the uncertainty.The difference between the known value and the reconstructed value is on average an over-estimation of k of $\Delta k = 3.27e^{-22}$, which is negligible.

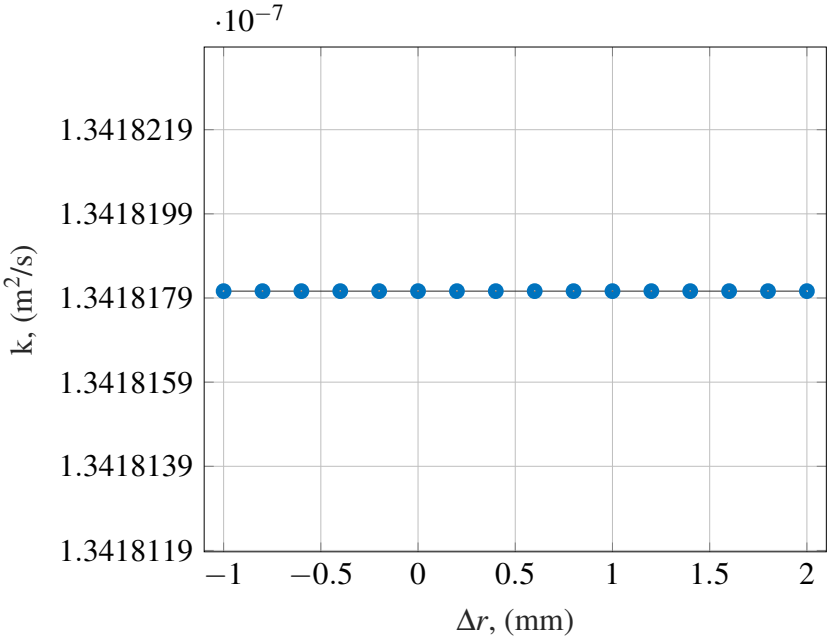

Figure 8.2: Thermal diffusivity recovery values for different position uncertainties.

The Fig. 8.3 show the absolute temperature estimation error for each position variation. The maximum value is $\Delta T = 2e^{-12}$, which is negligible.

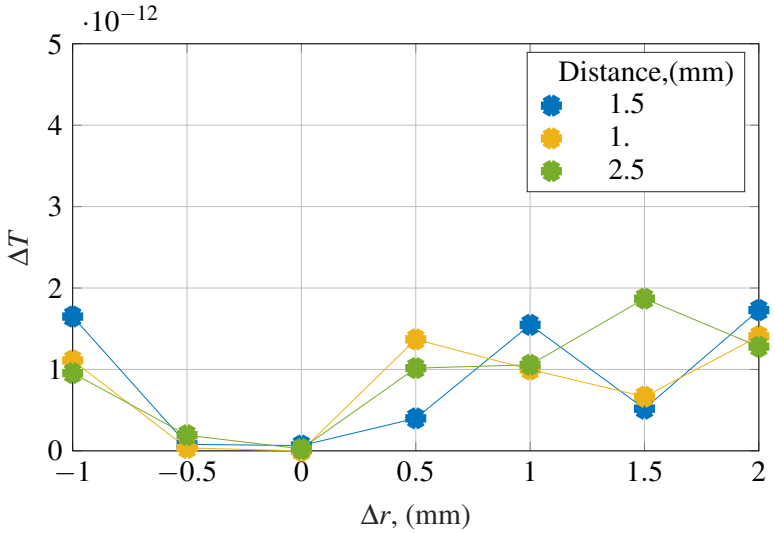

Figure 8.3: Absolute temperature estimation error for different position variation.

8.2 Array of 1-mm long FBG

In this section, the performance of the method is analyzed considering the FBG spatial dimension of 1 mm. So, the effect of sensor placement uncertainty together with that for the finite sensor size is evaluated. Considering the results of Chapter 6, the temperature map read along the grating length is averaged and associated with the center point of the sensor. The same parallel fiber configuration of the previous section is maintained, and the point at distance 1.5 mm coincides with the position of the center of the first sensor with respect to the heat source. the analysis considered five FBGs, with the following midpoints: 1.5 mm - 1.8 mm - 2.5 mm- 3.35 mm-4.3 mm. The analysis first averages the temperature read along the FBG in 0.1 mm steps and associates it with the midpoint of the sensor. Next, an error is introduced on the sensing point locations of $\Delta r = (\pm 0.5\ ,\ \pm 1\ ,\ 0\ ,\ 1.5\ ,\ +2)$. The Fig.8.4 illustrates the parallel arrangement of the delivery laser fiber with the 1-mm long FBG fiber array.

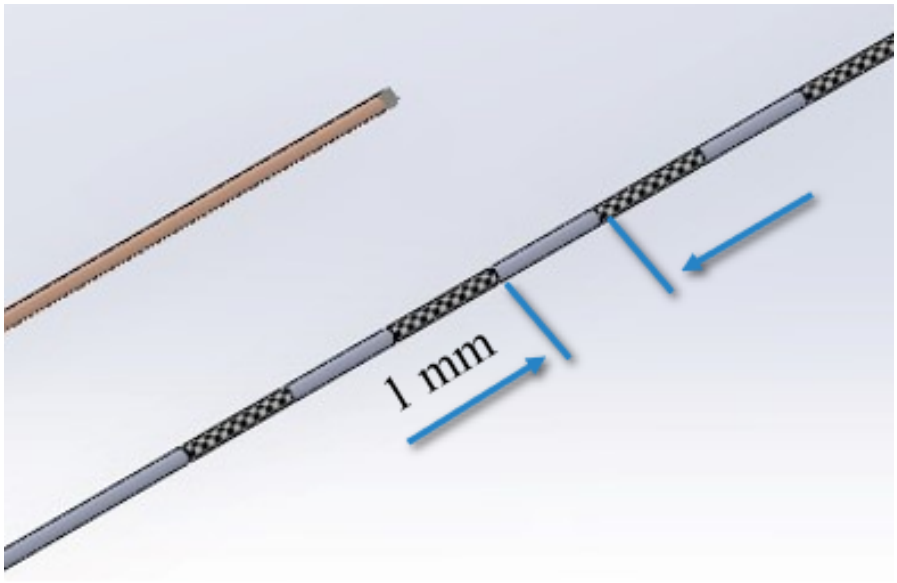

Figure 8.4: Fiber laser delivery and all-optical FBGs array.

8.2.1 Results

The results on thermal parameters estimation show that the difference between the known value and the reconstructed value is an under-estimation of thermal diffusivity of $\Delta k = 7.64e^{-11}$, for each position error. This conclusion shows that the main contribution of error is due to sensor length, as the position uncertainty is canceled out by the method of fitting temperature trends associated with known relative distances. The Fig.8.5 shows that the method overestimates the thermal response of the tissue of interest with a larger error for locations closer to the source origin, regardless of the value of the position uncertainty.

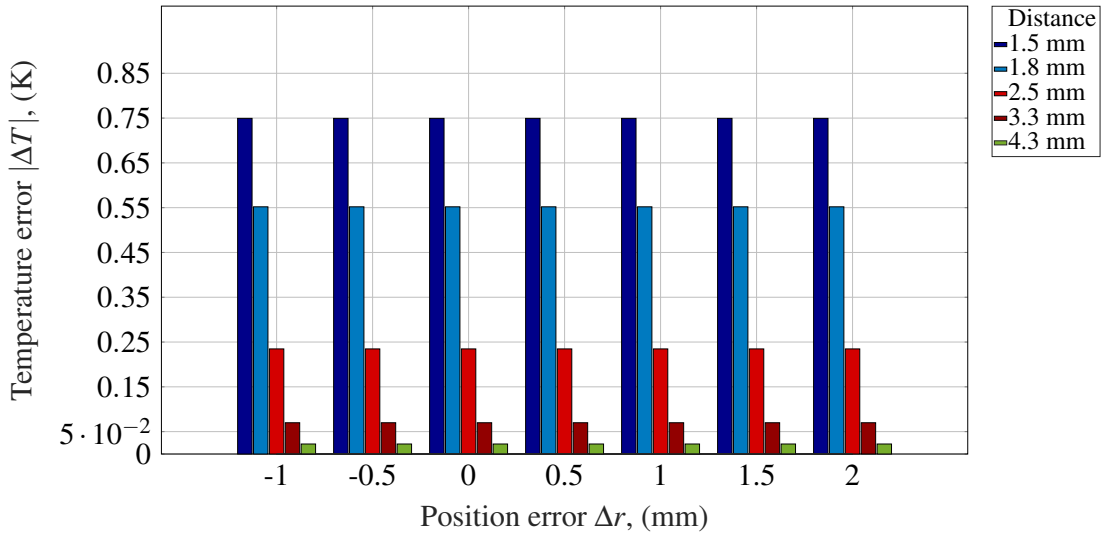

Figure 8.5: Absolute temperature estimation error for different position sensor uncertainty.

Part III

Experimental activities

Chapter 9

Experimental tests on phantoms

The experimental activity is based on the key information obtained in the previous chapters and aims to validate the applicability of the heat pulse method in real-world settings. The chapter presents the results of the tests performed in the laboratory, reporting detailed information on the instrumentation and experimental setup used for the tests.

9.1 Instrumentation

The instrumentation involved in the thermal treatment tests consists of two components: the first includes the generation and delivery of the laser beam; the second involves an instrument for detecting the thermal response of the target area. The laser device is based on a laser diode and, through a USB connection to the PC, is managed by a program in LabVIEW® to set and control the parameters of the laser beam. The program allows the user to set the power (W) of the beam and the emission duration in seconds through a timer. The user interface also includes an Enable on/off button for turning the irradiation on and off.The emission wavelength is 915 nm in a continuous wave modality. The Fig. 9.1 show the user interface in LabVIEW.

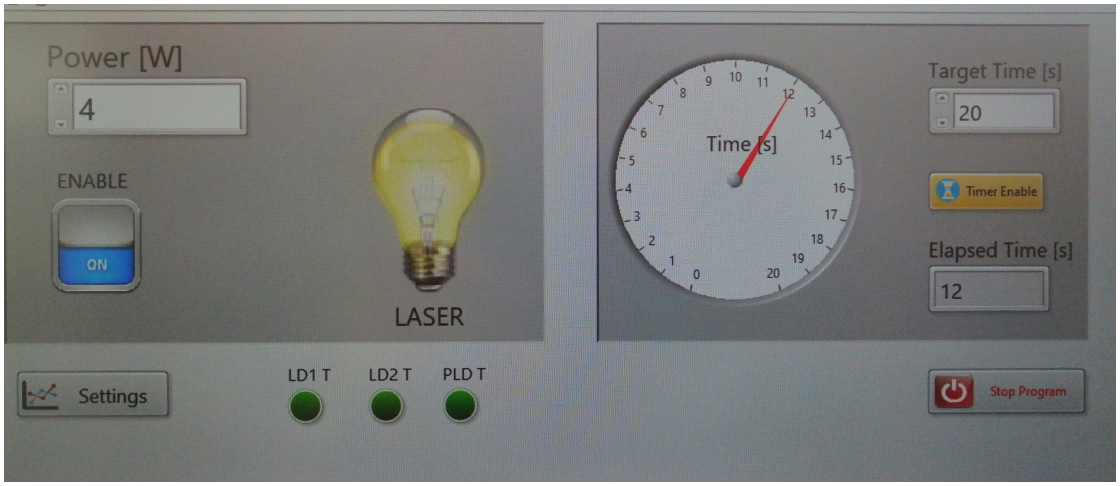

Figure 9.1: LabVIEW user interface for setting laser beam parameters.

The delivery of the laser light is through a multi-mode optical fibre with the following specification:

- Cladding diameter: 125 µm;
- Core diameter: 105 µm;
- Numeric aperture: 0.22;

Laser radiation is guided to the treatment target area through two FTB250MN Spider Fan-Out multimode fiber tubes arranged in sequence with an E-2000 optical connector, and terminating with the tip of the multimode optical fiber.
The experimental activity involved the multi-point fiber optic sensors to minimize the invasive impact and to reduce artifacts during the recording of the temperature increase distribution around the exposed area. In particular, the sensing system is based on all-optical fiber array of FBG for acquisitions distributed in the target area. The temperature sensing tool is a single-mode fiber with high-density 20 FBG array. Taking into account the results from the uncertainty analysis in Chapter 9, the texts involved 1 mm-wide gratings with a relative distance of 1 mm. The single-mode optical fiber has a core diameter of 9 µm and a cladding diameter of 125 µm, and the Bragg

wavelength range is from 1,505 nm to 1,581 nm. The FBG interrogator is MicronOptics HYPERION si155, which allows acquisition with four optical sensing fibers simultaneously for experimental tests. A LabVIEW program handles communication and data transmission with the FBG interrogation device.

9.1.1 Data processing

The Bragg wavelength peaks acquired by Micron Optics for each channel are saved in a texts file. The document also contains the corresponding temperature values, according to the relation:

$$\Delta T = \frac{\lambda_B - \lambda_0}{K_0} \tag{9.1}$$

where λ_0 is the initial value of Bragg wavelength acquired by the optical interrogator at the beginning of the test. The temperature sensitivity coefficient K_T is obtained by a specific calibration file required by the the LabVIEW program before starting the data acquisition.

9.1.2 Phantom

Experimental tests involve the preparation of a phantom of homogeneous material in order to make repeatable and reproducible measurements in time. The phantom is made with a water and vegetable agar, and a few drops of China ink to increase the absorption of the laser beam. Agar is a jelly-like bio-polymer synthesized by many red seaweeds as their major cell wall component [35]. In experimental activity, agar acts as a thickener for a gelatinous water simulator of the behavior of a biological tissue. In fact, water is the main constituent of human tissues and this has significant effects on thermal properties. The reference properties of the phantom are :

- Thermal conductivity $\lambda = 0.56\,\mathrm{W\,m^{-1}\,K^{-1}}$
- Specific heat c = 4,186 $\mathrm{J\,kg^{-1}\,K^{-1}}$
- Mass density $\rho = 997\,\mathrm{kg\,m^{-3}}$

In particular, the components for phantom preparation are:

- 300 g of water;
- 15 g agar agar (5% of water);
- 10 g drops of ink.

The shape of the control volume is a prism with a circular base: the thickness is 3.5 mm and the diameter is 9 mm, to simulate an infinite medium. In fact, the importance of the effect of the boundary conditions imposed in the target volume on the reconstruction of the thermal parameters of the method is emphasized in the previous chapters. Two phantoms are prepared so that the probe, consisting of the delivery fiber and the sensing fiber, can be placed in the center of the control volume. The Fig. 9.2 show the the system under analysis.

Figure 9.2: Biological tissue simulator diameter and thickness.

Probe position and laser parameters

The probe is placed on the upper surface of the lower phantom, and thus is located at mid-height of the system, at the interface between the two agar volumes.The position of the tip of the delivery fiber is at the center of the surface. The delivery and sensing fibers are placed in parallel, at a distance of about 2.5 mm. The Fig. 9.3 indicate the type of arrangement of the fibers.

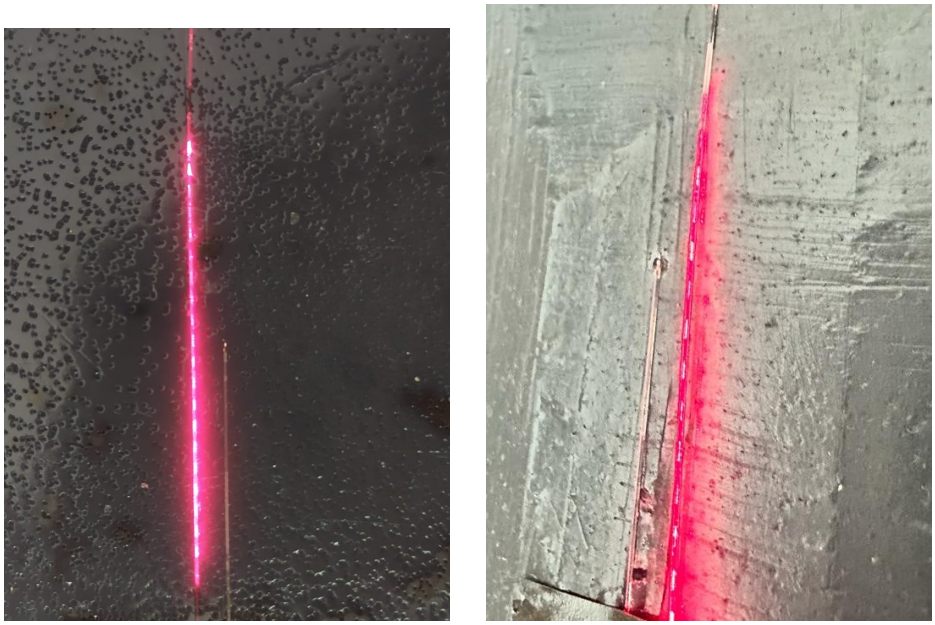

Figure 9.3: Fiber laser delivery parallel to the fiber with FBGs.

Experimental tests are conducted with powers of 3 W and a treatment duration is 20 s, in order to ensure a significant temperature change.

9.1.3 Results

The results obtained from the all-optical FBG are shown in Fig. 9.4. In particular, the analysis focused on four lattices in the array (17,16,15,14), which show a significant variation in temperature. The an The time resolution is about 2 ms.

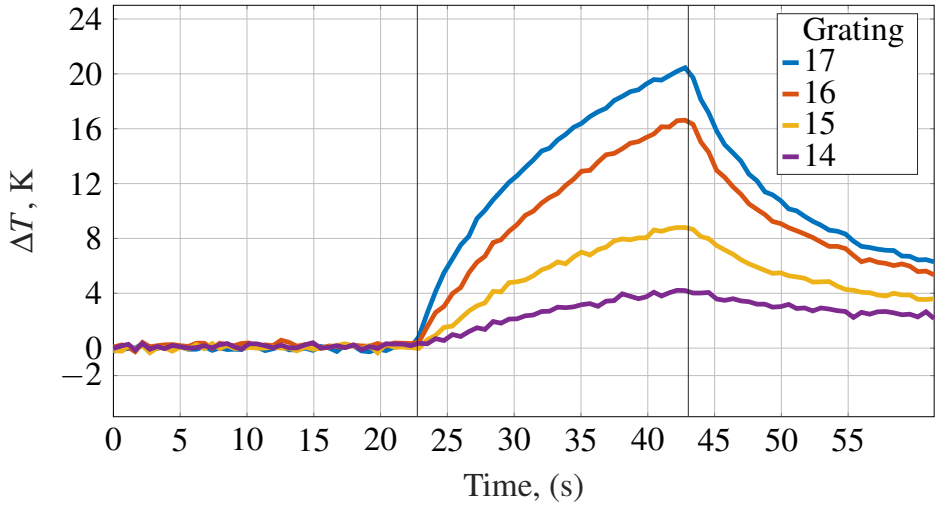

Figure 9.4: Temperature trends acquired by FBG during experimental text.

The temperature trends obtained from the experimental tests are fitted to the analytical solution of the bioheat equation. In particular, the following steps are listed:

1. Reconstruction of the phantom thermal property value knowing the certain relative distance of 1 mm between each FBG in the array. Fitting with the temperature trend of the gratings is carried out simultaneously to find the optimal sensors positions. The program input is an estimate of the position of the first grating; the outputs are the thermal diffusivity value of the analyzed tissue and the true position of the gratings.

The Tab. 9.1 shows the positions of the FBG recovered by the method with respect to the heat source. The reconstructed thermal diffusivity is

Table 9.1: FBGs position reconstruction during the experimental activity.

Sensing point locations	
Grating	Distance, (mm)
17	2.5
16	2.7
15	3.2
14	3.9

: 3.95×10^{-7} m^2/s. The reconstructed σ_s of the source is about 1.5 mm.

2. The locations of the sensors relative to the center of the source are known from the first step. At this point, a second program in Matlab is used to analyze each temperature trend separately, and diffusivity is obtained for each sensor. The Tab. 9.2 show the reconstructed thermal diffusivity value for each sampling point and the relative percent error from the reference water value of : $1.341{,}8 \times 10^{-7}$ m^2/s. The recon-

Table 9.2: Diffusivity estimation error in the experimental activity.

Thermal diffusivity and sensing positions		
Grating	Thermal diffusivity, (m^2/s)	Relative error, (%)
17	7.51e-7	82,3%
16	3.54e-7	62%
15	3.9e-7	66%
14	4.7e-7	72%

structed thermal parameter values for each sensor are in agreement with the value found in the first stage. In addition, the reference diffusivity value is not known, as phantom has properties only similar to those of water.Therefore, results are considered optimal when parameter estimation errors are similar for all sensor points, as in this case.

3. Once the thermal behavior of the tissue is obtained, the ability of the model to predict the temperature response of the target volume is analyzed. The temperatures predicted by the method and those obtained experimentally are compared. The model developed in this thesis shows an absolute maximum error in reconstructing the thermal response of the tissue under investigation of about 1 °C. The Tab. 9.3 show the temperature estimation error in details.

Table 9.3: Temperature estimation error in experimental activity. Difference between actual acquired temperature and estimated temperature.

Temperature predicted error	
Grating	ΔT
17	0.8627
16	-1.3274
15	-0.8254
14	-0.5913

Fig. 9.5 shows the comparison between the temperature estimated by the model (solid line) and the actual temperature acquired by the sensors (dots).

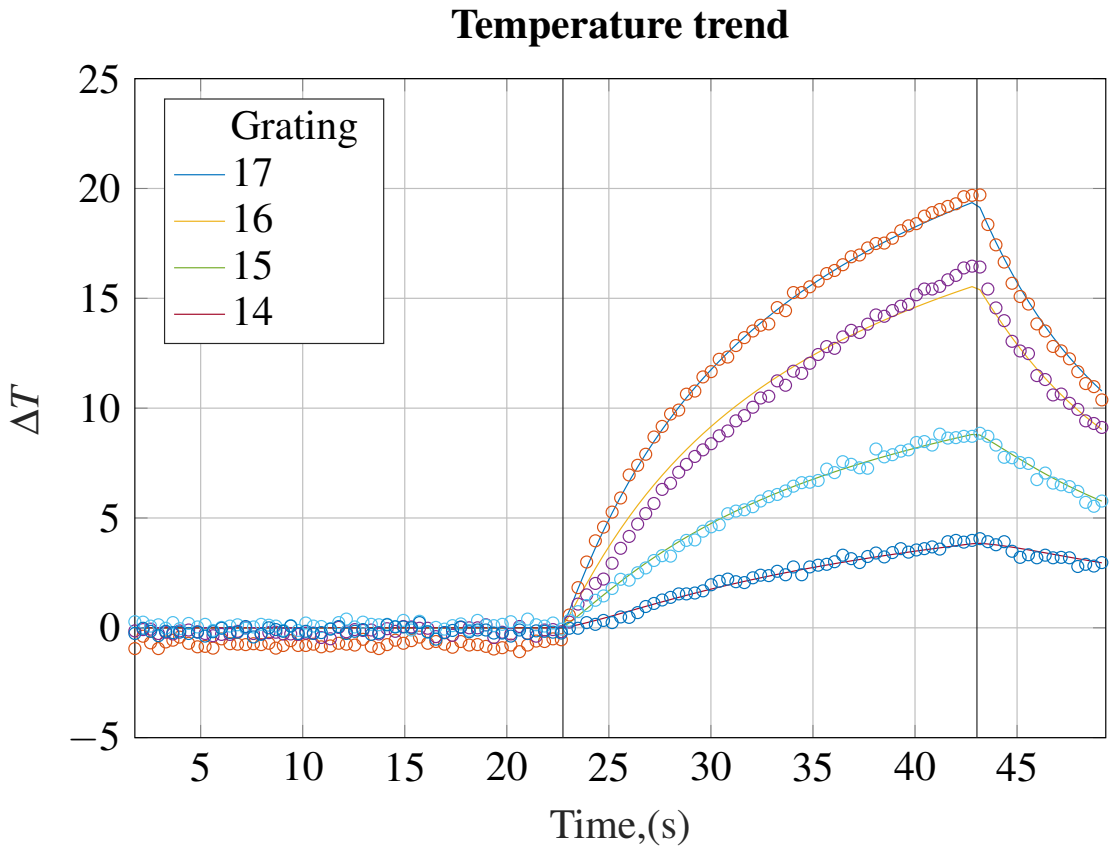

Figure 9.5: Temperature trends acquired by FBG and temperature predicted by the thermal model.

Chapter 10

Experimental tests with micro-pulsed laser technology

This chapter is devoted to thermal therapies based on micro-pulsed laser technology. In particular, new ophthalmological treatments based on the yellow laser are presented, together with an experimental activity aimed at developing a sensorized retinal simulator.

10.1 Modern laser therapy

Micropulsed retinal laser treatment is a modern thermal therapy designed to minimise collateral damage to the biological tissues involved in retinal target zone. The main diseases treated with this therapy are diabetic macular edema and macular edema secondary to retinal vein occlusion. Several studies [36, 37] have investigated the qualities of micropulsed lasers for photocoagulation in the treatment of diabetic macular edema. In particular, the new technology results in superior clinical performance compared with conventional modified ETDRS laser procedures, with less damage associated with the retinal pigment layer. Diabetic macular edema consists of fluid

accumulation in the macula due to molecular mechanisms such as increased oxidative stress resulting in increased cell permeability. The new therapy aims to restore the balance between oxidants and antioxidants within the retinal layers and stimulate cytokine production, with anti-angiogenic and anti-edema effects. The therapeutic procedure involves the placement of a high density of confluent laser spots over the entire target area, selectively targeting the RPE and choroidal melanin. The laser emits groups of microsecond pulses, with a typical exposure duration of 100 us and a recovery time between pulses of 1.9 ms. Laser off periods of several milliseconds allow the tissue to return to baseline temperature before the next laser pulse. The pulse envelope duration of the pulse burst is about 200 or 300 ms, with an emission frequency of 500 Hz. It is important to emphasize that the treatment has been defined as "subthreshold" or "subvisible" because the laser application does not cause intraretinal damage or visible scarring, even after the therapy; therefore, the end result is tissue with no observable laser effects. The Fig. 10.1 show the mechanism of action of the micropulsed laser technology. The lasers in conventional ophthalmoglogic therapies

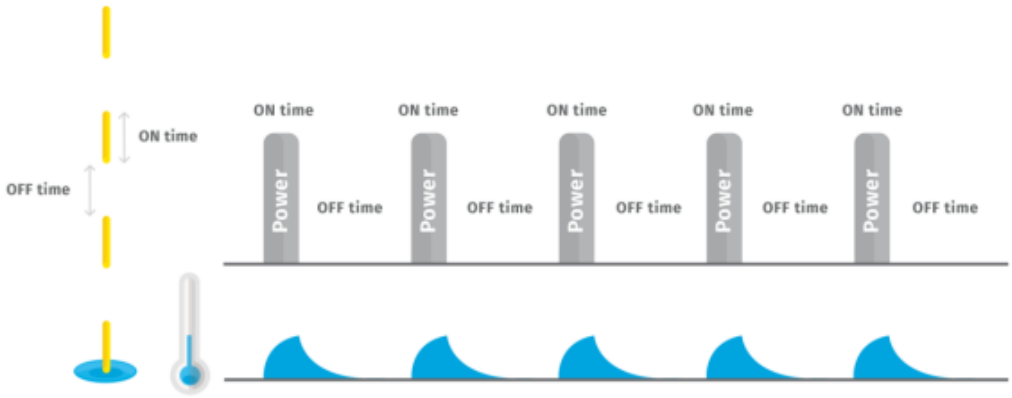

Figure 10.1: Micropulsed laser therapy [38].

work in CW mode, emitting a constant flow of energy, and this results in a significant thermal increase in the target area. The ability to pulse laser energy with a given Duty Cycle over the duration of emission allows the tissue to cool between pulses, reducing thermal buildup. The Fig. 10.2 show the two type of laser emission mode.

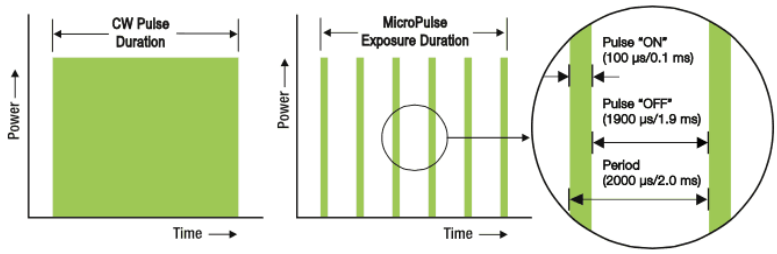

Figure 10.2: Continuous wave and micro-pulsed laser Therapy [39].

In conclusion, micropulsed technology therapy stimulates a natural healing response of the eye with a mechanism of photostimulation of reparative biological processes and cell regeneration, and the new cells help restore proper retinal function.

10.1.1 Experimental laser activity

The experimental activity describes a study aimed at developing a sensorized retina simulator to support the ophthalmologists in evaluating possible thermal effects of laser processes.In particular, the attention is on the case of yellow lasers used to treat macular retinopathies. The goal is to evaluate the thermal behavior of retinal cells during micropulsed laser therapies with invisible endpoints.The developed device incorporates an NTC sensor positioned toward the surface to assess the temperature change around the exposed area. Preliminary tests were conducted with a commercial technology, the IQ 577® system based on a solid-state laser emitting from continuous wave regime to micropulsed regime. The energy (J) delivered during treatments is equal to the product of the laser power (W) with the exposure duration and utilization factor (% /100). The utilization factor is often 5% to 15% when using the MicroPulse mode and is 100% in the continuous wave mode.

Phantom

The retina involved in micro-pulsed laser treatments has a thickness of a few hundred micrometres. Therefore, the simulator was constructed considering a thin layer of material, in the shape of a rectangular prism, with height of 1 cm and area of 22.75 cm^2 . The material used for the preliminary tests is a silicone rubber, which allows the shape of the simulator's physical structure to be generated repeatably and quickly. Thermochromic pigments are incorporated into the simulator material, which change color following a heat-induced variation in the chemical composition. Indeed, the heat applied to the thermochromic microcapsules induce changes to the the structure of the substance inside the microcapsule and consequently the colour disappears. The structural change is reversible so that during cooling, the microcapsule returns to its original color. The first pigment used is sensitive to threshold 75 °C, the temperature at which it changes color from black to white. This pigment is added throughout the base of the phantom. The second pigment changes colour from red to white sensitive to the 45 °C temperature threshold and is added only on the surface of the simulator, at the treatment area. The presence of the colored pigment increases the

absorption of laser energy by the phantom during experimental tests. In addition, the change in colour provides direct and rapid visible feedback on the temperature range reached by the developed device, especially during validation tests in the laboratory. The Figs 10.3 show the devices developed; in particular, the figure on the right shows the surface color change of the simulator being illuminated by the collimated laser, generating temperatures greater than or equal to 45 °C .

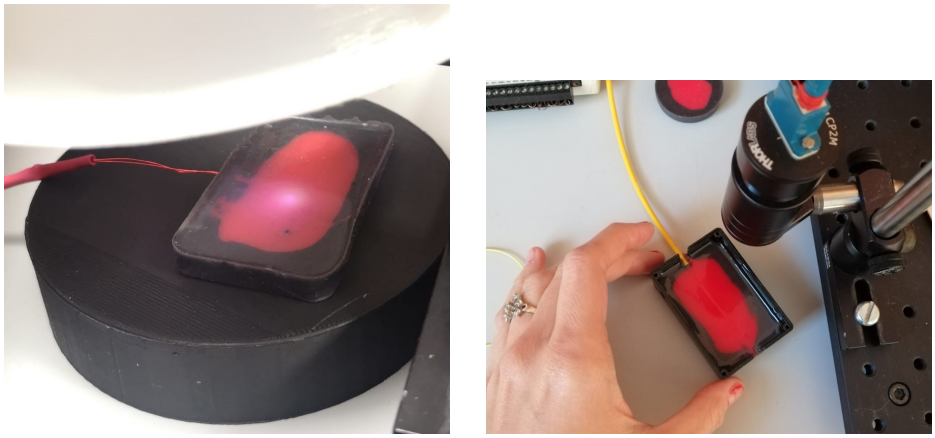

Figure 10.3: Sensorized retina simulator with thermistor sensor (left) and with FBG (right).

Experimental set-up and instrumentation

The temperature acquisition is obtained by a commercial thermistor NTC, with a resistance R_0 equal to 10 kΩ, and it is placed in the centre surface of the simulator. The relationship between the temperature sampled by the sensor and the change in resistance is given by the β-parameter equation:

$$T = \frac{T_0 \beta}{T_0 \ln(R/R_0) + \beta} \tag{10.1}$$

where R_0 = 10 kΩ and $T_0 = 25$ °C.
The National Instrument USB-6211 DAQ acquisition system is used to acquire a voltage in volts proportional to the change in thermistor resistance, via a voltage divider. A program on Labview software is developed to

acquire the voltage signal, to obtain the temperature trend and to visualize the thermal response in real time. The experimental tests were performed with the typical laser parameter set-up used during retinal treatments. In the first test, the square grid pattern of 7x7, the pulse train envelope of 200 ms and the spot diameter of the laser beam of 200 nm were set constant. The laser power was initially set at 250 mW and subsequently increased to 300 mW and then 400 mW. This test involved a duty cycle of 5%. The second experimental test involves setting the same initial laser setting parameters used during the first test, but the duty cycle is increased from 5% to 15%. The simulator's response was then evaluated for the following laser powers: 100 mW - 250 mW - 300 mW - 400 mW - 500 mW - 1,000 mW - 1,400 mW. Finally, a final test was performed keeping the duty cycle constant at 15%, as in the previous case, but increasing the envelope of the pulse train to 300 ms and increasing the spot diameter of the laser beam to 300 nm. The power was set to 1,000 mW. The initial temperature of all three tests is approximately 27 °C. The Fig. 10.4 show the experimental set-up and instrumentation; in particular, in the figure the laser is active, emitting a collimated beam on the sensing surface of the device.

Figure 10.4: Device developed and IQ 577™ Laser System with slit lamp (Cavallini Prof. Gian Maria Studio Oculistico a Modena).

10.2 Results and observations

The Figs 10.5 show the temperature response using a spot size of 200 µm and a pulse envelope duration of 200 ms. The Duty cycle imposed is 5%. The results show a significant increase in temperature with powers of 400 mW.

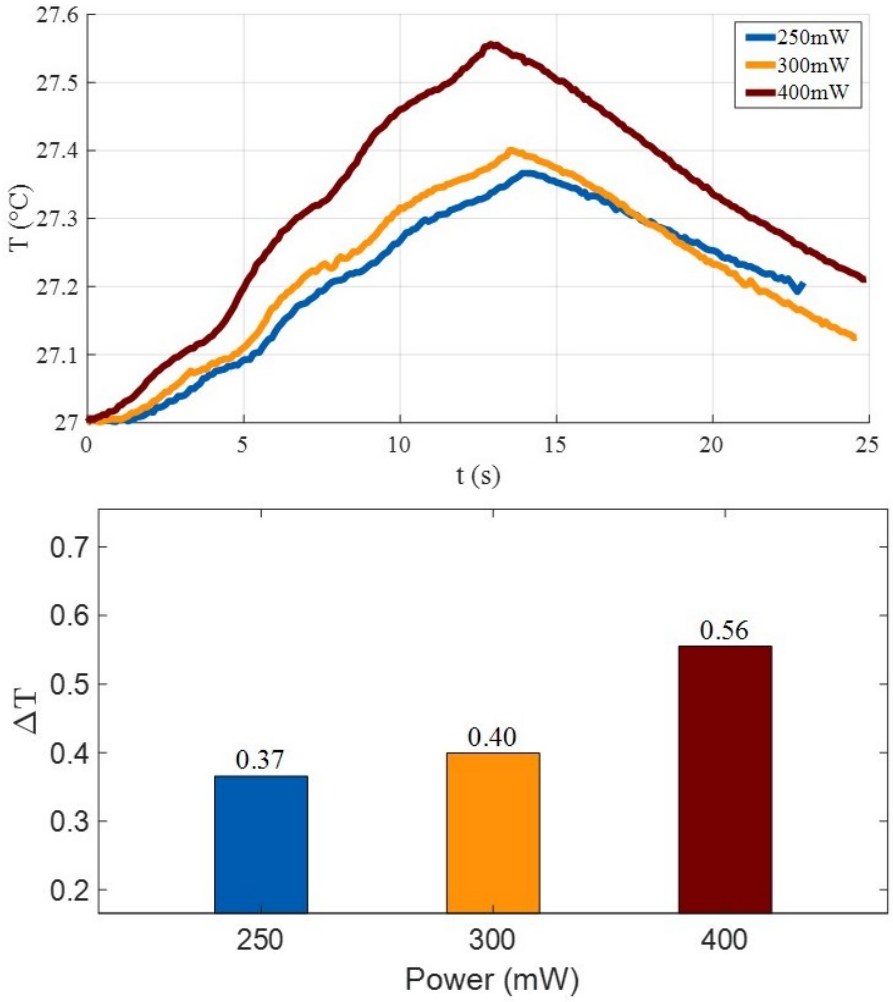

Figure 10.5: Temperature trend and maximum temperature variation versus laser power with D.C. of 5%.

The Figs 10.6 show the temperature response using a spot size of 200 µm and a pulse envelope duration of 200 ms. The Duty cycle imposed is 15%.

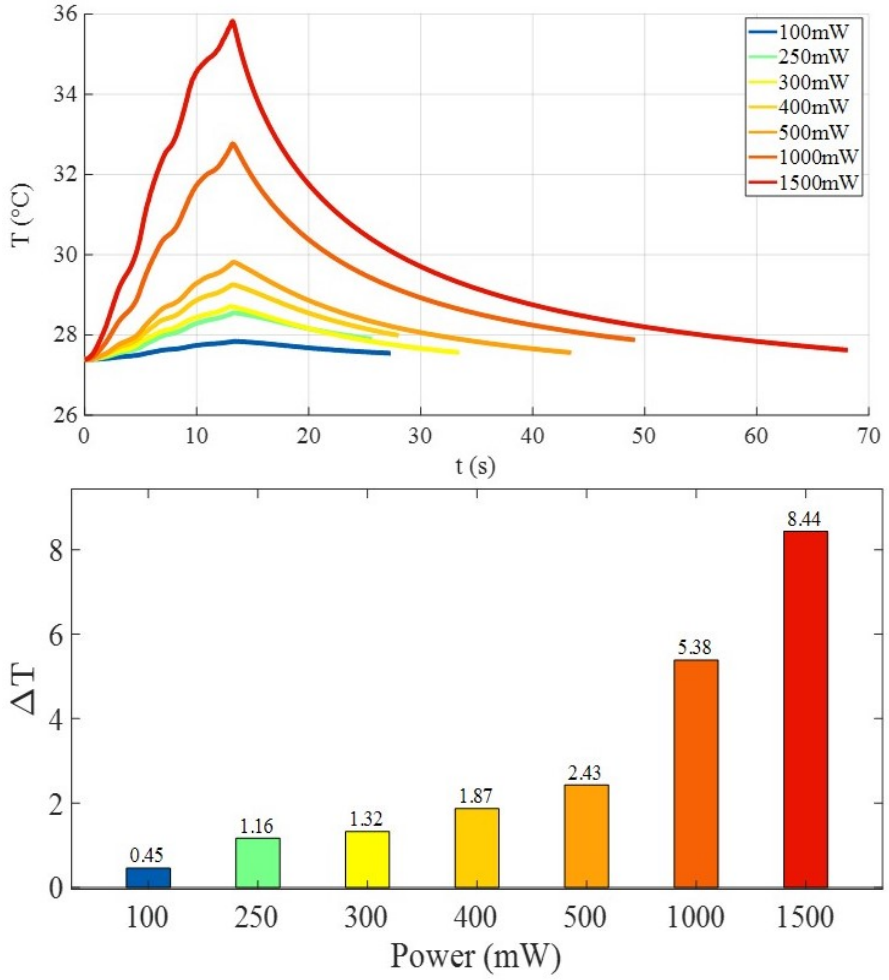

Figure 10.6: Temperature trend and maximum temperature variation versus laser power with D.C. of 15%.

The Figs 10.7 show the temperature response using a spot size of 300 µm and a pulse envelope duration of 300 ms. The Duty cycle imposed is 15%. From the processing of the data, it is concluded that if the power and all other parameters are equal, varying the duty cycle from 5% to 15%, results in a temperature increase of about 1.1 °C. Moreover, if the power and duty cycle are equal, varying the spot diameter (µm) and the pulse duration (ms) from 200 to 300 results in a temperature increase of about 1 °C. The results obtained demonstrate the effectiveness of these early experimental tests, which provide a basis for the future development of a sensorized device with

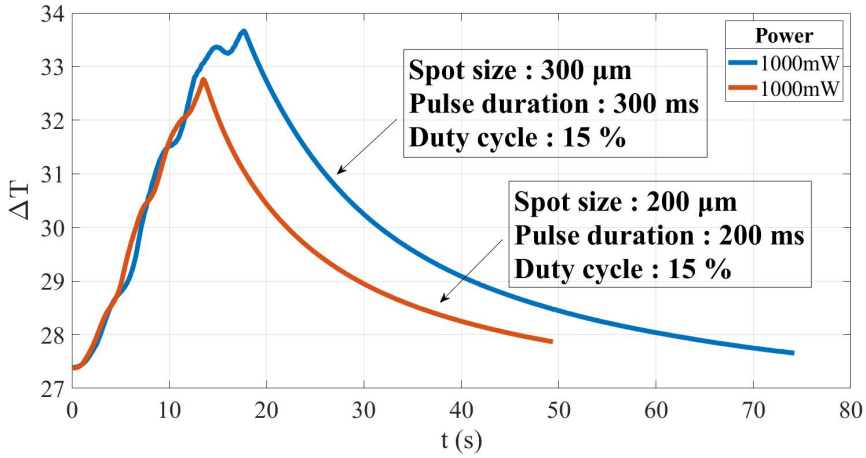

Figure 10.7: Temperature trends with different spot size and pulse duration.

retinal tissue-like properties to evaluate the thermal load of cells exposed to laser treatments.

Part IV

Conclusion

Chapter 11

Conclusions and outlook for the future

In the coming years, ophthalmologists will face an increase in age-related eye diseases that could lead to blindness. Currently, there are no definitive therapies that can reverse the eye conditions, and treatments aim to stop or at least slow their progression. One of the most promising methods is the use of lasers for thermal therapies, especially since the development of micro-pulse technology, which has led to the introduction of a number of innovative treatments. Despite the advantages and potential of this new approach, its development in the therapeutic field is limited by the lack of guidelines for treatment planning and monitoring.
This master's thesis aims to develop a method to optimize thermal procedures by providing a tool for accurately predict and measure laser-induced temperature in biological tissues. The first part of the project involved the implementation of a parametric 3D model of the human eye to provide key information on laser-tissue interaction. In particular, finite element methodology analyzed the intrinsic physics involved in thermal therapies: the tissue absorption of laser radiation and the heat transfer in the biological tissues. The model provided important insights into the maximum temperature reached in irradiated ocular tissues during the simulation period. Results show temperature peaks above 90 °C in the retinal pigment

epithelium through the application of lasers in continuous wave emission, emphasizing the importance of micro-pulsed technology in reducing cellular damage. In view to provide a tool for planning personalized treatments for each patient, the second part of the project focuses on the study of a method for assessing the thermal properties of biological tissues. The heat pulse method developed in the thesis is based on the bio-heat transfer equation solved through the Green's function method. The model is based on the thermal response of the tissue to a short pulse of heat, not intense enough to cause cell damage, which is fitted to the analytical solution of the bio-heat equation. Numerical simulations in COMSOL validated the proposed method. The analysis of the impact of experimental uncertainties on the model results allowed the evaluation of the method's applicability limits. The conclusions from the analysis are:

- The effect of additive noise on the temperature acquired signal is significant for distances from the source greater than 3.2 mm. However, the impact of this uncertainty appears to be limited; considering a very low SNR of about 4 dB, the absolute temperature over-estimation error is about 0.3 °C;
- In the presence of synchronization uncertainty, positive time delays and distances from the source greater than 3.4 mm are favored. In this way, the uncertainty results in an over-prediction of the thermal response of the system, which is preferable to under-estimating the temperature, considering the photo-thermal applications of the laser. Moreover, for the specified positions, the temperature reconstruction errors are lower than ΔT=0.5 °C , for all synchronization uncertainties;
- The uncertainty of sensor position has a significant effect on the estimation of thermal properties and temperature. In particular, for errors greater than or equal to 0.1 mm, the temperature estimation error exceeds the value of ΔT=0.5 °C for locations closer to the heat source, from 2.5 mm to 3.3 mm. Through the use of fiber-optic Bragg grating arrays, the impact of position error on model results is significantly reduced;

- Optimization of the method involves associating the temperature acquired by the 1-mm-long sensor FBG with the position of its midpoint. The absolute error of temperature estimation due to non-point sensors effect is less than ΔT= - 0.2 °C from a distance of 2.5 mm.

The third part of the project involved the experimental activity, in which the temperature distribution is acquired with all-optical fiber sensors, and is displayed in real-time through a program developed in Matlab. The thermal diffusivity of phantom is considered similar to that of water as a reference: $1.341{,}8 \times 10^{-7}$ m^2/s. The results, obtained by analyzing the temperatures measured from the FBGs closest to the source, show a reconstructed thermal diffusivity with a mean of 5×10^{-7} metersquare/ and a standard deviation of 1.7×10^{-7} metersquare/. Despite the non-negligible error on the recovery of diffusivity, the thermal response estimated by the model has a maximum temperature overestimation error of about ΔT= 1 °C. These results are good, considering the small number of pratical tests and the limitations due to experimental uncertainties.
Future prospects for method development involve the analysis of new thermal models based on different spatial distributions of the heat source, for example, considering the sum of multiple Gaussian-type sources. Another important future prospect involves the development of a new applicator for the thermal parameter reconstruction method; the probe is expected to incorporate a fiber with FBGs as temperature sensors, in parallel with the laser beam-emitting fiber. The goal is to reduce the invasive impact in the tissue and improve the reconstruction of thermal properties Other future developments include application of the method to temperature distributions obtained with millisecond-order heat pulses through the use of pulsed laser technologies. In the end, a key starting point for future research is the investigation of the optical interaction between the laser and the biological tissue, based mainly on the absorption of light and the subsequent generation of the heat source in the tissue.

In conclusion, the aims of this thesis have been achieved through new approaches that allowed the evaluation of some fundamental aspects of thermal therapies in ophthalmology, and which can be used as starting points for future research aimed at improving the therapeutic application of laser in ophthalmology.

Bibliography

[1] *Blindness and vision impairment*. https://www.who.int/news-room/fact-sheets/detail/blindness-and-visual-impairment (cit. on p. 1).

[2] *Projected Change in Vision Loss 2020 to 2050*. https://www.iapb.org/learn/vision-atlas/magnitude-and-projections/projected-change/ (cit. on p. 2).

[3] Theodore H Maiman et al. «Stimulated optical radiation in ruby». In: (1960) (cit. on p. 5).

[4] Ryan Lee, Tien Y Wong, and Charumathi Sabanayagam. «Epidemiology of diabetic retinopathy, diabetic macular edema and related vision loss». In: *Eye and vision* 2.1 (2015), pp. 1–25. DOI: 10.1186/s40662-015-0026-2 (cit. on p. 8).

[5] DRS Study Group et al. *Photocoagulation treatment of proliferative diabetic retinopathy. Clinical application of Diabetic Retinopathy Study (DRS) findings*. Tech. rep. DRS report. DOI: 10.1016/S0161-6420(81)34978-1 (cit. on p. 9).

[6] Early Treatment Diabetic Retinopathy Study Research Group et al. «Treatment techniques and clinical guidelines for photocoagulation of diabetic macular edema: Early Treatment Diabetic Retinopathy Study Report Number 2». In: *Ophthalmology* 94.7 (1987), pp. 761–774. DOI: 10.1016/s0161-6420(87)33527-4 (cit. on pp. 9, 11).

[7] Lesley A Everett and Yannis M Paulus. «Laser therapy in the treatment of diabetic retinopathy and diabetic macular edema». In: *Current*

Diabetes Reports 21 (2021), pp. 1–12. DOI: 10.1007/s11892-021-01403-6 (cit. on pp. 9, 11).

[8] Jennifer K Sun et al. «Rationale and application of the protocol S anti–vascular endothelial growth factor algorithm for proliferative diabetic retinopathy». In: *Ophthalmology* 126.1 (2019), pp. 87–95. DOI: 10.1016/j.ophtha.2018.08.001 (cit. on p. 9).

[9] Alexandre Uwimana, Cong Ma, Shengyao Chen, and Xiang Ma. «Metformin therapy as a strategy to compensate anti-VEGF resistance in patients with diabetic macular edema». In: *Medicine* 101.42 (2022), e31266. DOI: 10.1097/MD.0000000000031266 (cit. on p. 9).

[10] Linh TD Truong, Peter J Lesniewski, and A Bruce Wedding. «Heat transfer simulation in laser irradiated retinal tissues». In: *Biomedical Physics & Engineering Express* 8.1 (2021), p. 015027. DOI: 10.1088/2057-1976/ac3f51 (cit. on pp. 10, 37, 39, 40, 42).

[11] Anita Prasad. *Laser Techniques in Ophthalmology: A Guide to YAG and Photothermal Laser Treatments in Clinic*. CRC Press, 2022. DOI: 10.1201/9781003144304 (cit. on pp. 10–12, 14).

[12] Kobi Aflalo, Moshe Ben-David, Adrian Stern, and Irit Juwiler. «Theoretical investigation of using a yellow (577nm) laser for diabetic retinopathy». In: *OSA Continuum* 3.11 (2020), pp. 3253–3266. DOI: 10.1364/OSAC.399120 (cit. on pp. 10, 39, 40).

[13] Martin A Mainster. «Wavelength selection in macular photocoagulation: tissue optics, thermal effects, and laser systems». In: *Ophthalmology* 93.7 (1986), pp. 952–958. DOI: 10.1016/S0161-6420(86)33637-6 (cit. on p. 10).

[14] Sibel Inan, Onur Polat, Safiye Yıgıt, and Umit Ubeyt Inan. «PASCAL laser platform produces less pain responses compared to conventional laser system during the panretinal photocoagulation: a randomized clinical trial». In: *African Health Sciences* 18.4 (2018), pp. 1010–1017. DOI: 10.4314/ahs.v18i4.22 (cit. on p. 10).

[15] PH Zhao et al. «A coupled BioHeat transfer model for customized whole-eye modeling in retinal laser surgery». In: *International Journal of Thermal Sciences* 183 (2023), p. 107897 (cit. on pp. 11, 48).

[16] Wenjia Wang, Xiuqing Qian, Hongfang Song, Mindi Zhang, and Zhicheng Liu. «Fluid and structure coupling analysis of the interaction between aqueous humor and iris». In: *Biomedical Engineering Online* 15 (2016), pp. 569–586 (cit. on p. 13).

[17] Felipe Eduardo Dhawahir-Scala and David Clark. «Neodymium: YAG laser peripheral iridotomy: cause of a visually incapacitating cataract?» In: *Ophthalmic Surgery, Lasers and Imaging Retina* 37.4 (2006), pp. 330–332. DOI: 10.3928/15428877-20060701-14 (cit. on p. 14).

[18] *Laser peripheral iridotomy*. https://www.glaucomapatients.org/treatment/laser-peripheral-iridotomy/ (cit. on p. 15).

[19] Anna M Roszkowska, Mario Urso, Alberto Signorino, and Pasquale Aragona. «Use of the femtosecond lasers in ophthalmology». In: *EPJ Web of Conferences*. Vol. 167. EDP Sciences. 2018, p. 05004. DOI: 10.1051/epjconf/201816705004 (cit. on p. 18).

[20] Kendall E Donaldson et al. «Femtosecond laser–assisted cataract surgery». In: *Journal of Cataract & Refractive Surgery* 39.11 (2013), pp. 1753–1763 (cit. on p. 19).

[21] *Laser Beam Welding setup*. https://blogmech.com/how-laser-beam-welding-works-laser-beam-welding-process/ (cit. on p. 22).

[22] *Laser Diode: Definition, Working Principle, Application Types*. https://collegedunia.com/exams/laser-diode-definition-working-principle-application-and-types-physics-articleid-3055 (cit. on p. 23).

[23] *Optical Fiber Cables - Construction and Application*. https://foconec.com/optical-fiber-cables-construction-and-application/ (cit. on p. 24).

[24] *Optic fibre-numerical aperture diagram*. https://zh.wikipedia.org/wiki/File:Optic_fibre-numerical_aperture_diagram.svg (cit. on p. 25).

[25] Erden Ertorer, Moez Haque, Jianzhao Li, and Peter R Herman. «Femtosecond laser filaments for rapid and flexible writing of fiber Bragg grating». In: *Optics Express* 26.7 (2018), pp. 9323–9331. DOI: 10.1364/OE.26.009323 (cit. on p. 27).

[26] Dongdong Chen, Linsheng Huo, Hongnan Li, and Gangbing Song. «A fiber bragg grating (FBG)-enabled smart washer for bolt pre-load measurement: design, analysis, calibration, and experimental validation». In: *Sensors* 18.8 (2018), p. 2586. DOI: 10.3390/s18082586 (cit. on p. 30).

[27] Inessa Bekerman, Paul Gottlieb, and Michael Vaiman. «Variations in eyeball diameters of the healthy adults». In: *Journal of ophthalmology* 2014 (2014). DOI: 10.1155/2014/503645 (cit. on p. 37).

[28] Rita Ehrlich, Alon Harris, Scott M Wentz, Nicholas A Moore, and Brent A Siesky. «Anatomy and regulation of the optic nerve blood flow». In: (2017) (cit. on p. 37).

[29] Ashley J Welch, EH Wissler, and Leslie A Priebe. «Significance of blood flow in calculations of temperature in laser irradiated tissue». In: *IEEE Transactions on Biomedical Engineering* 3 (1980), pp. 164–166. DOI: 10.1109/TBME.1980.326619 (cit. on p. 42).

[30] J Sandeau, J Kandulla, H Elsner, R Brinkmann, G Apiou-Sbirlea, and R Birngruber. «Numerical modelling of conductive and convective heat transfers in retinal laser applications». In: *Journal of Biophotonics* 1.1 (2008), pp. 43–52. DOI: 10.1002/jbio.200710012 (cit. on p. 42).

[31] Markolf H Niemz et al. *Laser-tissue interactions*. Vol. 322. Springer, 2007 (cit. on pp. 47, 48).

[32] *Thermal Conductivity*. https://itis.swiss/virtual-population/tissue-properties/database/thermal-conductivity/ (cit. on p. 56).

[33] Hailong He, Miles F Dyck, Robert Horton, Tusheng Ren, Keith L Bristow, Jialong Lv, and Bingcheng Si. «Development and application of the heat pulse method for soil physical measurements». In: *Reviews of Geophysics* 56.4 (2018), pp. 567–620. DOI: 10.1029/2017RG000584 (cit. on p. 58).

[34] Riccardo Gassino. «Development of a fiber optic probe for tumor laser ablation with integrated temperature». In: (2020) (cit. on p. 86).

[35] WK Lee, YY Lim, and A Leow. «TC., Namasivayam, P., Ong Abdullah, J., and Ho, CL.(2017). Biosynthesis of agar in red seaweeds: a review». In: *Carbohydr. Polym* 164 (), pp. 23–30. DOI: 10.1016/j.carbpol.2017.01.078 (cit. on p. 100).

[36] D Lavinsky and JA Cardillo. «Melo LAS, Dare A, Farah ME, Belfort R. Randomized Clinical Trial Evaluating mETDRS versus Normal or High-Density Micropulse Photocoagulation for Diabetic Macular Edema». In: *Investigative Ophthalmology & Visual Science* 52.7 (2011), p. 4314. DOI: 10.1167/iovs.10-6828 (cit. on p. 107).

[37] Joao Figueira, Jaheed Khan, Sandrina Nunes, Sobha Sivaprasad, Andreia Rosa, Jose Faria de Abreu, Jose G Cunha-Vaz, and NV Chong. «Prospective randomised controlled trial comparing sub-threshold micropulse diode laser photocoagulation and conventional green laser for clinically significant diabetic macular oedema». In: *British Journal of Ophthalmology* 93.10 (2009), pp. 1341–1344. DOI: 10.1136/bjo.2008.146712 (cit. on p. 107).

[38] *Trattamenti laser*. https://miloftalmica.it/wp-content/uploads/2021/07/Informativa-Trattamenti-Laser.pdf (cit. on p. 108).

[39] *Come si cura la Maculopatia: Interventi e Laser*. https://www.microchirurgiaoculare.com/maculopatia/laser-interventi/ (cit. on p. 109).